POLITECNICO DI TORINO

Master's Degree in Mechanical Engineering

Master Thesis

Materials for Lightweight Bio-Inspired Structures with High Stiffness

Thesis Advisor:
Prof. Ing. Eugenio Brusa

Candidate:
Alberto Franco

Abstract

This thesis presents a detailed investigation into the structural and mechanical performance of a bio-inspired structure inspired from the internal cellular structure of the fungus Fomes fomentarius, and more specifically from high-porosity Hymenium layer. Using the Autodesk AutoCAD 2026 software, 3D models of the bio inspired structure were designed, and Finite Element Analysis (FEA) with the LS-DYNA software was executed in order to simulate the obtained cubic specimens under quasi-static uniaxial compression and tension, both in vertical (Out of plane) and horizontal (In plane) directions. The specimens were supposed to be produced of three common Additive Manufacturing materials: Titanium alloy Ti6Al4V, Aluminium alloy 6061-T6, and Acrylonitrile Butadiene Styrene (ABS). The studied simulations included two comparative strategies. In the first one, all specimens had the same external dimensions, differing only in the material, while in the second one, they were adjusted to have an identical mass, (taking the ABS specimen mass as reference), allowing to evaluate specific parameters of the structure. The obtained results confirmed the orthotropic mechanical response of the bio-inspired structure, which registered significantly higher stiffness and strength along the primary axis of the cylindrical holes (Vertical/Out-of-Plane direction) and lower values on the perpendicular (Horizontal/In-Plane direction). Moreover, the results also showed a high asymmetry of strength in tension and compression ($\sigma_{\text{max,Comp}} > \sigma_{\text{max,Tens}}$), especially for metal specimens, where compression benefits from energy absorption mechanisms like buckling, allowed to withstand higher ultimate load than that imposed by tensile rupture. Ultimately, Titanium Ti6Al4V showed the best overall specific performance, and the ABS polymer confirmed its use for high-strain energy absorption application.

Contents

1 Bio-Inspired Structure

1.1 Introduction to Bio-Inspired Structures

Bio-inspired structures are engineering systems that are modelled after biological systems and organisms. This kind of design is a growing design approach in multiple fields of engineering thanks to the peculiar characteristics and architectures of natural structures and topologies. It is a result of millions of years of evolution, that can produce structures that can be lightweight and offer combinnations of mechanical properties that often surpass those of their components considered alone.
More specifically, bio-inspired structures, often present advantages such as:

- High strength-to-weight ratio
- High energy absorption capacity
- Enhanced heat transfer
- Excellent toughness and stiffness
- Able to handle dynamic loads

Bio-inspired structure may have a complex configuration, in fact, natural systems are usually complex and anisotropic. Considering different scales, going from nano to macro scale, very common patterns that can be encountered in natural systems are, for instance, lamellar arrangement, columnar alignment, coaxial layered arrangement, tubular array structure, which all give different mechanical characteristics to the system.
In some cases, the same structure can exhibit distinct layers with different motifs, such as the combination of columnar and lamellar regions in a shell, which allow to combine and often improve the mechanical characteristics.

This type of structure cannot be built accurately using traditional manufacturing technologies and conventional approaches.
In recent years, with the advantages, with the advancements of additive manufacturing and computational modelling, complex structures inspired from natural systems can be fabricated with more ease and with an high level of precision and reproducibility, allowing the mimicking of biological creatures to become more popular, opening a promising path for new application in multiple engineering fields, such as aerospace, transportation, civil engineering, biomedical, where lightweight structures are usually preferred.

Learning from nature allows the discovery of new ways to overcome technological limitations in both industrial and everyday contexts. Natural biological structures are a constant source of inspiration for the development of new materials and structures with multifunctional properties. Emulating the design logic of natural organisms, which have evolved to be highly efficient and multifunctional in order to survive in harsh environments, engineers can develop synthetic materials that embody the same principles. Biomaterials and biological systems are lightweight but impact-resistant and can withstand external dynamic loading as a result of their complicated architectures and hierarchical structure.

A comprehensive understanding of the structure-function relationship in nature allows the development of artificial materials with enhanced impact resistance and energy absorption. It is then essential to have the knowledge of the dynamic response of bio-inspired structures to establish the design principles, mechanisms, and modelling strategies that govern their performance. These elements make bio-inspired structures strong candidates for impact protection in engineering systems. Moreover, the discovery and understanding of nature-designed systems can promote the utilization of data-driven methodologies in structure design and support the development of more efficient and less expensive manufacturing technologies.

1.2 Structural Features and Natural Inspirations

Over billions of years, nature has optimized materials and structures to be multifunctional, efficient, and mechanically optimized. Hierarchical structure at several length scales ranging from nano- to the macro-scale are characteristic aspects of natural architecture. Natural material structures enable them to achieve more excellent combinations of lightness, strength, and toughness, often many times better than their man-made counterparts with similar density.

Typical structural elements of biological origin are tubular, fibrous, cellular, hierarchical, and helical structures. Tubular structures occur in beetle elytra, horse hooves, and ram horns; fibrous structures occur in spider silk, silkworm cocoons, and wood; cellular structures occur in bones and muscles; while hierarchical and helical motifs occur in the fractal branching of trees, in the glass sponge skeleton, and in the dactyl club of mantis shrimps. All of these natural systems provide a unique mechanical benefit, ranging from impact resistance and energy absorption to flexibility and stiffness optimization.

One of the universal laws that dictate such systems is material efficiency in which nature employs minimal material and obtains a maximum amount of structural performance. This is achieved by integrating multiple design aspects contained within a single structure so that the resultant architectures are simultaneously complex and yet highly organized. This leads to having the overall performance of these natural systems, which is greater than the sum of the mechanical characteristics of their individual components.

The starting point of bio-inspired design is therefore the understanding of these natural processes and translating their principles into engineering design. The reliability of this exercise relies on the availability of advanced characterization techniques, such as Scanning Electron Microscopy (SEM), Transmission Electron Microscopy (TEM), Atomic Force Microscopy (AFM), and Micro-Computed Tomography (µCT), through which natural architectures can be thoroughly analyzed at different scales.

With these tools is it now possible to study the micro- and nano-scale morphology of biological materials, and hence discover their anisotropy, hierarchical organization, and functional gradients. It is the knowledge on which to base the development of synthetic systems with the efficiency and multifunctionality of the biological original.

1.3 Manufacturing Technologies for Bio-Inspired Structures

The reproduction of biological architectures in engineering requires advanced manufacturing technologies that replicate the complicated geometries and multi-scale structuring of natural systems. Conventional manufacturing technologies are often not suitable to replicate the complexity required in bio-inspired designs. Many natural structures are characterized by porous, reticulated, or hierarchically patterned morphologies, which cannot be properly produced using conventional methods.

The recent development of additive manufacturing (AM) has revolutionized this field, allowing to create extremely complex geometries with high precision and control. Additive manufacturing builds parts layer by layer starting from a computer-aided design (CAD) model. This allows to create structures that would be otherwise impossible or extremely challenging to produce with traditional manufacturing methods.
AM also provides significant flexibility over conventional processes for developing bio-inspired structures.

Many AM techniques have been used to produce bio-inspired structures. Some of the most common are: Selective Laser Melting (SLM), Selective Laser Sintering (SLS), Laser Engineered Net Shaping (LENS), and stereolithography; and each process has its own advantages and limitations.
A wide range of materials such as polymers, metals, ceramics and composites, can be used in Additive Manufacturing, extending the possibility of the creation of bio-inspired structures.

However, AM may present some limitations that influence its suitability to bio-inspired components, such as process speed, surface finish, material and operating costs, and defect generation like porosity, unmelted particles and balling. Moreover, residual stress and the subsequent need for post-heat treatment are additional issues for metal AM, and parts with complex internal features, usually require mandatory post-processing. Moreover, support removal and other finishing processes can also weaken the structures with complex internal geometries.

Beyond AM, various conventional manufacturing processes have been utilized to produce bio-inspired structures depending on material selection and complexity; these include hand lay-up, VARTM, VARI, autoclave cure, manual winding, thermal and ultraviolet infusion, prepreg lay-up, compression moulding, filament winding, bladder moulding, freeze casting, biomineralization forming and pultrusion.

Despite the abundance of available traditional processes, the complexity of many bio-inspired geometries still poses fabrication challenges, and this is the reason why AM is increasingly considered to be the most suitable technique to duplicate extreme geometric complexity with acceptable precision and reproducibility.

1.4 Applications of Bio-Inspired Structures

Bio-inspired structures have become promising and competitive candidates for future impact-resistant applications, including helmets, undercarriage systems, planetary landers, body armor, and protective structures for automobiles. The inspiration from biological systems has encouraged the development of highly efficient and energy-absorbing structures that can be used in various engineering fields such as aerospace, transportation, and structural engineering. In these sectors, lightweight and impact-resistant designs are essential, since they can convert impact energy into deformation energy, protecting both occupants and equipment. Moreover, lightweight structures also offer superior properties such as a high strength-to-weight ratio, excellent toughness, and good damping characteristics.

To improve the performance of such lightweight designs, many researchers have developed novel structures directly inspired by biological features. in particular, bio-inspired architectures provide several advantages, including innovative geometrical design, high energy absorption capacity, enhanced heat transfer, and improved stiffness and toughness. For these reasons, emulating structures found in animals, plants, and other natural systems is considered a viable and effective approach for future energy absorption applications. Moreover, the cellular-type of bio-inspired structures present a special advantage: by altering the geometrical parameters of the structure, such as cell size and wall thickness, it is possible to obtain different mechanical responses.

In 2000 the bio-mimicking concept was employed for the first time to study energy absorption, a major milestone for this field of research. The bio-inspired methodology has since then made important contributions in the field of engineering, as each biological organism present distinct characteristics that can be utilized to develop new designs and efficient energy-absorbing systems.

Initially, the bio-mimicking method was not widely adopted due to some manufacturing limitations. However, with the rapid advancement of additive manufacturing, the mimicry of biological systems became more feasible, providing a promising path for future energy absorption applications.

Honeycomb structures inspired from natural cellular materials, for instance, are one of the best bio-inspired energy absorption, stiffness, and light weight performing architectures. These can be optimized and tailored in additive manufacturing by varying relative density, gradation, and aspect ratio to enhance their mechanical performance. While conventional, non-tailored honeycomb structures buckle and collapse globally, resulting in an abrupt loss of load-carrying capacity, in contrast, custom-engineered configurations, like re-entrant, irregular, or chiral geometries, experience localized buckling and progressive failure mechanisms, resulting in gradual and controlled energy absorption.

The introduction of geometric gradation of wall thickness allows efficient redistribution of stresses, preventing global collapse and allowing local deformation and energy dissipation. Consequently, tailored honeycomb structures allowed to improve the mechanisms of failure, preventing abrupt structural collapse and improving their effectiveness in impact energy absorption.

1.5 Challenges and Future Perspectives

Although the remarkable potential of bio-inspired structures across most fields of engineering, their real-world applications in industries can be limited by several major challenges. The main challenge is related to defects and non-uniformities that can significantly impact the mechanical response of produced structures. Additionally, the absence of low-cost and efficient manufacturing processes viable for large-scale production, makes it difficult to realistically produce bio-inspired designs. Therefore, despite the extensive research, bio-inspired engineering design is still a developing field that is not fully mature.
In order to overcome these limitations, the continuous progress in additive manufacturing and material characterization is expected to play a crucial role in the following years.
Advanced additive manufacturing techniques allow a precise production also of very complex geometries with increased reproducibility, opening new perspectives for the integration of principles of biological design into engineering solutions.

Another aspect that must be taken into consideration is that the bio-mimetic strategy requires interdisciplinary collaboration. Efficient bio-inspired systems are developed by integrating knowledge from biology, materials science, physics, chemistry, design, and manufacturing. Only through this multidisciplinary approach, bio-inspired methods can be converted to useful designs with improved mechanical and multifunctional properties. It is also required to improve the mechanical reliability of such structures by reducing internal defects and improving post-processing operations such as heat treatment and support removal, which otherwise debase the component's integrity.

The continuous evolution of additive manufacturing technology combined with new insights into the behaviour of biological systems will enable the development of highly efficient, reproducible, and cost-effective bio-inspired structures for industrial applications.

Ultimately, the studies on nature-inspired systems offer a long-term path toward the development of lightweight, energy-absorbing, and multifunctional structures that can meet the growing demands of modern engineering applications.

2 Biological Inspiration: *Fomes Fomentarius*

2.1 Fungus as Inspiration for Bio-inspired Structure

Evolution can be considered a natural design-like process, in which natural selection favours different traits that helps natural organisms to survive and prosper in their environments. In nature, multiple structures exhibit material properties that are tailored to their specific roles, in such a way that cannot be accomplished by their constitutive materials alone. As a result of this process, the natural world offers an multiple examples of natural structures where form and function are strictly related.

Many lightweight biological materials such as wood, bone, and silk for instance, present exceptional mechanical properties, such as strength, hardness, and fracture toughness that are critical for their physiological functions. The same can be said for many other materials that can be found in nature, and this wide range of properties, enables species to adapt and survive even in extremely challenging habitats.

However, while many natural materials and their structures have been extensively studied and characterized, other species, such as fungi, remain far less explored, with limited reports available on their structural and mechanical characteristics.
Although properties like strength and toughness are not usually associated to the body of a fungus, the variety of their biological materials is remarkably wide and thus, it can be expected that the multicellular fruiting bodies of fungi display a great variance, not only in their appearance and edibility but also in terms of remarkable material properties.

The fungal kingdom is very diverse; every year thousands of new species are discovered and documented, while millions are still believed to be discovered and described.
The structures of fungi, together with their inherent material, physical, and mechanical properties, hold a significant potential as a source of inspiration for the development of bio-inspired materials and structures.

2.2 Biological Role and characteristics of *Fomes Fomentarius*

Among the wide diversity of fungal species, this thesis focuses on the characterization of bio-inspired structure derived from the tinder fungus *Fomes Fomentarius*.

Fomes Fomentarius is a basidiomycete white-rot fungus from the family of Polyporaceae, which finds the perfect growing habitat on birch and beech trees of the Northern Hemisphere forests, where it grows on weakened or deciduous trees.
It gradually decomposes the tree it grows on, in a process that can continue for more than 30 years. By doing so, it holds an important biological function as it can release carbon and other nutrients that would otherwise remain sequestered by the dead trees. It also digest and breaks down all the main components of deadwood (lignin, cellulose and hemicellulose) allowing the wood to fully decompose, and prepares it for other organisms that cannot break down lignin on their own.

Outside the trees, the fungus is visible only through its large fruiting body: the reproductive structure of the mushroom, which serves to generate and spread spores.

The application of this fungus in the past were multiples:

For instance, the *Fomes Fomentarius* is also commonly known as *"tinder fungus"* or *"tinder polypore"*, from its former use as tinder for lighting fires rapidly.
Given its tough and leathery texture, it was very suitable to be used as material for clothes, leather-like vests, hats and bags, and in some countries such as Romania and Hungary, it is still used for this purpose, producing products with excellent mechanical durability.
Finally, it has also been employed for various medical purposes such as antiseptic wound dressings.

Figure 2.1: External view of *Fomes Fomentarius* [3]

Figure 2.2: Typical application of fungus *Fomes Fomentarius* [4]

2.3 Structural Features of the Fungus

Perennial polypores fungi such as the *Fomes Fomentarius*, usually present a light but strong and tough fruiting body, able to reach a diameter of up to 50 cm, and which is able to resist different natural disturbances, such as, for instance, impacts generated from falling objects (like tree branches), dynamic and static loading coming from animals, snow in winter times, or even the body weight of an adult human.

In order to withstand those forces, not only a strong connection to the tree is required, but also, the fruiting body must be characterised by a hierarchical structure which allows to achieve a very low density, combined with an remarkable specific strength.
With these characteristics, the *Fomes Fomentarius* represent a clear example that in nature, one structure often has to serve several functions but is still composed of only a few constituents.

More specifically, the fruit body, *"mycelia"*, of tinder fungus presents a hierarchical and isotropic structure characterized by open porosity (honeycomb-like) both on the nano and macro-length scales.
It is composed by four distinct macroscopic layers, each varying in thickness and microstructural features, namely:

- Crust
- Trama
- Mycelial Core
- Hymenium

In each layer, three main components are found:

1. **Mycelium**: it is the primary component that can be found in all layers. In each layer, it displays a characteristic microstructure differing in its orientation, aspect ratio, density, length of its branches.

2. **Hyphae**: it consists of hollow fibrous cells, mainly made of chitin (a polysaccharide) and from the Mycelium. In *F. fomentarius* three different types of hyphae can be found: vegetative, skeletal and binding hyphae, which build the macroscopic segments in the fruiting body differing optically, mechanically and chemically. The three types of hyphae shows distinctions in the dimension, with the vegetative hyphae having 2–4 μm in diameter, the skeletal hyphae with 2–8 μm, and the binding hyphae with 1.5–3.0 μm. The latter one, as the name suggests, it is capable of branching and of forming intimate interconnections.
   At the sub-millimeter level the hyphae produces different arrangement in the body of the fungus, decisive in shaping the mechanical properties: it has honeycomb structures in the hymenium, foam-like structures both in mycelial core and trama and solid in the crust.

   However, the exact distribution of the different types of hyphae within different regions of the fruiting body remains still unclear.

3. **Extracellular matrix**: it is the third fundamental component. It acts as a reinforcing adhesive that differs in each layer in terms of quantity, polymeric content, and interconnectivity.

2.3.1 Microstructure

The primary structural differences between the layers arise from different factors such as the density of the network, extracellular cement binding the hyphae, and the presence of a substantial hollow space in the hymenium.

Figure 2.3: Cross section of *Fomes Fomentarius* on a tree [3]

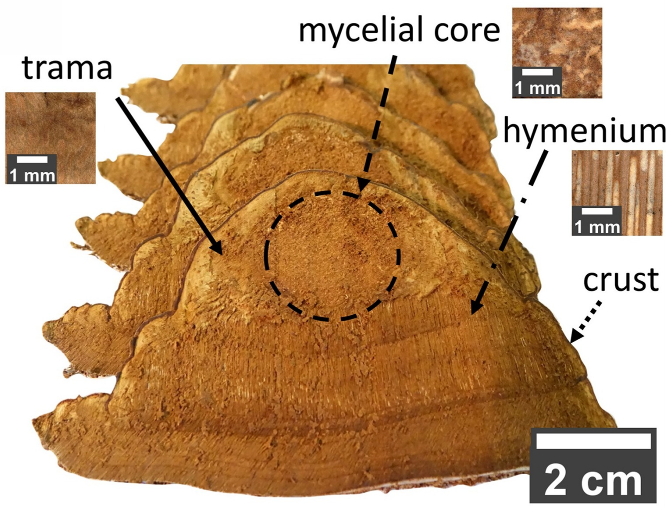

Figure 2.4: Internal Structure of *Fomes Fomentarius* [8]

Crust:

It is the exterior region of the fruiting body and consists of a hard and rigid protective layer. It has a dense and uniform structure, composed by compressed layers of hyphae, exhibiting the lowest porosity among all layers and lacking of visible microscale structural features. Here, the mycelium network is deeply embedded in an extracellular matrix that acts as a binding agent.
Crust thickness is generally not uniform, typically ranging from 900 μm at the posterior to 200 μm in the anterior region, with a characteristic porosity of around 19%. The upper surface of the crust is exposed to the external environment, while the lower surface is in contact with the trama, and in between, a densely compressed hyphal layer transition into a less dense zone, and toward the exterior part, a second thin dense layer lies below the rough outer surface.
Functionally, the crust serves as the primary barrier between the fruiting body and its surrounding. Moreover, its fracture toughness, together with padding abilities of the underlying trama, protect the mycelial core and hymenium from the environment.

Trama:

Subjacent to the crust, the trama is a foam-like, soft, and leathery layer. The interface between the two layers shows a gradual transition, with portion of the mycelial network remaining partially embedded within the same extracellular matrix found in the crust. This gradient progresses until the mycelium becomes entirely free of the extracellular matrix, and with the hyphae being partially aligned and oriented with branches extending up to several hundred micrometers.
The mycelium of the trama consist predominantly of skeletal hyphae approximately of 2 μm in diameter, forming a generally uniform mass with some denser areas, some of them probably containing binding hyphae, adding complexity to the microstructure. On

the sub-millimeter scale, the trama presents an homogeneous structure, with hyphae displaying a clear directional arrangement, each one running parallel to one another. The porosity of this layer is marginally lower compared to the one measured in the hymenium, with an average value of approximately 70%.

Mycelial core:

Positioned near the trunk and surrounded by the trama on the upper side, the mycelial core, together with hymenium, occupies the innermost region of the fruiting body. Within the fruiting body, this layer is the least structurally organized, comprising multiple regions that differ in porosity.
The hyphae present in this layer are of the generative (or vegetative) type - curved, thinner than skeletal hyphae (approximately 1–2 μm in diameter), and do not present any consistent orientation.

Functionally, the mycelium core has a fundamental role, serving as the interface through which the hyphae maintain the physical and physiological connection between the fungus and the tree.

Hymenium:

The hymenium represents the most dominant component of structural organization of the fruiting body, located beneath both the mycelial core and the trama layers, it accounts for about the 70% of the fruiting body.

Structurally, the hymenium is organised by a honeycomb arrangement, whose pores leads to to tubes that extend all the way across the structure up to the trama and can reach lengths up to 4 cm with diameters of around 200 μm. The orientation of the tubes is preferentially oriented and aligns with the gravitational force, resulting in a transversely isotropic structure, which will lead to a dependency of the response to mechanical load and deformation on whether load is applied parallel the tube axis or perpendicular to it. Having an overall porosity of about 70%-76%, the hymenium is the layer with lower density and higher porosity of the fruiting body.

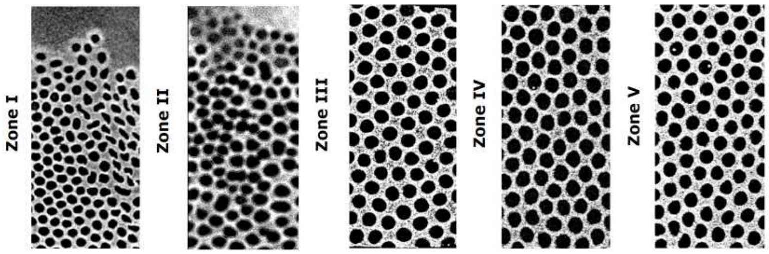

Figure 2.5: Cross-section of the hymenium tubes at different positions along their axis [7]

In a similar way to the crust, inside the tubes, the hyphal network is bonded by a small amount of extracellular substance, although in much lower concentration than in the outer crust and the hyphae are preferentially aligned along the tube axes, reflecting the structural anisotropy of the layer. Each tube directly shares its walls with the neighbouring tubes, without a distinct interface, its thickness is extremely low, being typically about 20 to 50 μm. These walls are made of relatively thick skeletal hyphae, typically 3–4 μm in diameter, which are often aligned parallel to the tube axis.
When observed at higher magnification, their arrangement reveals a fibrous microstructure. On the submillimetre scale, this material exhibit the characteristics of porous foam, with a relatively low porosity. Binding hyphae are interconnected with the skeletal hyphae, contributing to the integrity of the structure. Moreover, the hyphae themselves are hollow, which further increases the porosity of the hymenium.

The hymenium also has a fundamental biological role, as its hyphae release spores, necessary for fungi reproduction. The downward- facing tubular architecture facing the ground, increases the available surface area for releasing the spores facilitating their delivery into the environment. Typically, over the curse of a year, *Fomes Fomentarius* can develop up to three new layers of hymenium, which largely increase the spore production of the fruiting body reaching hundreds of million spores per cm^2 every hour.

2.4 Relevance to Engineering Design

In recent years, the fruiting bodies of F. fomentarius has attracted growing interest in the scientific community, mainly because of its mechanical properties such as the combination of lightweight and high toughness of the fruiting body. These characteristics make it an extremely interesting species for the development of advanced bio inspired materials and structure, especially where lightweight, high-performance and sustainability is a priority.

A unique aspect of the Fomes fomentarius is the way its internal structure is organised. Unlike many other fungi, it adopts an honeycomb structure, where the fibres are oriented along the direction of the honeycomb tubes. This arrangement allows the Fomes fomentarius to have a remarkable increase in compressive strength, especially of the hymenium,

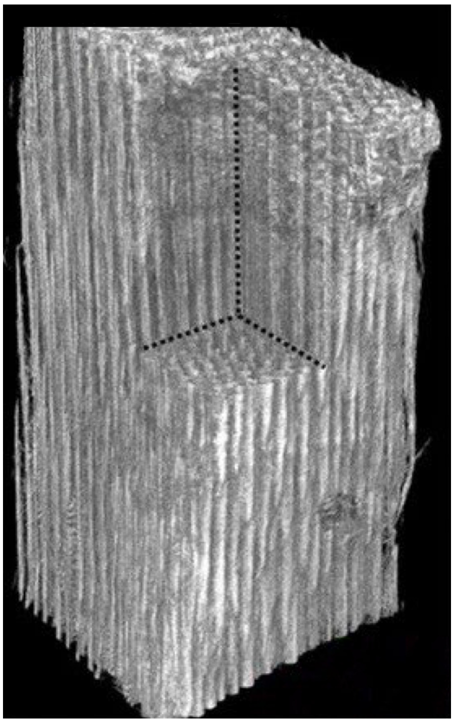

Figure 2.6: Anisotropic arrangement of mycelium tubes [6]

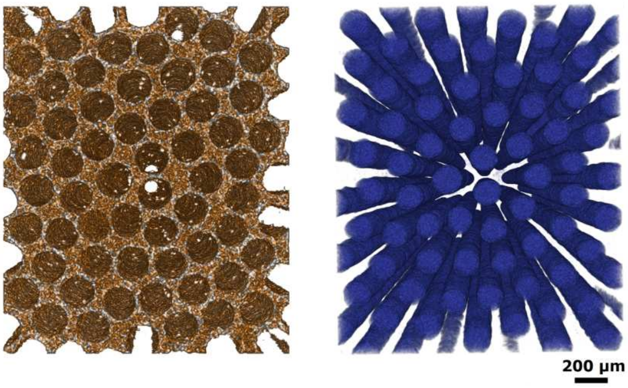

Figure 2.7: Cross-section of Hymenium and image of empty space of each tube (blue) [7]

where it can increase up to six time higher compared to similar fungi, demonstrating the potential of the mechanical performance of this structure.

Although these findings, the relation between their microstructure of the bracket fungi and their mechanical properties is still not fully understood, and the exact role of the different structural components of fruiting bodies are not yet clearly defined. What is known, is that, with the combination of a rigid and hard external layer, together with a lighter and porous core, the fruiting body presents a balanced trade-off between mechanical strength and reduced weight.

With these characteristics, F. Fomentarius is increasingly seen as a model system to design new composite materials and bio-inspired structures, which can find application in impact-absorbing and protective systems, packaging insulation applications, and multiple engineering fields like civil, aerospace, and building design.

2.5 Mechanical Characteristics

To investigate the mechanical properties of the fungus, I referred to the experimental study conducted by Ajit Kumar, Dominik Weil, Ernesto Scoppola, and Salima Bahri, who analyzed the tensile and compressive behavior of Hymenium tubes and the context layer.

In their experiments, a fruiting body of $Fomesfomentarius$ was collected from a birch trunk in Vantaa, Finland. The specimen had a volume of about 10 cm^3 and was dried by lyophilization. Afterwards, it was stored under normal laboratory conditions, and the fruiting body was separated into its main layers, such as crust, context or trama, H. tubes, and their interfaces.

Moreover, since the mechanical response of biological materials is strongly affected by humidity, all measurements were conducted at 50% relative humidity and samples were equilibrated under these conditions for 24 hours prior to testing to ensure consistency.

2.5.1 Tensile Test - Procedures and Results

For the tensile tests, 15 *mm* long, 2 *mm* wide strips of the *H.tubes* and *context* were cut. The measurements were conducted with a 5 *kN* tensile-compression module (Kammrath & Weiss GmbH, Germany) using 100 *N* load cells, a gauge length of 5*mm*, and an elongation speed of 2 $\mu m/s$. To prevent the specimens from slipping, their ends (at 5 *mm* from the edge) were secured between two pieces of abrasive sandpaper using an adhesive. .

The results are reported in Figure 2.8. Both the context and the *H.tubes* presented typical stress–strain curves. In particular, the *H.tubes* showed a yield curve with a positive slope until an instantaneous failure, while the *context* instead, displayed a more complex behaviour, with an initial failure after the elastic stage, followed by a jagged trace in the curve and a secondary failure.

In Figure 2.9 instead, are shown the graphics obtained from the test, together with a table collecting the values of Young Modulus, Maximum stress, maximum strain and toughness for both the *H.tubes* and the *context*. More specifically, for the *context*, the values of stress and strain shown in the graphics are the primary stress and the secondary strain, as they represent the higher value obtained for that properties for the *context*.

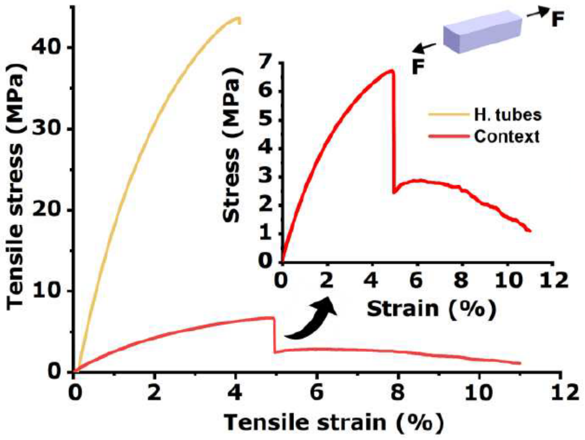

Figure 2.8: Tensile stress-strain curves for the context and the H. tubes [6]

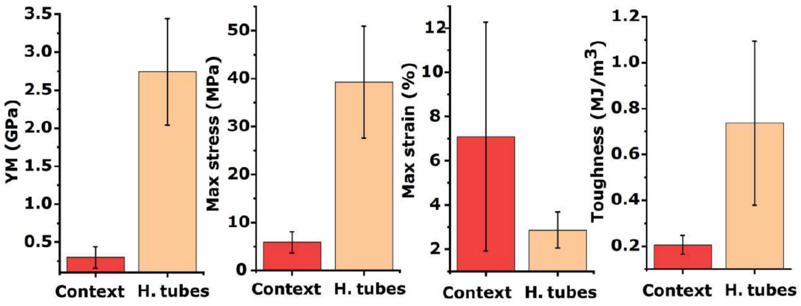

Figure 2.9: Mean values ± SD for stress, strain, Young's modulus, and toughness [6]

	H.Tubes	*Context*
Young Modulus [GPa]	2.7 ± 0.7	0.3 ± 0.13
Max Stress [MPa]	39.23 ± 11.7	5.8 ± 2.1
Max Strain	$2.8 \pm 0.8\%$	$4.3 \pm 2.6\%$,
Toughness [MJ/m^3]	0.73 ± 0.3	0.2 ± 0.05
Secondary Max Stress [MPa]	/	2.3 ± 0.84
Secondary Max Strain	/	$7.09 \pm 5.1\%$,

Table 2.1: Mechanical Properties of the H. Tubes and Context of the Fomes Fomentarius, obtained from the Tensile Test

As it is possible to notice from the data obtained, the H. tubes possess higher values in all the properties. The only exception is for the maximum strain, which is higher for the context (7.09 ±5.1%) compared to the H. tubes with of 2.8 ±0.8%.

After the tensile tests, the fractured surfaces of both layers were observed using SEM to study the deformation and failure mechanisms (Figure 2.10). Major differences were identified: the H. tubes showed blunt fracture surfaces with fewer pullout regions. Their mycelium network was able to carry higher loads without large plastic deformations, despite their high porosity and low density, resulting in higher strength and stiffness compared to the context, and also a higher toughness (0.73 ± 0.3 MJ/m^3 vs. 0.2 ± 0.05 MJ/m^3),but with the expense of lower tensile strain.

In contrast, the context maintained partial connections in the mycelium network even after secondary failure which explains the two-stage fracture behavior in its stress–strain curve. Under tensile load, the context resists deformation until the force overcomes the elastic limit of the interfacial matrix, causing the primary failure. It is then followed by the gradual sliding, stretching, and unfolding of bonds of the mycelium, which dissipates energy until the final catastrophic failure.

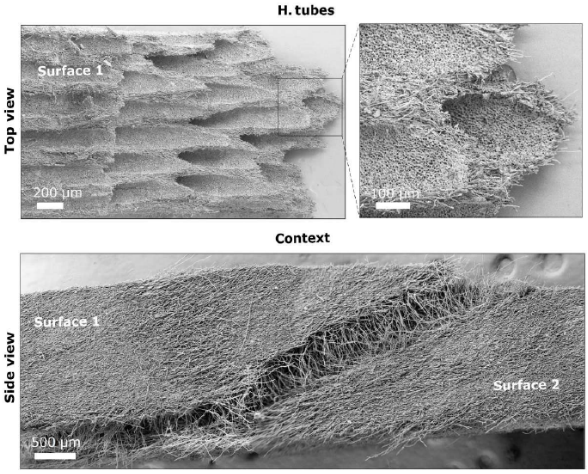

Figure 2.10: SEM images from the fractured surfaces after tensile tests to better identify [6]

2.5.2 Compression Test - Procedures and Results

Compression tests were also performed to better understand the effect of anisotropy and interfacial bonding in the mycelium network. In particular the tests were conducted both on the tubes and context either parallel or perpendicular to the orientation of the hyphae, and they were performed using a TA.XTExpressC Texture Analyzer (Stable Micro Systems) equipped with a 100-N load cell. Cylindrical samples of approximately 5 mm^3 were loaded with a flat-face probe of 5 mm diameter at a deformation speed of 2.5 μm/s until densification and catastrophic failure occurred.

The obtained results are shown in Figure 2.11 and Figure 2.12, and as expected, both layers showed higher compressive strength when loaded parallel to longitudinal axis of the hyphae. Moreover, thanks to their high orientation, the H. tubes reached about 8 MPa in longitudinal loading and 2 MPa in lateral loading, while the context reached only 1.8 MPa and 0.61 MPa in the same directions, confirming that the stronger orientation of H. tubes improves their resistance to compression.

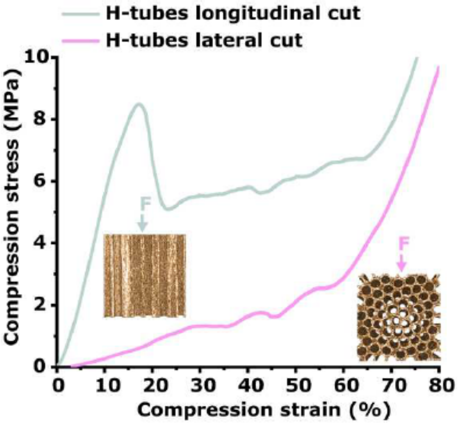

Figure 2.11: Compression Stress-Strain curve for H.tubes [6]

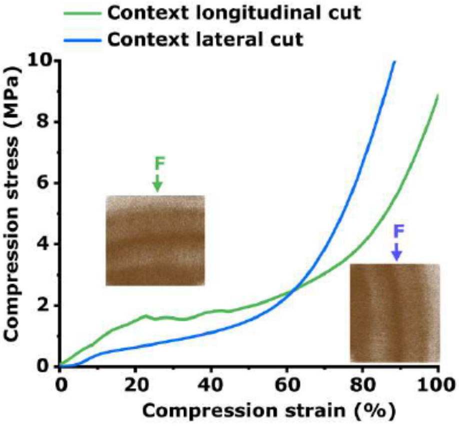

Figure 2.12: Compression Stress-Strain curve for Context [6]

Another important difference is the presence of an extracellular matrix in the H. tubes, which was not observed in the context. This matrix acts as a binder for the mycelium network, improving the mechanical properties.

To investigate the failure mechanisms, μCT imaging was performed on the compressed specimens, and it is reported in Figure 2.13 and Figure 2.14.
Under transverse compression, the H. tubes first absorbed energy by bending their walls, then cracks initiated and propagated along adjacent tubes. Under longitudinal compression, the H. tubes dissipated energy mainly through buckling, leading to deformation of the tubular structure along the longitudinal axis.

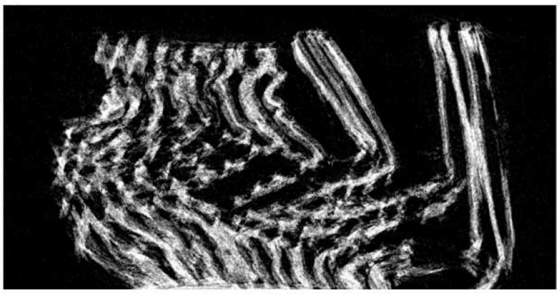

Figure 2.13: X-Y CT slice of the H. tubes cut longitudinally after compression test showing how the material dissipates energy through buckling effect. [6]

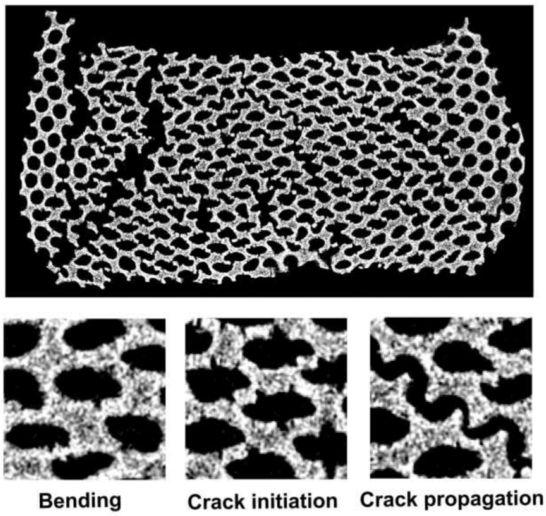

Figure 2.14: X-Y CT slice of the H. tubes cut laterally after compression test showing that the material follows sequential energy dissipating failure, including bending, crack initiation, crack propagation [6]

3 Design and Modeling of Bioinspired Structures

3.1 Methodology description

The aim of this work is to investigate the structural and mechanical performance of a bio-inspired architecture derived from the morphology of the tinder fungus Fomes fomentarius (described in Chapter 2). The methodology consists of comparing different materials, widely used in additive manufacturing, through finite element analysis (FEA) under static loading conditions.
More specifically, the study focuses on a cubic specimen reproducing the microstructural features of the fungus, which is subjected to both tensile and compressive tests.

In order to design the 3D CAD models whose performance is evaluated under high deformation, it is essential to define the type of simulations to be performed and the materials selected, all of which are representative of common additive manufacturing applications.

As it will be further detailed in Chapter 4, two main simulation strategies are adopted:

1. Tests on a single CAD specimen and varying the material
2. Test on three CAD specimens with equal mass varying the material

For the first case, the same CAD specimen, modelling the fungus structure, was tested in tension and compression. The material assigned to the CAD was systematically changed, in order to identify performance differences between materials, under same conditions.

For the second case instead, three different 3D CAD specimens having the same mass were tested. In this case, three different CAD models are needed, as the specimen dimensions will change according to the density of each material to ensure identical mass.

3.2 Material Selection

The fabrication of bio-inspired structures with complex architectures is extremely difficult when relying on conventional manufacturing processes. While traditional machining techniques such as CNC milling or metal arc welding can produce intricate components, they generally result in significant material waste due to their subtractive nature.

Additive manufacturing (AM), by contrast, offers higher flexibility for the design and fabrication of multiscale, multifunctional, and multi-material structures. This makes it a very attractive technology for bio-inspired systems, as they allow the reproduction of highly porous morphologies, such as those found in natural cellular structures and on the Fomes Fomentarius, which would be more difficult to manufacture through conventional methods, making the layer-by-layer deposition principle of AM more suitable for mimicking the detailed architecture of natural porous systems like the Fomes fomentarius.

This approach eliminates many of the geometric constraints of traditional manufacturing, allowing the production of components with complex topologies while reducing both cost and processing time. In addition, AM significantly lowers material waste, requires fewer machining steps, and reduces the dependence on highly skilled labor.

Several AM processes are currently available, including fused deposition modeling (FDM), direct ink writing (DIW), polyjet (PJ), stereolithography (SLA), selective laser sintering (SLS), selective laser melting (SLM), binder jetting (BJ), and powder-bed fusion (PBF). Many of these can be employed to replicate porous structures inspired by nature, ranging from honeycombs to lattice frameworks, for applications in biomedical implants, energy absorption systems, lightweight structural components, and soft robotics.
Additive manufacturing can be used with a wide variety of materials such as high-end engineering polymers, metals, ceramics and more.

In this study, three representative materials were selected for comparison:

- Titanium alloy Ti6Al4V,
- Aluminium alloy 6061-T6
- Acrylonitrile Butadiene Styrene (ABS)

These materials were chosen due to their extensive use in additive manufacturing, well-documentedd mechanical properties, and their relevance in engineering applications.

3.2.1 Titanium Alloy Ti6Al4V

Titanium and its alloys are some of the most widely used materials for additive manufacturing due to their excellent specific strength, corrosion resistance and biocompatible nature. These qualities make titanium ideal for aerospace and biomedical applications.
It is usually characterised by long production times and high machining costs of conventional processes. For this reason, titanium is very amenable to AM where material efficiency and less waste offer high cost advantages.

In the current research, properties of Ti6Al4V produced by Laser Engineered Net Shaping (LENS), or Directed Energy Deposition (DED) are considered and were taken by the research done by (Baranowski et al., 2019) [41]. The LENS process involves the utilization of a high-energy focus source (laser or electron beam) to melt the substrate and the metal feedstock (wire or powder) together, and then deposit and solidify layer by layer. Differently from the selective laser melting (SLM), DED does not use a powder bed and is therefore viable for repairing already formed parts or building complicated and expansive geometries.

Although DED has less precision ($\approx 0.25mm$) and poorer surface finish compared to powder-bed technologies such as SLM, it offers good mechanical properties, control of microstructure, and multi-material printing potential. Having the capability to combine additive and subtractive manufacturing processes in a single system further increases its applicability. Thus, Ti6Al4V produced by DED is an excellent choice for the investigation of lightweight, high-performance bio-inspired structures, and find applications in various industries such as automotive and aerospace

Density [kg/m^3]	4430
Elastic Modulus [GPa]	108.5
Poisson's ratio	0.3
Yield Stress [MPa]	710
Plastic Failure Strain	19%

Table 3.1: Mechanical Properties for Titanium Ti6Al4V

3.2.2 Alluminium Alloy 6061-T6

The second material chosen is Aluminium 6061 T6. Like steel, aluminium is a very popular engineering material with a density approximately one-third that of steel. Its specific strength, or strength-to-density ratio, which is a gauge of high specific strength, makes it good for designing light yet strong structures. Aluminium alloys exhibit high strength, corrosion resistance, and recyclability that are responsible for their enormous application in the automotive, aerospace, and maritime industries. Compared to other alloys such as AlSi10Mg, which may present higher castability and higher additive manufacturing suitability, Aluminium 6061 exhibits greater levels of application based on its compromise between machinability, strength, and flexibility in processing.

Aluminium 6061 was chosen specifically because it is one of the most popular alloys used in many applications such as structural, automotive, and aeronautical industries. It belongs to the 6xxx series of Al-Mg-Si alloys, which are precipitation hardenable systems reinforced with Mg2Si precipitates.. In the 6061 alloys family, the most prevalent is usually the T6 heat-treated alloy because of its corrosion resistance, weldability, and machinability.
T6 refers to a temper treatment which has been designed to attain maximum precipitation hardening and therefore yield strength, and allows to balance the typical aluminium elongation with high strength.

It is characterized by three phases:

1. **Solution Heat Treatment**: it consist in increasing the alloy temperature to 530–535°C, in order to homogeneously dissolve silicon and magnesium in the aluminium matrix and to avoid eutectic melting, which would compromise material strength.
2. **Quenching**: quenching is performed to maintain the homogeneous solution and avoid large precipitate formation. However, it can introduce residual stresses due to the rapid cooling
3. **Artificial Aging**: is performed by heating the alloy to approximately 177°C for 8–12 hours. This process creates precipitates that increase Brinell hardness and fatigue resistance.

In early stages, for additive manufacturing, 6061 T6 was first discovered to be less suitable for standard AM methods since it showed too much porosity and solidification cracking under processing. However, recent advancements, including the application of solid-state AM processes like additive friction stir deposition (AFSD) and alloy modifications through particulate additions, allow to overcome these challenges, allowing to develop a functional aluminium 6061 T6 alloy, with properties comparable to the conventionally produced alloy.

For example, researches like the one done by (Abhishek Mehta et al., 2021) [42] has established that alloying AA6061 with 1 wt% Zr and then manufacturing through laser powder bed fusion (LPBF) and T6 thermal treatment reduces solidification cracking and porosity considerably. Zr additions trigger the formation of Al3Zr precipitates, grain refinement, and stops columnar grain epitaxial growth. As such, AA6061 that is modified with Zr achieves improved printability ,near-full density, and its mechanical properties of yield strength, ultimate tensile strength, and elongation at failure are either similar or superior to those of conventionally processed 6061 T6.

LPBF process conditions were optimized to achieve relative densities of 99.7% at 350 W laser power, scan rate of 1400 mm/s, hatch spacing of 130 m, and a layer thickness of 30 μm. Traditional T6 heat treatment was equally effective in this sense, wherein the samples were solutionized at 500°C for 1 hour, water quenched, and artificially aged at 160°C for 10 hours, producing fine Mg2Si precipitates. Precipitation of Al3Zr and Mg2Si precipitates together in Zr-modified AA6061 achieved strengthening equivalent to traditional alloys while maintaining printability.

Entering more specifically in the LPBF process, it is a type of PBF (power bed fusion) process. It relies on the deposition of finely dispersed powder layers, well spread and solidified on a build platform. Inside each layer, the material is selectively melted by a concentrated laser beam, shaping the part. Successive layers of powder are then deposited and bonded to the previous ones until the final 3D component is finished. The excess powder is removed with a vacuum system, and further post-processing operations like coating, sintering, or infiltration can be used if needed to improve surface finish or material properties.

The process is best suited for powders with relatively low melting or sintering points that can be melted outright by the laser. Under situations where the melting point is too high, a liquid binder can be used as a substitute.
LPBF's advantages are found in its incredibly thin layer thickness, allowing to achieve high resolution and acute geometric accuracy in the final parts. More specifically, LPBF machines can typically achieve tolerances of ±0.05 mm for small components and about ± 0.1 mm for large components.

Another way of production of 6061 T6 parts through additive manufacturing is AFSD. It is a solid-state process operating below the melting point and therefore avoids defects typical of beam-based AM processes rely on a liquid solid phase transformation, such as porosity and hot cracking.
In AFSD, feedstock material is driven through a hollow rotating tool against a substrate. This leads to frictional heating, up to 60–90% of the melting point of the alloy, which softens the feedstock and enables plastic deformation. The softened metal is progressively deposited layer by layer and forms metallurgical bonds with neighbouring layers. The process mimics friction stir welding in terms of heat generation mechanics and plastic flow. AFSD avoids gas entrapment and hot cracking and reduces residual stresses, enabling the creation of fully dense components with fine microstructures, minimizing void formation. It is particularly ideal for creating large aluminum parts for the aerospace, automotive, and maritime sectors through its high deposition rate and resultant mechanical properties that are capable of equaling or even outdoing the original material. However, AFSD does not come without issues, such as oxidation during processing. Alumina oxide films lead to interlayers between deposited layers that form interlayer defects and reduce mechanical strength.

Practical applications of AFSD using AA6061 have been reported by (S.C. Beck et al., 2021) [39] and (Numan Habib et al., 2021) [38]. For example, in the first research, multilayer AFSD-constructed AA6061 underwent standard post-deposition heat treatment according to ASTM B918–B91820-M: the samples were solutionized at 565°C for 50 minutes, quenched in ice water, and artificially aged at 177°C for 8 hours. This developed T651-type mechanical properties, such as strength and hardness by strengthening phases reprecipitation. Results showed that AFSD-processed AA6061 could achieve strength, hardness, and ductility equivalent to T6 tempers in conventionally produced alloys.

Similarly, in second reference, (Numan Habib et al., 2021) [38], were collected studies that confirmed that mechanical characteristics of AFSD-produced 6061 are almost identical with those of conventional alloys. In particular, they also showed the dependence of this properties, microstructure and performance on the variations in processing parameters such as transverse velocity, feed rate, and tool rotation.

AFSD also enables the processing of aluminum alloys with a broader range, e.g., non-weldable aerospace alloys like 7075, due to its solid-state character. Despite issues induced by oxidation, AFSD remains one of the best AM processes for large, structurally demanding aluminium components due to its ability to generate fine-grained, defect-minimized microstructures.

Density [kg/m^3]	2716.6
Elastic Modulus [GPa]	68.9
Poisson's ratio	0.33
Yield Stress [MPa]	287
Plastic Failure Strain	8-13%

Table 3.2: General mechanical properties of Aluminium 6061-T6

3.2.3 ABS - Acrylonitrile Butadiene Styrene

The last material that was chosen is acrylonitrile butadiene styrene or ABS. it is one of the most common thermoplastic polymers that are being used in additive manufacturing, especially when using Fused Deposition Modeling (FDM). It is found to be of good toughness, impact strength, which are desirable characteristics for energy absorption. It also results easy to process and convenient for printing smaller parts with small defects. For these reasons and for ability to identify all the properties needed for numerical modelling, ABS was chosen for exploring bio-inspired structures on the polymeric level.

The data are reported in the following table, which was taken from the (Shakib Hyder Siddique et al., 2023) [47] research where an ABS component component was produced with FDM-based 3D printer.

Fused Deposition Modelling (FDM) is one of the most widely used additive manufacturing methods for thermoplastic polymers. Through this process, a continuous filament is exposed to a hot nozzle, where it is rendered semi-liquid before being deposited layer by layer onto a build platform or onto previously extruded layers. The thermoplastic nature of ABS allows the neighboring layers to be welded upon deposition and then solidify once cooled to room temperature.

The mechanical properties of printed parts are mainly dependent on process conditions such as layer thickness, filament width and direction, and air gaps within or between layers. Between these, interlayer distortion tends to be the primary source of mechanical weakness.

Standard FDM nozzles are generally in the 0.2 mm to 0.8 mm range, and smaller diameters are used when higher geometric resolution is required.

Some of the advantages of the FDM are low cost, rapidity of production and simplicity of the proces. It presents, however, some drawbacks, like sacrificed mechanical strength, perceptible layer-by-layer surface topography/appearance, poor surface quality , and a limited range of processable thermoplastics. The incorporation of reinforcing fibres into polymeric filaments has been shown to improve mechanical properties. However some problems are still present in fibre orientation control, fibre–matrix adhesion strength, and avoidance of voids occurring within printed structures.

Density [kg/m^3]	1068
Elastic Modulus [GPa]	1.85
Poisson's ratio	0.35
Yield Stress [MPa]	36
Plastic Failure Strain	4.7%

Table 3.3: Mechanical Properties of ABS

3.3 CAD

As described in Chapter 2, within the fungal microstructure the hymenium represents the dominant component of the fruiting body, accounting for about 70% of its volume. In addition, it is the mechanically strongest part, showing higher structural properties compared to the other layers. For this reason, and because the hymenium is also the most clearly defined microstructural layer, characterized by a honeycomb-like arrangement of tubes, the specimens tested in this work were designed to reproduce the hymenium structure, without replicating all the layers of the fungus, which would require different manufacturing techniques at multiple length scales.

To best reproduce and study the behaviour of the biomimetic structure under static analysis, a cubic specimen was selected. This specimen was designed with through-holes arranged in a hexagonal honeycomb pattern. The reason of this choice is that, as shown in Figure 3.1, the distribution of the hymenium tubes usually follows an hexagonal arrangement, as it is highlighted in the image. For this reason, the same pattern was adopted in the CAD model.

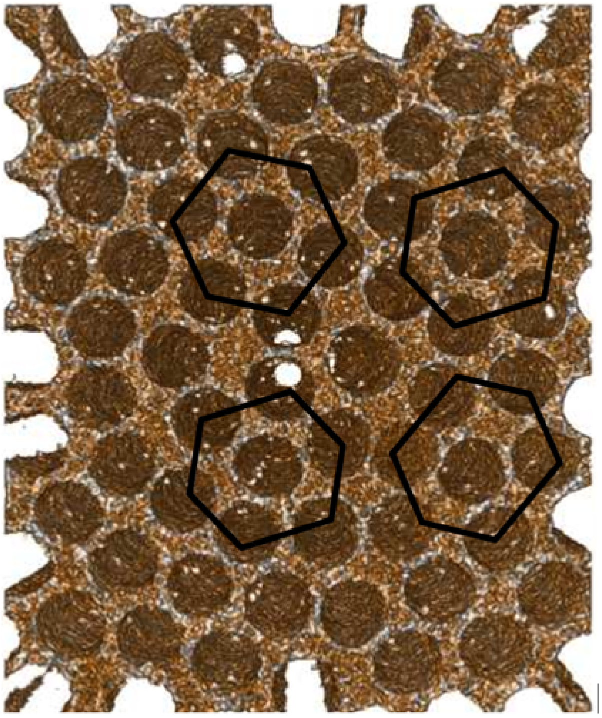

Figure 3.1: Hexagonal arrangement of Hymenium Tubes [6]

The CAD model was developed using Autodesk AutoCAD 2026, and the general steps for constructing the specimen are reported below, and the resulting model is shown in Figure 3.3:

1. Create a cube with the "BOX" command and set the dimensions.
2. With the "CYLINDER" command, draw a cylinder at the centre of the lower face of the cube. The radius and the height of the cylinder must be imposed and they correspond to the desired hole diameter and the cube's height.
3. Using the command DRAW → POLYGON and settin the number of sides to 6 it is possible to draw a hexagon inscribed in a circle whose radius is equal to the distance between the hole centres, and its centre point is positioned along axis of the initial cylinder. The vertices of the hexagon, will help to find he position of other cylinders and create the hexagonal patter of the honeycomb.

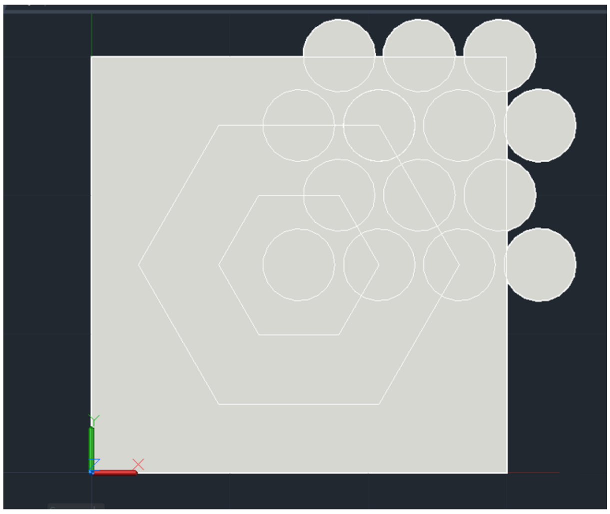

Figure 3.2: Hexagonal distribution of the cylinders

4. With the ”ARRAYRECT” command, is possible to create a rectangular array of cylinders, defining the spacing along the vertical and horizontal directions. This allows to replicate multiple cylinders without having to design each one manually.
5. Similarly, using the ”MIRROR” command to a reduced set of cylinders that cover one quarter of the cube face, it is possible to extend the pattern to the entire face, making the process faster and more efficient.
6. Before subtraction, the ”EXPLODE” command is applied on all cylinder groups created with ”ARRAYRECT” and MIRROR command, since these are treated as a single entity. Exploding them ensures that each cylinder can be considered individually, and this is a step without which would not be possible to proced with the next step.
7. Finally, with the ”SUBTRACT” command all the cylinders are removed from the cube, obtaining the final honeycomb structure shown in the figure below.

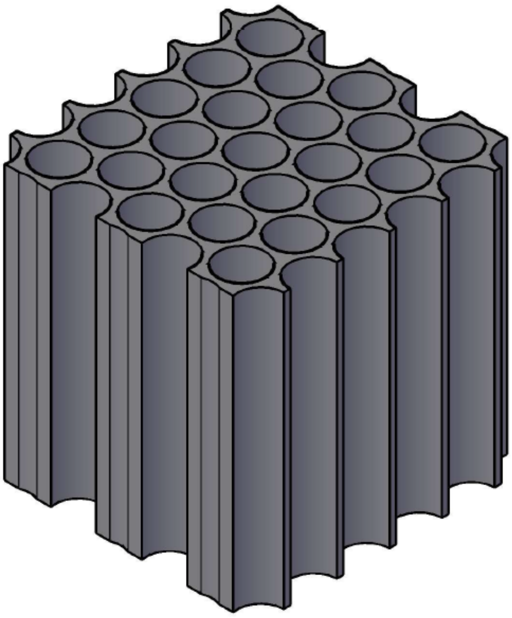

Figure 3.3: Final 3D-CAD model of the bio-inspired specimen

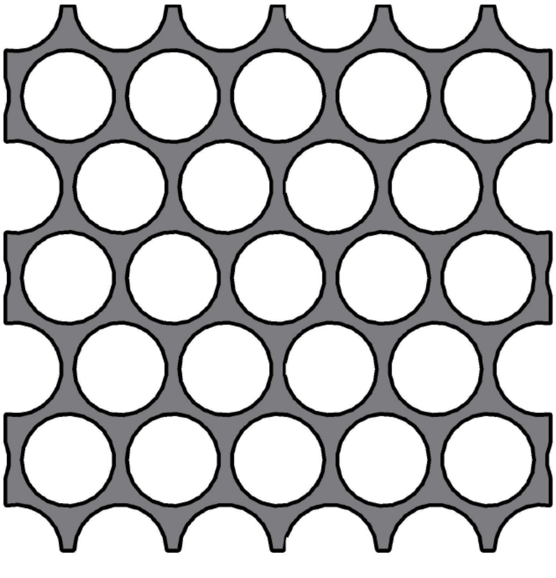

Figure 3.4: Top-View of the 3D Model

These steps are general and were followed for the design of every specimen used during the Finite Elements simulations. As explained in Section 3.1, multiple specimens had to be designed, varying the cube size, hole diameter, and spacing between holes. In total, three different specimens were created.

In designing the specimen, the porosity was kept at around 70%, which corresponds to the values typically found in the Hymenium of the Fomes Fomentarius. This choice follows the biomimetic approach, according to which, when mimicking natural structures, the relative density of the engineered model should remain close to that of the natural reference. In this way, the comparison between the artificial structure and the biological source can be considered more reliable.

For the first simulation case, where the same CAD model was used, varying only the materials, the cubic specimen was designed with the dimensions reported in Table 3.4.

Side's Size	**Hole Diameter**	**Hole-Hole Distance**	**Porosity**	**D/p Ratio**
30 mm	5.2 mm	5.8 mm	72%	0.897

Table 3.4: Parameter of the specimen

The size, hole diamtre and distance, and porosity of the structure, are shown in the table. In addition, a standard geometric check was carried out, ensuring that the ratio $D/p \leq 0.9$, where D is the hole diameter and p is the centre-to-centre distance between adjacent holes. And as we can see this condition was respected.

For this specimen, an important detail must be mentioned. In this first specimen, a portion of the cylindrical holes at the cube edges was kept. Their depth reaches about $0.2mm$, which is a feasible detail for the additive manufacturing techniques previously discussed, and it is shown in figure 3.5

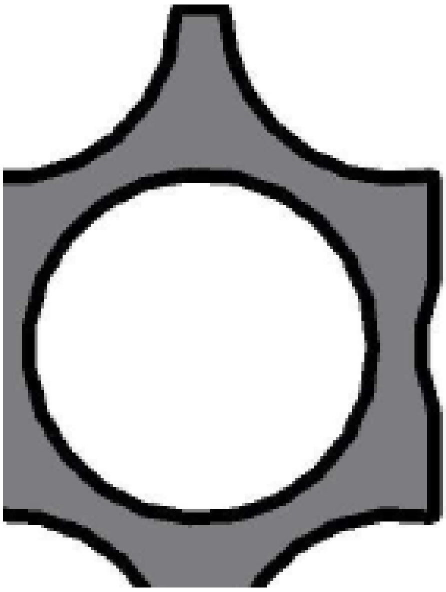

Figure 3.5: Detail of a portion of a through-hole at the side of the specimen

In the second simulation case, instead, three CAD specimens with the same mass were compared under tension and compression. The mass of the ABS specimen was taken as reference and was then kept constant. This choice was made as it allowed the ABS model to remain unchanged, avoiding the need to design it again; and also, being the ABS the material with the lowest density among the three materials, it resulted in the new aluminium and titanium specimens having smaller dimensions compared to the ABS one. This reduced unnecessary computational effort that would otherwise be required in FEM analysis if aluminium or steel had been taken as the mass reference.

The new dimensions of the two new specimens were calculated in the following way. Starting with the reference mass of the ABS specimen, defined as:

$$M = \rho \cdot V \tag{3.1}$$

where ρ is the density of the ABS and and V is the solid volume of the specimen, the reference mass of the ABS specimen is 7.99 g.

This value was then used as the target mass for the other specimens. By fixing the porosity at about 70% and using this mass, with the following calculation:

$$M_{\text{ref}} = \rho_{\text{material}} \cdot V_{\text{new}} \cdot (1 - \text{Porosity}) \tag{3.2}$$

it was possible to retrive, using first the density of aluminium, and then the density of titanium, V_{new} which represent the new total volume for the aluminium specimen and titanium specimens respectively.

In particular, starting with the aluminium specimen, from the value of the volume V_{new} obtained, the new side length of the cube was evaluated, which would be 21.42 mm. In practice, the side was rounded to 21.5 mm to simplify both the design and potential additive manufacturing production, giving a total volume of: $9938.375mm^3$ (21.5 x 21.5 x 21.5 mm).

With this new value of the cube's side, a proportional scale factor between the new and the original specimen was calculated. This factor was then applied also to the hole diameters and their spacing, obtaining the final dimensions of the aluminium specimen. In particular, the scale factor for aluminium was found to be 0.716, and the new geometric parameters reported in Table 3.5 .

Based on the updated specimen parameters, the application of the Aluminium 6061-T6 density to the net solid volume gives a total mass of 7.74 g with a porosity of 71%. The difference from the reference ABS specimen mass (7.99 g) is approximately 3% for the mass and 1.4% for the porosity, which, in both cases falls within an acceptable range.

Side's Size	Hole Diameter	Hole-Hole Distance	Porosity	D/p Ratio
21.5 *mm*	3.7 mm	4.15 *mm*	71%	0.892

Table 3.5: Parameter of the new Aluminium 6061 - T6 specimen

The same procedure was used in order to determine the size of the titanium specimen. In this case, the new cube side was determined to be 18.2 mm, corresponding to a scale factor of around 0.606. The following is the geometric data of the titanium specimen:

Side's Size	Hole Diameter	Hole-Hole Distance	Porosity	D/p Ratio
18.2 *mm*	3.1 *mm*	3.5 *mm*	70%	0.886

Table 3.6: Parameter of the new Titanium Ti6al4v specimen

Similarly, for the new titanium specimen,the application of the Titanium Ti6Al4V density to the net solid volume gives a total mass of 7.91 g with a porosity of 70%. The difference from the reference ABS specimen mass (7.99 g) is approximately 1% for the mass and 2.6% for the porosity, which, again, in both cases falls, within an acceptable range.

The 3D CAD model resulting from this calculations is shown in the figure below. Since the new specimens have the same geometric features and the software does not clearly show the small dimensional differences, only one is shown.

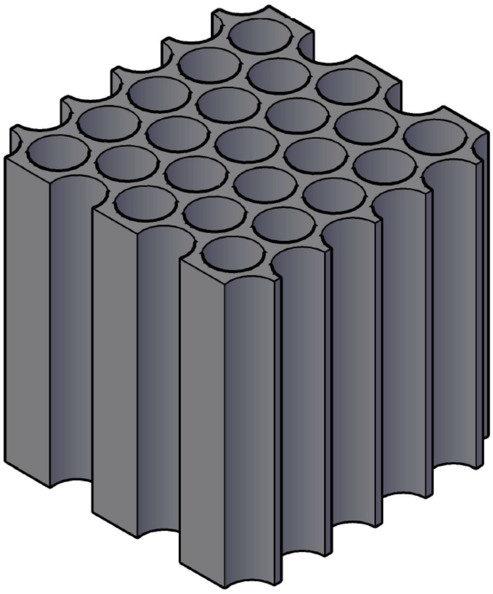

Figure 3.6: 3D CAD model the new Titanium Ti6al4v modified specimen in order to obtain the same mass of the ABS specimen

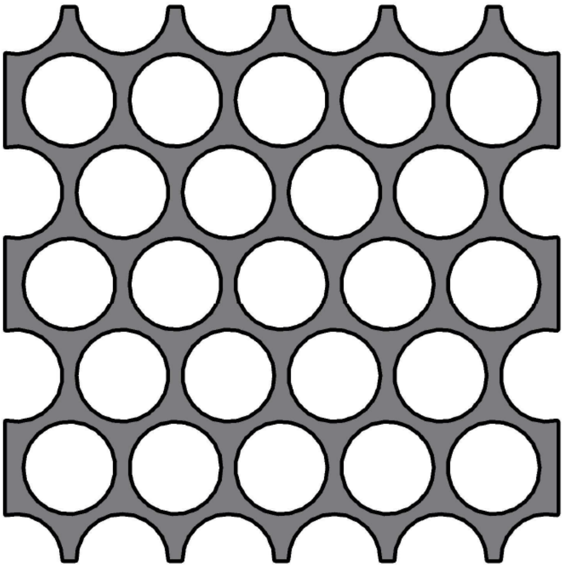

Figure 3.7: Top view of 3D CAD model the new Titanium Ti6al4v specimen

An important difference can be observed between the new specimens and the previous one. As mentioned earlier, in the first model a small detail was present at the edge of the cube, corresponding to a partial section of a hole. In the new specimens, however, this feature is no longer included. This change is a consequence of the reduction in specimen size required to maintain a constant mass. For these new models, the depth of this detail would have become extremely small, making it difficult, or even impossible, to reproduce with the additive manufacturing techniques previously considered. For this reason, the detail was removed from the new models.

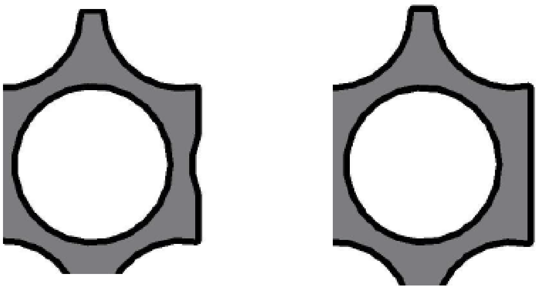

Figure 3.8: Comparison between the geometrical detail at the cube edge in the first specimen (left) and in the new specimen (right). The small edge detail visible in the first model was removed in the updated version due to the size reduction required to maintain constant mass.

In the following table, a summary of the main parameters of the three different specimens is reported to provide a clearer comparison of their differences.

Table 3.7: Summary of parameters of the three specimens used for FEM simulations

Parameter	**Specimen 1**	**Specimen Aluminium**	**Specimen Titanium**
Side's Size	30.0 mm	21.5 mm	18.2 mm
Hole Diameter	5.2 mm	3.7 mm	3.1 mm
Hole-Hole Distance	5.8 mm	4.15 mm	3.5 mm
Porosity	72%	71%	70%
D/t	0.897	0.892	0.886

4 FEM Analysis

4.1 General Review of FEM Analysis

Finite Element Analysis (FEA) is a numerical simulation technique that uses the Finite Element Method (FEM) to compute approximate solutions of the partial differential equations describing physical phenomena in most engineering fields, such as structural mechanics, fluid mechanics, thermodynamics, and electrostatics. The method works by simplifying these complex differential equations into a simpler system of linear algebraic equations.

The main idea behind FEM is the discretization of a complex domain into a finite number of smaller and simpler elements like triangles or quadrilaterals in two dimensions, and tetrahedra or hexahedra in three dimensions. These elements are connected through nodes, each associated with degrees of freedom that describe possible displacements or other physical quantities. Together, the elements and nodes form the computational mesh. The mesh can also be refined in certain areas, for instance where the geometry is more irregular or where higher stresses are expected, to obtain better accuracy.

Historycally, FEM was developed from the need to solve complicated structural problems in aeronautical and civil engineering. Even though that more elementary structural elements were introduced in the 1930s by researchers like A. R. Collar and W. J. Duncan, and the concept of dividing the integration domain into subdomains of easier nature were conceived by A. Hrennikoff and R. Courant, formal beginning of the modern FEM is generally dated to the mid-1950s. This was the period when the first formal FEM process, or "Direct Stiffness Method," came into being and was refined by M. J. Turner and co-workers.
Significant subsequent developments further improved the technique's mathematical basis and flexibility.

For example, B. M. Irons developed the concept of the isoparametric element, which significantly improved the method's flexibility in handling curved geometries. R. J. Melosh provided a consistent theoretical foundation on the basis of variational form of the FEM, providing it with mathematical validity. This development led to the dissemination of the early FEM codes and eventually the extensive range of sophisticated commercial codes available today.

The usual process of a finite element analysis (FEA) consists of three main steps:

1. **Pre-processing**: This is where the mathematical model of the system is built. It involves importing or defining the geometry, defining material properties, selecting the analysis type (static, dynamic, linear, nonlinear), applying boundary conditions (loads and constraints), and defining the mesh. During this step, the infinite degrees of freedom of the continuum are mapped to a finite number depending on the mesh nodes.

2. **Processing (Solving)** : in this stage the governing equations are solved numerally. Within each element, the unknown field (like displacements in structural mechanics) is approximated by interpolation functions, also referred to as shape functions. The problem is then condensed to an algebraic system whose solution has the nodal degrees of freedom as unknowns. A specialized solver then computes the solution.

3. **Post-processing**: in this step, the results are interpreted and expressed. Depending on the analysis type, this may include stress and strain distributions, displacements, reaction forces, or other suitable physical quantities.

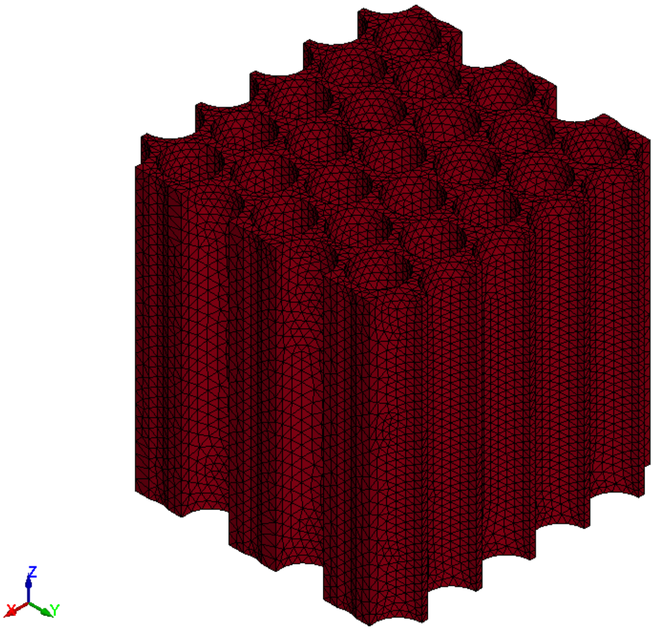

Figure 4.1: Final meshed 3D-CAD model of the bio-inspired specimen

Graphical visualization tools enable qualitative understanding, whereas numerical data enable detailed quantitative analysis. FEM is universally accepted because of its versatility. It can handle complex geometries, multiple materials, and numerous physical problems, and together with its availability within CAD and CAM packages, FEM has become a very common engineering tool. One of its most significant advantage is the capability to reduce the number of physical prototypes needed since many design choices and optimizations are done directly through simulation.

In this work, the finite element analysis of the test specimen was conducted using commercial software called LS-DYNA (Ansys). The software package is composed of LS-PrePost, used in the pre-processing and post-processing stage, and LS-Run, that is a solver.

4.2 Pre-Processing

4.2.1 Model Definition on LS-Dyna Software

As explained in the previous section, a Finite Element Method (FEM) analysis is usually divided into three main stages: pre-processing, processing, and post-processing.
The aspects related to the geometry definition, material selection and properties definition have already been described in Chapter 3, where three cubic cells with hexagonal honeycomb holes pattern were modeled in AutoCAD 2026. For the simulations, Titanium, Aluminium, and ABS were selected as materials.

The next step, in order evaluating the mechanical behaviour of the structure, consists in preparing a finite element model that can accurately reproduce the behaviour of the specimen under quasi-static loading. This stage is carried out within the LS-Dyna PrePost interface and it represent a fundamental step to ensure reliable results from the LS-Run solver. One of the main difficulties of this phase lies in modelling the boundary conditions and loads, since they strongly influence the outcome and if not properly defined may lead to incorrect results.

The procedure begin with the importation of the 3D CAD geometry into LS-PrePost, followed by the creation of a sufficiently fine mesh. Meshing can be done directly in LS-Dyna, but in this work the software HyperMesh was employed. Once the mesh was generated, the model setup continued with the selection of keywords. In LS-Dyna, keywords are command groups in which is possible to insert and define parameters for properly building a realistic numerical model like for instance material parameters, or other values for pre-defined options (flags) that enable or disable specific features. The data entered in the keywords are then stored in a .key (.k) file, which is essentially a text file containing the instructions to be executed by the LS-Run solver.

A list of the keywords used in the FEM model is reported in Figure 4.2 and Figure 4.3, as it appears in the LS-PrePost interface. From the figure, it is already possible to notice that different sets of keywords were applied depending on the type of loading (tension or compression) to obtain more accurate simulations.

The chosen keywords will be now described in more detail, underlining the most relevant parameters and highlighting the differences introduced between compression and tension cases, as well as between horizontal and vertical load applications.

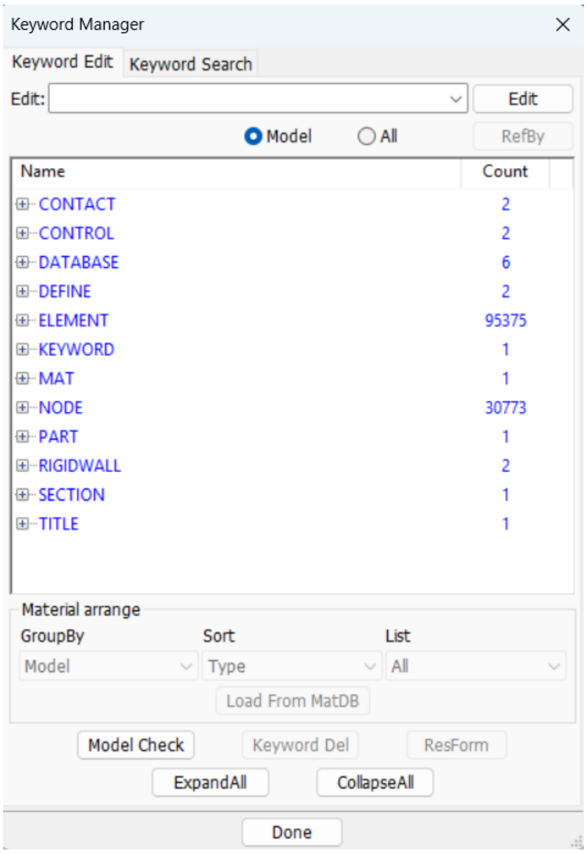

Name	Count
CONTACT	2
CONTROL	2
DATABASE	6
DEFINE	2
ELEMENT	95375
KEYWORD	1
MAT	1
NODE	30773
PART	1
RIGIDWALL	2
SECTION	1
TITLE	1

Figure 4.2: LS-Dyna keyword list for compression test

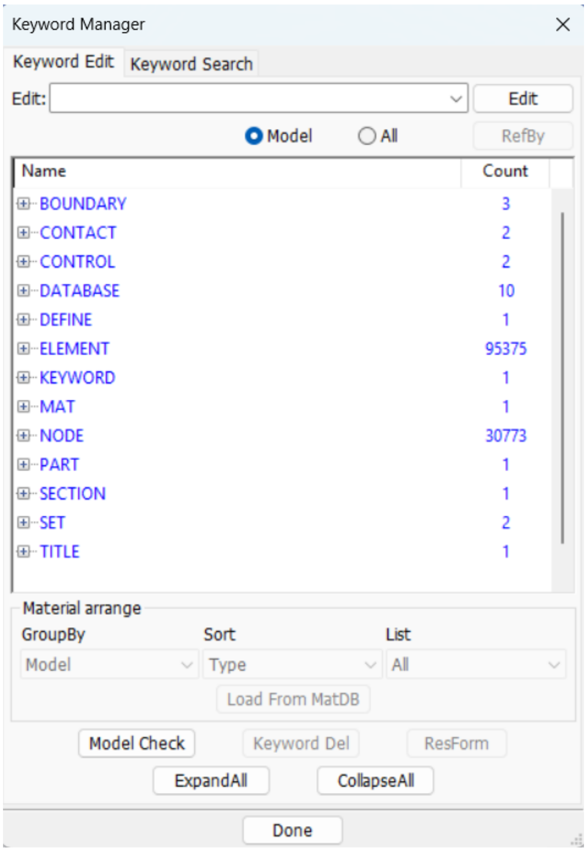

Name	Count
BOUNDARY	3
CONTACT	2
CONTROL	2
DATABASE	10
DEFINE	1
ELEMENT	95375
KEYWORD	1
MAT	1
NODE	30773
PART	1
SECTION	1
SET	2
TITLE	1

Figure 4.3: LS-Dyna keyword list for tension test

CONTACT AUTOMATIC SINGLE SURFACE: In the model, this keyword allowed to define the contact interactions between the honeycomb walls to prevent unrealistic overlapping of the cube elements. This configuration also corresponds to the option recommended in the LS-Dyna manual for cases where contact occurs with a single surface, such as between each rigid wall that was used to compress the specimen and the cell. In this keyword, the default software settings were maintained.

CONTACT ERODING SINGLE SURFACE: It was selected to address the complex issue of internal contact, which inevitably occurs during the collapse and densification of the cellular structure. In honeycomb-like or foam structures, when compression progresses to failure and subsequent crushing, different portions of the same component inevitably come into contact with each other, and this keyword takes it into account in a proper way. Also in this case the default values are kept.

CONTROL TERMINATION Since the analysis was conducted with the explicit solver, which computes the solution as a time evolution, it was necessary to define the final simulation time within the ENDTIM box. In particular it was selected as 0.01 s. And this values was sufficient to simulated a quasi-static experiment correctly. Even if apparently the ENDTIME may seem extremely small, in simulation of quasi-static load cases, the use of real-time loading is impractical due to the excessively long computation time. For this reason, the speed of the loading head must be increased to reduce the total simulation time while still ensuring reliable results.

CONTROL TIME STEP: The CONTROL TIMESTEP keyword plays a fundamental role in explicit analyses, since it is directly connected to the concept of mass scaling, which consist in adding a small amount of non-physical mass to the structure, allowing the use of a larger time step in the explicit simulation and therefore reducing the total computational time.

As it specified in LS-Dyna manual, adding artificial mass inevitably affects the results, because it alters the basic principles of dynamics. However, in certain situations, like in the case of quasi-static simulations, as in the present work, the effect is negligible, and mass scaling becomes acceptable. In quasi static simulations the kinetic energy remains very small compared to the internal energy of the system. This condition must be verified before proceding, through the energy plots provided as part of the LS-Dyna outputs, as shown in Figure 4.4.

To achieve the required quasi-static condition, it was necessary to assign a proper value to the parameter DT2MS. Following the guidelines on LS-Dyna Support, this value was set to a negative number. In this way, additional mass is introduced only into those elements whose natural time step would be lower than the absolute value of DT2MS. On the contrary, a positive value would affect all the elements equally, either by adding or subtracting mass, leading to an identical time step for the whole model. However this latter method is not recommended, and was therefore avoided. For this work, the selected value of DT2MS varied depending on the material and the specific simulation. For each case, it was checked that the kinetic energy remained negligible when compared to the internal energy, confirming that the analysis could be considered quasi-static. Figure 4.4 shows an example of this verification for the aluminium specimen.

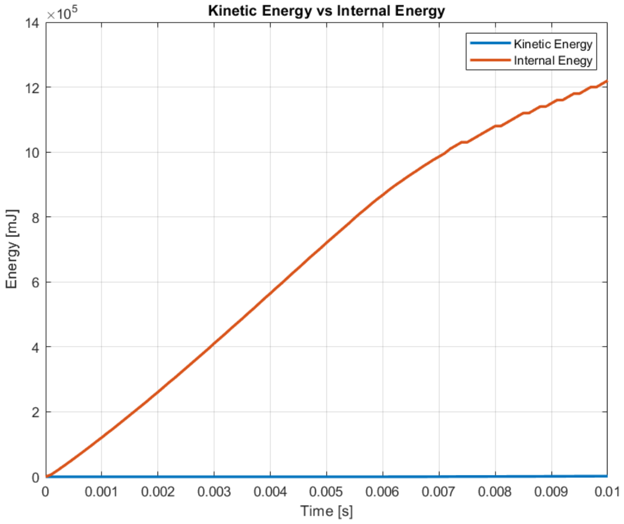

Figure 4.4: Kinetic Energy vs Internal Energy

DATABASE ASCII OPTION: This option is used to extend the simulation output by including additional quantities of interest. These values are stored as ASCII files, which are directly readable and visualizable in the LS-PrePost interface, under post-processing of LS-DYNA. Alternatively, one can also generate a binout file for the same additional variables. To do so, the corresponding boxes must be checked in the setup menu and the BINARY option selected from the dropdown list.
Among the various quantities added in this work, the most relevant were GLSTAT, which allows verification of the difference between kinetic and internal energy (confirming that the analysis was truly quasi-static), and for the compression case, the RWFORC and RBOUT outputs. These enable the visualization of the RIGIDWALL reaction force and the imposed displacement against the specimen, respectively.
For the tension case, the most important parameters are SPCFORC and NODOUT, which record the applied forces on the node set and the corresponding displacements in the loading direction. These outputs are essential for later evaluating the stiffness and generating the stress-strain curves derived from the simulations.

DATABASE BINARY D3PLOT: This is the main output file containing the complete set of simulation results at each time step. The D3PLOT file provides a detailed representation of the evolution of stresses, strains, and displacements throughout the model during the entire analysis process.

DATABASE EXTENT BINARY: This additional option extends the set of results stored in the D3PLOT file by including extra quantities, which are not saved as separate files but embedded directly in the binary output. Among these quantities, particular attention was given to the strain components, which can be activated by setting the corresponding flag STRFLG = 11. The value of STRFLG is obtained as follows:

$$STRFLG = L + M \cdot 10 + N \cdot 100 \tag{4.1}$$

where: L enables the writing of the strain tensor data to d3plot, elout, and dynain files, M enables the plastic strain data, N enables the thermal strain data. In this study, a value of STRFLG = 11 was selected, meaning that LS-DYNA was set to record both total and plastic strain tensors, while thermal strains were not considered.

DATABASE HISTORY NODE SET:Although the DATABASE BINARY D3PLOT is the primary reference for visual output and field analysis, the quantitative validation of the mechanical behavior under quasi-static conditions requires high-resolution dynamic data. The keyword DATABASE HISTORY NODE SET is used to define a restricted set of nodes from which precise time histories of nodal variables, such as displacements and reaction forces, can be extracted and written to dedicated history files. The main goasl of this keyword are: to track the nodes subjected to the imposed motion (defined through BOUNDARY PRESCRIBED MOTION SET) in order to record the exact evolution of the total applied displacement, which serves as the independent variable in the subsequent analysis; and to monitor the constrained nodes (for example, those fixed by single point constraints, SPC) and accurately record their reaction forces, which represent the dependent response of the system.

DEFINE CURVE: The DEFINE CURVE keyword is used to create curves that can be linked to other commands throughout the simulation. It is an essential tool in LS-DYNA, as it allows the definition of relationships between variables such as force, displacement, stress, and time.For example, a curve can represent the experimental stress-strain behaviour of a material and be connected to the material model to achieve more realistic results. It can also be used to define the time-displacement relationship that will be imposed to the RIGIDWALL motion during compression, or the displacement applied to node sets during tension tests.
In this study, the motion curve was defined as a straight line starting at the origin and passing through a point characterized by: an abscissa equal to the end-time defined in the CONTROL TERMINATION keyword, and an ordinate equal to the final displacement or deformation desired for the specimen at that specific time. This simple definition allows for a uniform and controlled displacement throughout the simulation.

ELEMENT SOLID: This is a keyword that is automatically generated by LS-DYNA after importing of a meshed model with solid elements. In the present work, the models were discretized in terms of tetrahedral elements, and the ELEMENT SOLID keyword gives the number of elements in the mesh.

MAT 003 PLASTIC KINEMATIC: The MAT 003 PLASTIC KINEMATIC material model was selected to properly model the behaviour of the ABS polymer used in the simulations. This model is designed for isotropic and kinematic hardening plasticity and can also include strain rate effects. It is widely used because it provides a good balance between computational efficiency and accuracy, and it is available beam, shell, and solid elements. The choice of this model was supported by literature findings (Shakib Hyder Siddique et al., 2023) [47], which demonstrated that simulations performed using MAT 003 produced results in very good agreement with experimental data, validating the suitability of this model for ABS polymers. This model proceeds accounting, however, some assumptions, such as:

- Simulations were carried out assuming perfectly plastic material for the loading phase.
- Manufacturing defects that are usually introduced as a result of the 3D-printing process, such as warping or irregular surface features, were not explicitly modelled, but such kind of imperfections may occur in printed specimens.
- The structure was assumed to be isotropic, and any material anisotropy caused by the additive manufacturing process was not considered.
- A uniform relative density was assumed, while in reality minor variations may occur due to microporosity between printed layers.

Moreover, a specific discussion is required regarding the failure criterion used in this model. To simulate specimen failure, a particular flag must be defined: “FS”, which represents the failure strain for eroding elements. This parameter determines when elements are removed from the computation, effectively simulating fracture. However, as observed in many studies, the value assigned to ”FS” in numerical models often differs from the experimental failure strain obtained from real tensile tests. This adjustment is necessary to correctly reproduce the overall behaviour of the polymer during large deformations. For ABS, the experimental failure strain typically ranges between 5% and 7%, while the most accurate simulations, in the literature, are obtained when the FS value is set to approximately 1.2. This higher threshold allows the model to reproduce more realistic stress-strain responses, compensating for simplifications introduced by the finite element mesh and the constitutive formulation.

Density [tonne/mm^3]	$1.068 \cdot 10^{-9}$
Elastic Modulus [MPa]	1850
Poisson’s ratio	0.35
Yield Stress [MPa]	36
Plastic Failure Strain	1.2

Table 4.1: Values of Mechanical Parameters used in the LS-Dyna model for ABS

A summary table with the data of the material used in LS-Dyna for the ABS material is showed above. It should also be noted that all units used in the table of material properties are consistent with the LS-DYNA unit system adopted in this work. With this system, the forces are expressed in Newtons (N) and displacements in millimetres (mm), which is a convenient submultiple of the metre given the specimen dimensions. These unit conventions were applied consistently across all material models and simulations.

MAT 024 PIECEWISE LINEAR PLASTICITY: The MAT 024 PIECEWISE LINEAR PLASTICITY keyword was used to model the mechanical behaviour of Aluminium 6061-T6 in LS-DYNA. This material model represents an elasto-plastic response where the stress–strain relationship and strain rate dependency can be defined through a user-specified curve. The model allows for a realistic representation of the non-linear mechanical response of metals under various loading conditions. The load curve, in which effective stress is drawn against effective plastic strain, must be first defined with the DEFINE CURVE keyword and then linked to the material definition through the LCSS flag. The curve ensures that the simulation simulates the actual stress–strain response of the aluminium alloy under deformation. Another significant parameter in this material model is the FAIL flag, which is the plastic strain to failure. When the plastic strain in an element reaches this critical value, the element is deleted from the analysis, effectively simulating the material failure. This approach allows the model to reproduce the fracture behaviour observed in physical experiments.

All the input data for the MAT 024 model, including the LCSS curve and the FAIL value, were obtained from a the engineering website (Varmint Engineering Page) that provided material property coefficients and plastic failure strain values for 1,044 materials, including Aluminium 6061-T6. These coefficients are validated for use within LS-DYNA simulations and correspond to those described earlier in Chapter 3 of this work.

A specific explanation regarding the FAIL parameter is necessary. As mentioned above, it defines the effective plastic strain at failure. However, several studies have shown that to properly replicate the real mechanical behaviour of a material in a finite element simulation, the FAIL value often needs to be adjusted to a value significantly higher than the experimentally measured plastic strain at failure.

For example, in conventional tensile tests, the plastic strain to failure for Aluminium 6061-T6 typically ranges from 8% to 15%, while in LS-DYNA simulations, higher values are needed. This higher value compensates for the limitations of the element formulation and mesh discretization, providing a more accurate representation of the overall deformation and failure process observed experimentally.

Density [tonne/mm^3]	$2.713 \cdot 10^{-9}$
Elastic Modulus [MPa]	$6.895 \cdot 10^{4}$
Poisson's ratio	0.33
Yield Stress [MPa]	286.91
Plastic Failure Strain	0.8272

Table 4.2: Values of Mechanical Parameters used in the LS-Dyna model for Aluminium

MAT 081 MAT PLASTICITY WITH DAMAGE: The MAT 081 material model was employed to represent the mechanical behaviour of the titanium specimens. This constitutive model describes elasto-visco-plastic response and accounts explicitly for damage accumulation prior to rupture by using an effective plastic-strain measure. More specifically, two curves are required: effective stress (ES) versus effective plastic strain (EPS), and damage (DAM) versus EPS. The damage curve governs material softening after the onset of damage and allows a gradual degradation of stiffness instead of an abrupt loss of continuity. An effective plastic failure strain (EPFS) is defined and used as an erosion criterion. The damage curve is calibrated so that the first point corresponds to the EPFS (damage = 0) and subsequent points progressively increase the damage until complete failure (DAM = 1) Figure 4.6. Typical calibration of EPS is based on experimental uniaxial tensile tests.

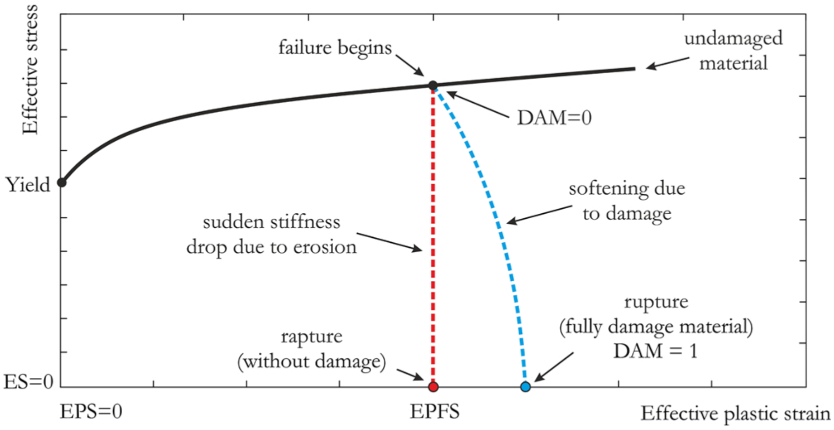

Figure 4.5: Damage Curve (blue line) used to model the Titanium Ti6Al4V [41]

In this work, damage and plasticity curves for the titanium produced by LENS were taken from the literature and implemented in the model. These curves were linked to the material through the appropriate flags (LCSS and LCDM). Moreover, the assumption was that the damage curve does not change the stiffness of the material.
Element erosion based on EPFS was enabled to reproduce fracture and material separation. Although in the reference, very large EPFS values (400%) were used, an EPFS of 100% was chosen in the present case. This value produced a realistic visual representation of fracture while avoiding excessively elongated elements that would reduce the stable time step and dramatically increase computational cost.

Density [tonne/mm^3]	$4.43 \cdot 10^{-9}$
Elastic Modulus [MPa]	$1.085 \cdot 10^{5}$
Poisson's ratio	0.3
Yield Stress [MPa]	710
Plastic Failure Strain	0.19

Table 4.3: Values of Mechanical Parameters used in the LS-Dyna model for Aluminium

NODE: As for the element keyword, its generated automatically from LS-Dyna once already meshed model is imported in the software. It represent the number of nodes of the mesh of the specimen.

PART: Once the material and the element model have been defined, they are assigned to the PART keyword, which is automatic. It is important to assign this characteristics to the model in order to obtain realistic simulations.

RIGIDWALL GEOMETRIC FLAT DISPLAY: In order to reproduce a realistic compression test setup, rigid walls were introduced in the model. The RIGIDWALL GEOMETRIC FLAT DISPLAY option was used to create the fixed plates of the testing cell. These walls were considered ideally rigid, meaning that their stiffness was set much higher than that of the specimen, so that no deformation occurred during loading. For each rigid wall, the direction of the normal vector (N) and the lateral vector (L) had to be defined. These two vectors describe the plane orientation with respect to the specimen and are necessary to correctly apply the boundary conditions. The wall size was also chosen slightly larger than the surface of the honeycomb cell in contact with it, to make sure that the load was applied uniformly on the whole specimen. The final dimensions of the rigid walls used for the simulations were: 40 × 40 mm for the 30 mm cubic cell, 28.2 × 28.2 mm for the titanium cell (18.2 mm edge), 31.5 × 31.5 mm for the aluminium one (21.5 mm edge). This configuration guaranteed full contact during loading, avoiding unrealistic stress concentration on the specimen edges.

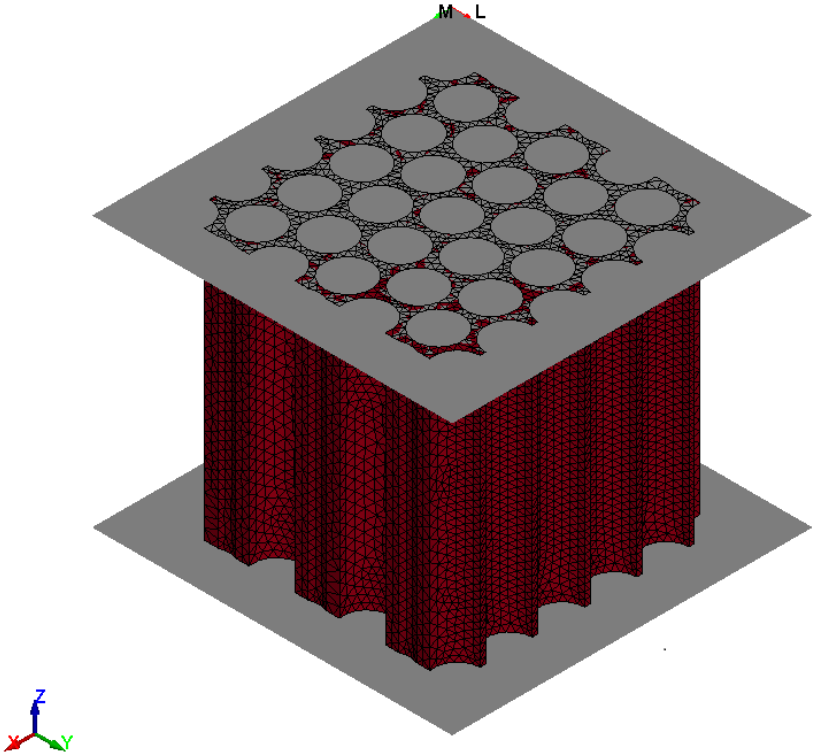

Figure 4.6: RigidWall representation in LS-Dyna

RIGIDWALL GEOMETRIC FLAT MOTION DISPLAY: The RIGIDWALL GE-

OMETRIC FLAT MOTION DISPLAY option was instead used to define the moving plates for the compression. These plates reproduce the loading head of the experimental machine. Depending on the type of test, the motion of the wall was constrained along a single direction , in particular, the Z-axis for vertical compression and the X-axis for horizontal compression while all other translations and rotations were restricted. The moving wall was defined with the same geometric parameters as the fixed one but positioned at a different height. The motion was controlled by a displacement-time curve, created using the DEFINE CURVE keyword and linked to the wall definition through the LCID flag. In order to properly apply the displacement, the OPT parameter of the keyword must assume the value 1, which tells the solver that the curve describes displacement and not velocity. Moreover, to make sure that the parameters were set in a right way, it good practice to check that the reaction forces on the upper and lower rigid walls are equal in magnitude (Figure 4.7). Finally, a small friction coefficient was introduced at the interface between the rigid wall and the specimen to better reproduce a common experimental conditions, as it is usually done in literature.

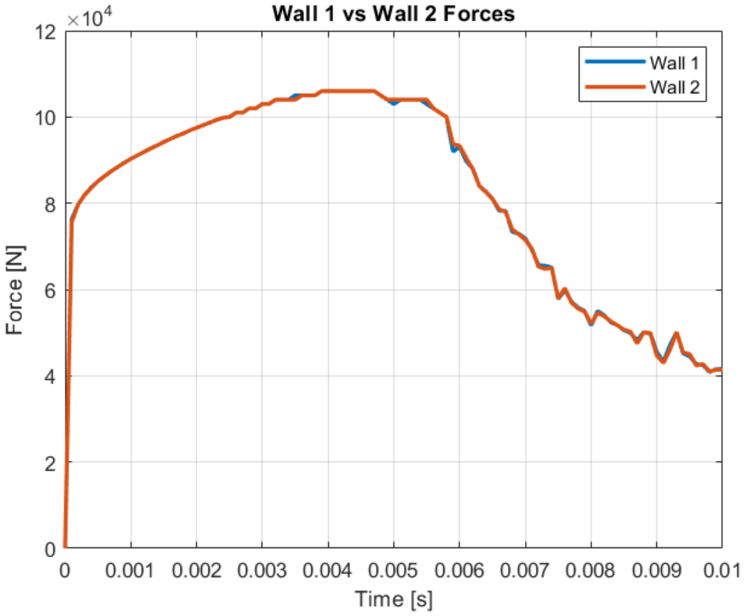

Figure 4.7: Wall 1 vs Wall 2 Forces

SECTION SOLID: it is a keyword related to the element formulation options. After defining the loads and boundary conditions, one of the most critical aspects that influence the accuracy of an explicit finite element analysis is the formulation of the solid elements used in the model. As it has been previously specified, since all the honeycomb structures were meshed with four-node tetrahedral elements, the SECTION SOLID keyword had to be properly defined to specify the element formulation adopted for the simulation. In LS-DYNA, different element formulations are available, and the choice can have a significant impact on the precision, convergence, and computational time of the analysis. It must be inserted in the ELFORM flag of the keyword.

Moreover, the choice of the element formulation, is crucial to avoid some numerical errors which may influence in a negative way the results of the simulation. The most common issues related to the element formulation are:

- **Hourglassing**: which occurs in first-order elements with reduced integration. These elements may deform in unrealistic ”hourglass” or ”zig-zag” shapes, without generating any internal strain energy. In this case, even if the geometry appears deformed, the solver calculates almost zero internal energy, producing incorrect results. This problem can be mitigated by using elements with a higher number of integration points.
- **Shear locking**: typical of first-order fully integrated elements subjected to bending. It causes an artificial increase in stiffness due to a non-zero shear strain inside the element, leading to an overestimation of the model rigidity. Using higher-order elements can solve this issue.
- **Volumetric locking**: which can appear for materials that can almost be considered incompressible. It generates unrealistic stresses and excessive stiffness. To reduce this effect, LS-DYNA allows the use of hexahedral or tetrahedral elements with selective reduced integration.

Considering these factors, the EQ.13 formulation (one-point nodal pressure tetrahedron) was selected. This option was selected as it provides a good balance between accuracy and computational time. According to LS-DYNA documentation and several studies in the literature, the EQ.13 element produces results comparable to more complex formulations, such as EQ.4, but with a much lower computational cost. Moreover, this formulation performs particularly well for metallic materials with a Poisson’s ratio greater than zero (such as aluminium and titanium) and helps reduce volumetric locking phenomena.

SET NODE LIST: The SET NODE LIST keyword was introduced specifically for the tensile test simulations, where two opposite faces of the cubic specimen were used to apply and to constrain motion. This command allows to create two groups of nodes from the existing mesh, that can later be referenced by other keywords. In particular, the first set of nodes, representing the fixed surface, had all degrees of freedom constrained, while the second set representing the loaded surface, the displacement along one direction was imposed to simulate the tensile loading. Finally, the constraining and movement applications are applied with the key words BOUNDARY PRESCRIBED MOTION SET, BOUNDARY SPC SET.

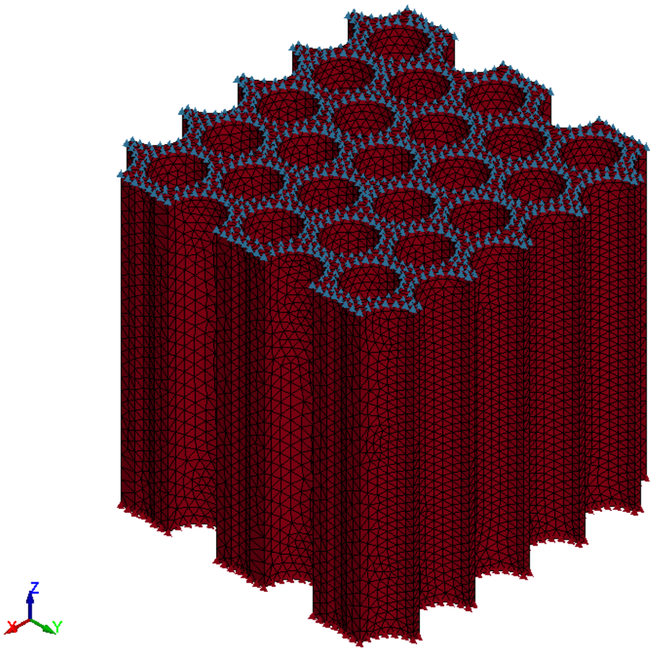

Figure 4.8: Set of nodes used in the Model. To the blue nodes the motion is applied, while the red nodes are the static nodes

BOUNDARY PRESCRIBED MOTION SET: The BOUNDARY PRESCRIBED MOTION SET keyword was used to apply a prescribed motion to the node set defined for the moving side of the specimen. This command allows assigning a motion to a selected group of nodes, and it is fundamental for reproducing the tensile test in a realistic way. As for the RIGIDWALLS, the motion law was defined through a displacement-time curve, created using the DEFINE CURVE keyword, and then linked to the BOUNDARY PRESCRIBED MOTION SET using the flag LCID. The most relevant parameters in this keyword are DOF and VAD: where DOF specifies the degrees of freedom allowed for the prescribed motion. For vertical tension, it was set to 3, which enables displacement only along the Z-axis, while for horizontal tension, it was set to 1, allowing movement only along the X-axis. The VAD flag, instead, determines the type of variable represented by the curve. Setting "VAD = 2" tells the solver that the curve describes displacement versus time, while the default setting would interpret it as velocity.

BOUNDARY SPC SET: The BOUNDARY SPC SET is the keyword that allows to fully constrain the transversal motion and rotation of the set of nodes to which is applied. This is then applied to the nodes that must be fixed in the tension test. In this case, all translational and rotational movements along the three global directions (X, Y, Z) were restricted by setting each flag to 1. This created a fully constrained boundary condition.

4.2.2 Mesh Generation and Mesh Convergence Study

The generation and definition of the mesh is a key procedure for any finite element analysis. The quality of the mesh as well as the selection of the size of elements determines directly both the accuracy of the results and the computational time. For example, a very coarse mesh can produce unrealistic results, while an excessively fine mesh would lead to an extremely high calculation time. For these reasons, this step must be accomplished carefully in order to achieve a proper balance between results accuracy and computational time.
The mesh can be generated directly in LS-DYNA or using dedicated meshing software. In this work, Altair HyperMesh was chosen for mesh generation. After the 3D geometry was created in AutoCAD 2026, as previously described, it was exported in "*.iges*" format, which can be directly imported into HyperMesh.

Once the model is imported, the mesh definition process can begin. In the main command panel of HyperMesh, under the "3D" section, the command "Tet → Create" is selected. This opens a pop-up window where the user can define the parameters for generating the tetrahedral mesh. In this window, the average element size is specified, and the options "Use proximity" and "Curvature-based refinement" were activated to obtain a finer and higher-quality mesh, especially in the critical regions of the model.

More specifically, the curvature-based refinement automatically minimizes the size of elements in regions of large curvature, so that the geometry is captured in a proper way and to allow the physical effects to be accurately simulated. Similarly, "use proximity" refine the mesh in areas where two parts or surfaces are close to each other. This is done because there should always be a reasonable number of elements within the area of local thickness to avoid numerical errors. Moreover, this choice provides a good transition from small to large elements, providing a better quality of the mesh. Finally, if necessary, an element size may also be prescribed as a minimum in the same dialog box.

Once the mesh has been generated, it is usually recommended to perform a mesh check quality. For elements such as 3D tetrahedral elements, one of the most suitable criteria is the "Tet Collapse" parameter, which measure how close an element is to being flat or degenerate. A rating of 1.0 shows a perfect element, whereas for a fully collapsed element, the rating is 0.0. Elements with Tet Collapse $<$ 0.1–0.15 tend to be poor and might cause convergence problems or incorrect simulation results.

In Figure 4.9, as an example, is reported the model that is used for the Titanium cubic cell for the tension and compression simulation between specimens having the same mass. As it can be noticed, it shows an high quality mesh where all the elements have Tet Collapse values well above 0.15, confirming that the chosen parameters ensured a reliable and accurate mesh configuration.

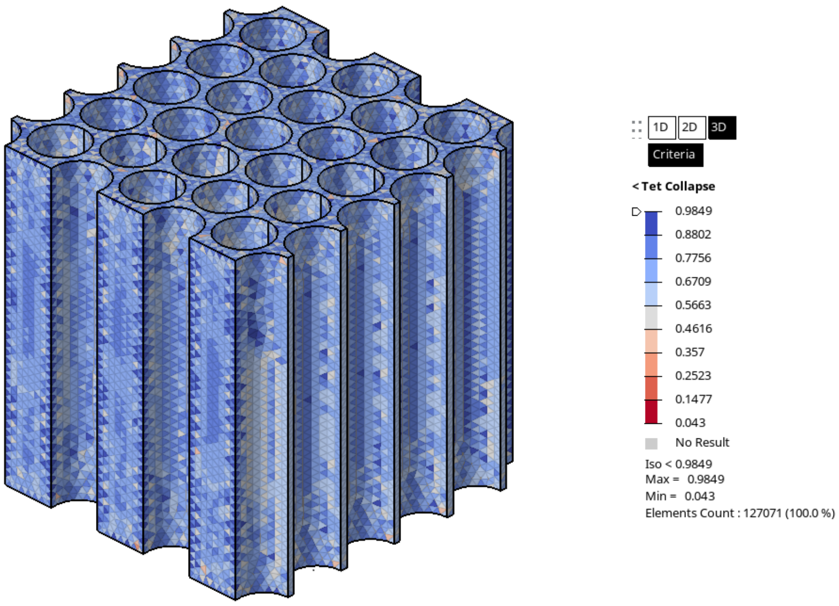

Figure 4.9: Tet-Collapse Values for Mesh Quality

The same procedure was applied to all the other CAD models used in this work, and in each case, a high-quality mesh was obtained.

In order to ensure the accuracy of the results, not only the mesh quality but also the number of elements and nodes plays a key role. A general rule is that a finer mesh provides results closer to the real behavior of the system, at the expense of higher computational cost and longer simulation times.
For this reason, a mesh convergence study was performed for each CAD model. Different mesh sizes were tested to identify the optimal element size that represents the best compromise between accuracy and computational efficiency. The convergence criterion was applied by verifying that further mesh refinement produced negligible variations in the results. Once this condition was met, the mesh was considered convergent, and the solution mesh-independent.

As shown in Figure 4.10, as an example, the Force vs. Time curve for the horizontal compression of the aluminum specimen (with equal-mass configuration) was obtained using three different mesh sizes:

1. 0.85 mm - 92855 elements and 29574 nodes
2. 0.785 mm - 121740 elements and 37514 nodes
3. 0.77 mm 127394 elements and 39222 nodes

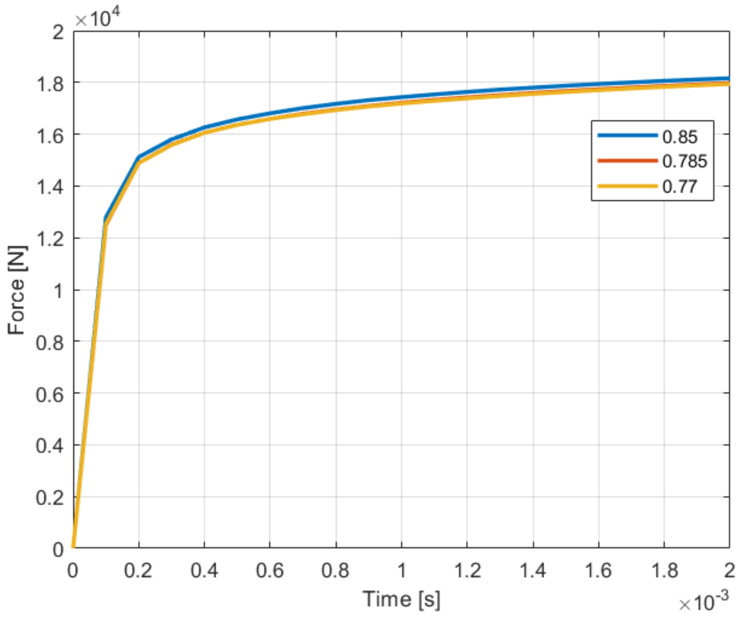

Figure 4.10: Different Mesh Element Dimension Results Comparison

The three meshes produced very similar results. Since the variation between the curves was minimal and the computational cost increased significantly for the finer meshes, the mesh size of 0.85 mm was selected for the aluminum model.

The same convergence procedure was repeated for the other CAD geometries analyzed in this study. In particular, for the CAD used in the simulation where the same CAD was used, chaing the material, the most suitable mesh dimesion resulted in being 1.2 mm with 95375 elements and 30773 nodes, while for the titanium model used in the equal-mass compression and tension tests, the most suitable average element size was 0.66 mm, corresponding to 127072 elements and 39380 nodes.

4.3 Post-Processing

In this section the post processing and the evaluation and analysis of the FEA analysis results is carried out. As it was previously anticipated, two main simulation strategies are adopted:

1. Tests on a single CAD specimen and varying the material (1st family of specimens)
2. Test on three CAD specimens with equal mass varying the material (2nd family of specimens)

For the first case, the same CAD specimen, is tested both in tension and compression. The material assigned to the CAD is systematically changed between Titanium, Aluminium and ABS, in order to identify performance differences between materials, under same conditions.

For the second case instead, three different 3D CAD specimens having the same mass, but made of different materials were tested, again in tension and compression. In this case, three different CAD models are needed, as the specimen dimensions will change according to the density of each material to ensure identical mass.
Furthermore, both tensile and compressive tests were conducted in two loading directions: vertically, along the axis of the holes, and perpendicularly to it. This approach was necessary because a structure like the one considered in this work, featuring through-holes arranged in a hexagonal honeycomb pattern, even if made of an isotropic solid material, exhibits an intrinsically orthotropic mechanical behaviour at the macroscopic scale, as its properties strongly depend on the loading direction.

The two directions considered are the following:

- Out-of-Plane Direction: it is the direction of the extrusion axis, to which the cell walls are aligned. It represents the vertical loading direction in the tests. In this orientation, the structure is significantly stiffer and stronger, as the cell walls mainly experience axial tensile or compressive stresses.
- In-Plane Directions: This correspond to loading within the plane of the honeycomb cells, representing the lateral tests. In this direction, the dominant deformation mechanism is the bending of the cell walls, resulting in considerably lower stiffness and strength compared to the Out-of-Plane direction.

In both directions, tensile and compressive tests were performed as previously explained. In particular, for the In-Plane case, the tests were carried out along the x-axis, as along this direction the cells present a larger surface area in contact to the rigid wall. This orientation would also be the preferred configuration if panels were to be attached to form a sandwich structure, commonly used in energy absorption applications. By contrast, the loading along the y-axis would involve a much smaller area and would therefore be practically less suitable.
In this post-processing stage, several parameters were analysed and compared among all specimens, for both tensile and compressive load cases, and across the two simulation strategies. A particular attention was given on the stress-strain response, the elastic stiffness, and the overall deformation behaviour of the specimens. These quantities were evaluated to assess how the material properties and specimen geometry influence the global mechanical performance under the same boundary conditions.

All the numerical results were accessed through the LS-DYNA PrePost interface. After loading the simulation output files, it allows an analysis of the results allowing to visualize, process, and export all data related to the simulation such as, for example, nodal displacements, stress distribution, reaction forces, and energy evolution. The application of the post-processing procedure ensures a systematic and accurate comparison

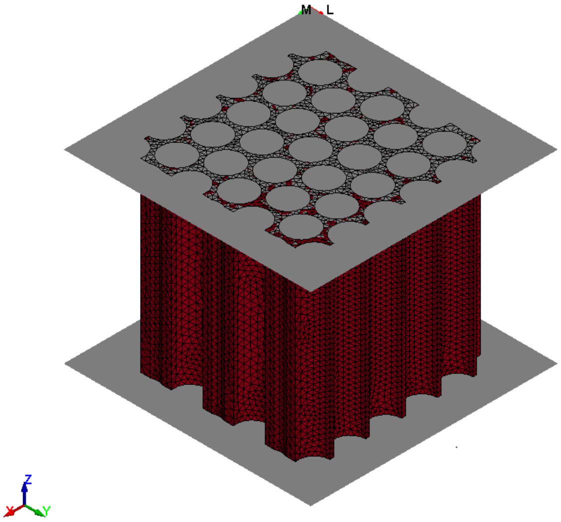

Figure 4.11: Vertical Compression

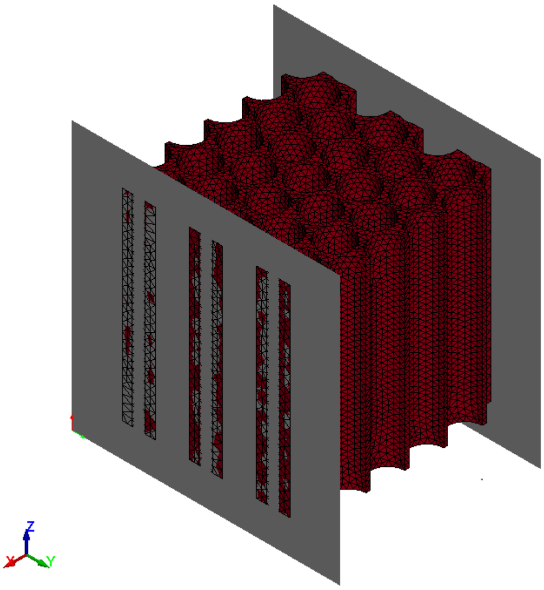

Figure 4.12: Horizontal Compression

of the numerical results for all specimens and loading conditions.

Stress-Strain Curve
As mentioned, one of the data that are discussed is the stress-strain curve. In order to evaluate the stress-strain curves, the data required are the total compressive or tensile force acting on the specimen and the corresponding displacement. The total compressive force is obtained as the resultant reaction on the loading surface (RIGIDWALL) for the compression tests, while it is calculated as the reaction force on the set of nodes located on one face of the cube for tension.

The displacement represents the effective deformation (both for compression and tension) applied to the specimen. Since both compression and tension were performed by imposing a prescribed displacement to the specimen, the value of displacement L directly corresponds to the imposed loading curve.

Having the force and displacement data, it is possible to derive the equivalent nominal stress and strain. In order to properly evaluate this curve, the stress was calculated as the total reaction force divided by the nominal cross-sectional area of the specimen, which includes both solid and void regions. By employing this nominal area, the calculated equivalent stresses represent the effective load-bearing capacity of the entire architecture, rather than the local stress within the cell walls. This is the standard approach in the characterization of cellular solids, lattice structures, and honeycomb cores, where the aim is to determine properties that can be directly applied to macro-scale continuum models. This approach allows defining equivalent properties such as the equivalent stiffness for the cellular material at the macroscopic scale.

- **Nominal Stress:**The nominal stress is defined as the ratio between the total reaction force (F) and the nominal or equivalent cross-sectional area (A_0) of the specimen, where A_0 represents the total geometric area perpendicular to the loading direction, including the voids.
- **Nominal Strain:**The nominal strain is defined as the ratio between the applied displacement (δL) and the initial specimen length (L_0)along the loading direction.

$$\sigma = \frac{F}{A_0} \tag{4.2}$$

$$\varepsilon = \frac{\delta L}{L_0} \tag{4.3}$$

In particular, referring to the two families of test described in Chapter 3.1, for the first families of test, since the specimen used is the same for all materials involved, the Area is given by 30x30mm = 900 mm^2, and L0 is equal to 30mm.

While for the second family:

- For the aluminium the area is 462.25 mm^2 (21.5x21.5) and L0 = 21.5 mm
- For titanium the area is 331.24 mm^2 (18.2x18.2)while L0 = 18.2 mm

Equivalent Elastic Stiffness

The equivalent stiffness of each specimen was determined as the ratio between the applied load and the corresponding displacement, which corresponds to the slope of the force-displacement curve in the elastic region.

In particular:

$$K = \frac{F}{\Delta L} \tag{4.4}$$

where:

- K is the structural stiffness (typically expressed in N/mm),
- F is the total reaction force or the applied load (N),
- ΔL is the resulting displacement or shortening (mm).

4.3.1 Compression Tests

The present analysis of the simulations conducted with the software LS-Dyna, begins with compression tests, which represent the most common experimental approach used to assess the equivalent mechanical behaviour of cellular structures. A first evaluation was carried out on both families of simulations, in order to compare their response under the same loading conditions. A corresponding discussion for tensile tests will be presented later in this chapter.

Vertical Compression

In the figures below are reported the stress-strain curves obtained from quasi-static vertical uniaxial compression for specimens made of Titanium Ti6al4v (Figure 4.13) Aluminium 6061 -T6 (Figure 4.14) , and ABS (Figure 4.15) , all sharing the same geometry, together with the figures showing their fractural mechanisms, respectively (Figure 4.16),(Figure 4.17),(Figure 4.18).
For ease of comparison, compressive stresses and strains are plotted in the positive quadrant as absolute values.

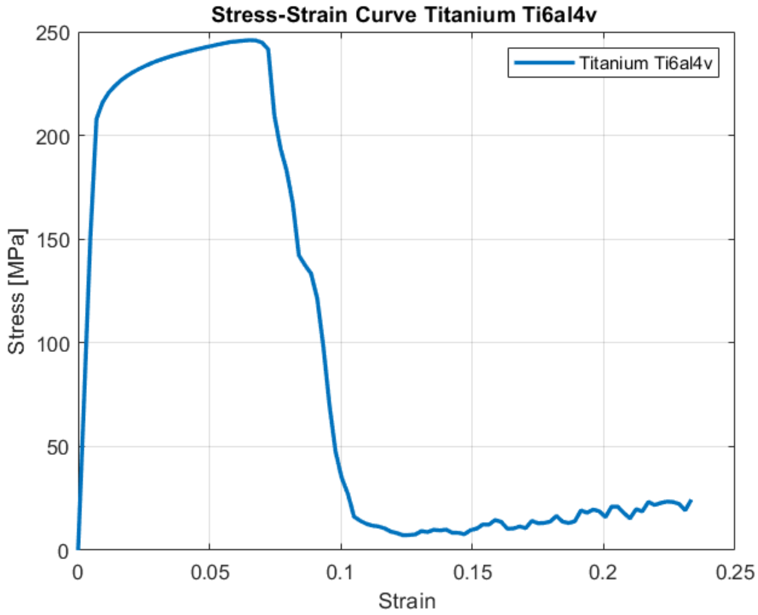

Figure 4.13: Stress-Strain Curve of the Specimen made with Titanium Ti6al4v

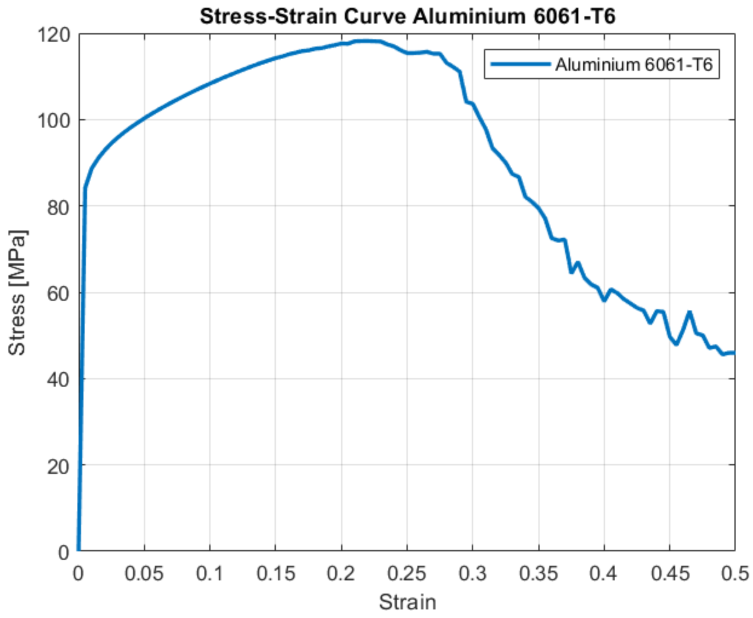

Figure 4.14: Stress-Strain Curve of the Specimen made with Aluminium 6061 - T6

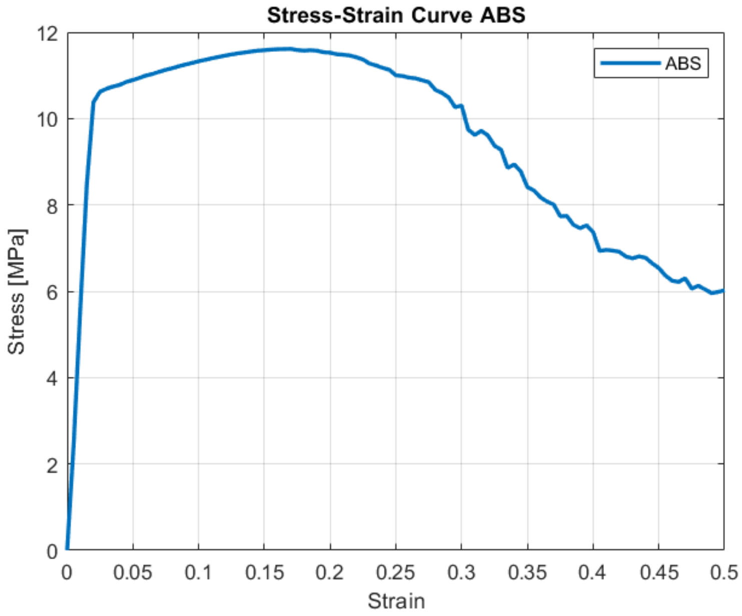

Figure 4.15: Stress-Strain Curve of the Specimen made with ABS

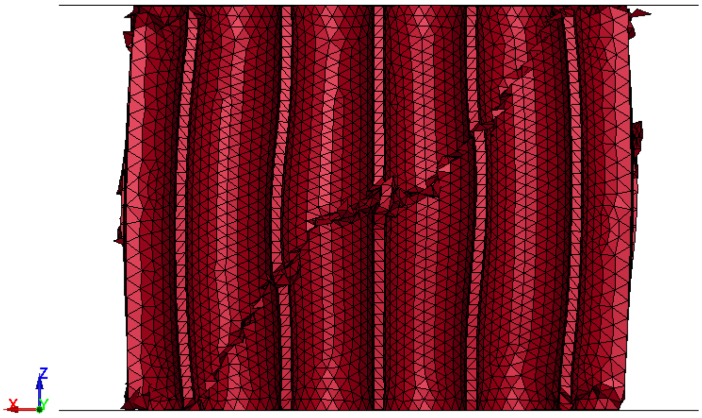

Figure 4.16: Fracture Mode of the Titanium Ti6Al4V Specimen under Vertical Compression

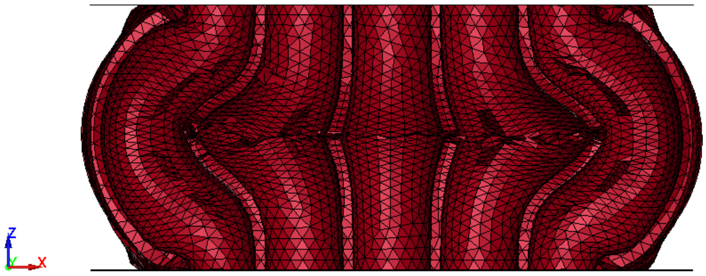

Figure 4.17: Fracture Mode of the Aluminium 6061 - T6 Specimen under Vertical Compression (section of the specimen)

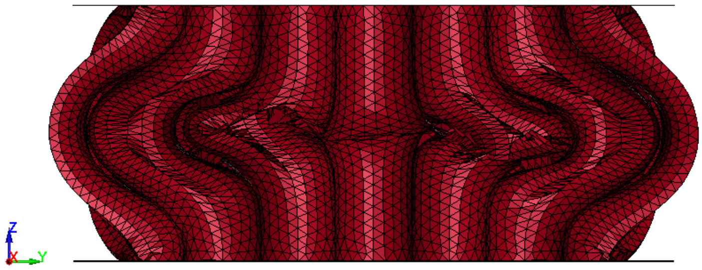

Figure 4.18: Fracture Mode of the ABS Specimen under Vertical Compression (section of the specimen)

As it is possible to notice, the three curves present a clearly distinct mechanical responses among the materials, presenting different curves with different shapes and different deformations. Although all of them show an initial linear-elastic region followed by yielding and

plastic deformation, their post-yield behaviour differs significantly. Titanium exhibits a sudden strength drop after reaching its maximum compressive strength, Aluminium shows gradual strain hardening, and ABS displays a soft, highly ductile response.
Common to all cases, however, is an initial linear trend where stress increases proportionally with strain, indicating elastic behaviour.

Titanium Ti6al4v

The stress-strain curve obtained for the titanium specimen is typical of a high-strength material. The slope of the elastic region is very high, reaching up to about 208 MPa of yield stress, and a corresponding very high stiffness of about 918,720 N/mm. The curve reaches its maximum stress of about 246 MPa at very low level of strain (0.065). After reaching this peak, a sudden stress drop can be observed, with the stress rapidly decreasing to values around 10-20 MPa at a strain of about 10%. This behaviour clearly indicates an abrupt structural failure or instability under compression, which occurs once the maximum load-bearing capacity is exceeded. This behaviour is visually confirmed in (Figure 4.16), which highlights a distinct diagonal fracture line running from top to bottom through the specimen, indicating the catastrophic failure plane. Notably, a slight plastic deformation along the vertical axis is observed just before to the final, abrupt fracture.

Aluminium 6061-T6

The aluminium curve shows the typical behaviour of a ductile metal with strain hardening under compression. The initial slope is steep, indicating a high stiffness, which is evaluated of about 504,666.7 N/mm, which is lower than that of titanium. The yield point occurs at approximately 84 MPa, followed by a transition to the plastic region where the slope gradually decreases. In particular, after yielding, the stress continues to rise slowly with increasing strain, showing the effect of strain hardening, and reaches a maximum value of around 120 MPa at about 22% strain.
Differently from titanium, the aluminium 6061-T6 doesn't suddenly collapse, but the stress gradually decreases, until the end of the test. This behaviour indicates that aluminium deforms plastically without a sudden or catastrophic collapse, which is consistent with a more ductile nature of the material.
This is confirmed from the specimen showed in Figure 4.17, which illustrates that the primary fracture is exclusively internal and not visible on the exterior surface. This indicates that the failure mechanism begins inside the structure, while the outer part primarily exhibits a high level of plastic deformation consistent with the applied compressive load.

ABS - Acrylonitrile Butadiene Styrene

The ABS stress-strain curve represents the typical response of a ductile thermoplastic polymer with high deformability. As expected, since ABS is the weakest material among the three, the initial slope of the curve is the lowest, corresponding to a stiffness of about

16066.7 N/mm. The yield point occurs at approximately 10.5 MPa and 0.02 strain, while the maximum stress of 11.6 MPa is reached at a higher strain level (almost 20%) The difference between the yield and peak stress values is relatively small. After the peak, there is a gradual softening phase in which the stress slowly decreases from about 11.5 MPa to 6 MPa at a strain of 0.5. This is more gradual and smoother compared to aluminium and is typical of polymeric behaviour, where the material can experience plastic deformation at large strains without cracking. The cross-sectional view of the compressed specimen (Figure 4.18) reveals that cracks begin to appear within the internal holes only after the structure has undergone a substantial amount of vertical deformation. In particular, these internal cracks do not propagate to the external surface, where only a significant degree of outward deformation (barrelling) is evident.

An overall comparison of the properties obtained in the uniaxial vertical compression test are reported in the table below.

Material	Maximum Stress [MPa]	Yield Stress [MPa]	Stiffness [N/mm]
Titanium Ti6Al4V	246	208	918,720
Aluminium 6061-T6	120	84	504,666.7
ABS	11.6	10.5	16,066.7

Table 4.4: Mechanical properties obtained from Vertical Uniaxial Compression

Horizontal Compression

The following figures show the quasi-static uniaxial compression along the X-axis stress-strain curves for Titanium (Figure 4.19), Aluminium (Figure 4.20), and ABS (Figure 4.21) coupled with the images showing the specimens after rupture. Similar to the vertical compression tests, for each material there is a specific mechanical behaviour, but here overall stiffness and strength are significantly lower. This is an indication of the anisotropic characteristic of these cellular structures. In particular, as it can be imagined, under load along the transversal direction, the cell walls are loaded perpendicularly with respect to the principal axis of the holes, so that they buckle or bend instead of axially compressing, until reaching rupture. Since thin-wall bending strength is inherently lower than their axial compressive strength, failure occurs earlier, usually due to buckling or local instability instead of material failure.

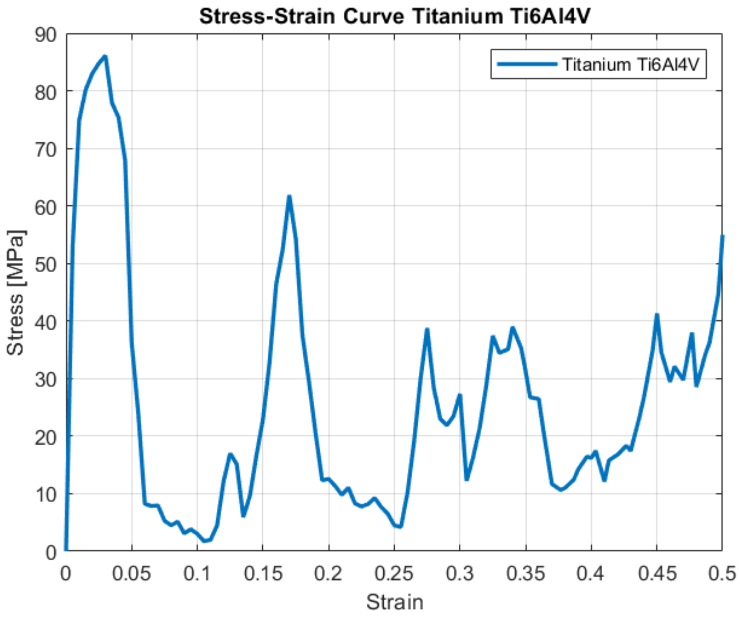

Figure 4.19: Stress-Strain Curve (a) and fracture mode (b) of the Specimen made with Titanium Ti6Al4V

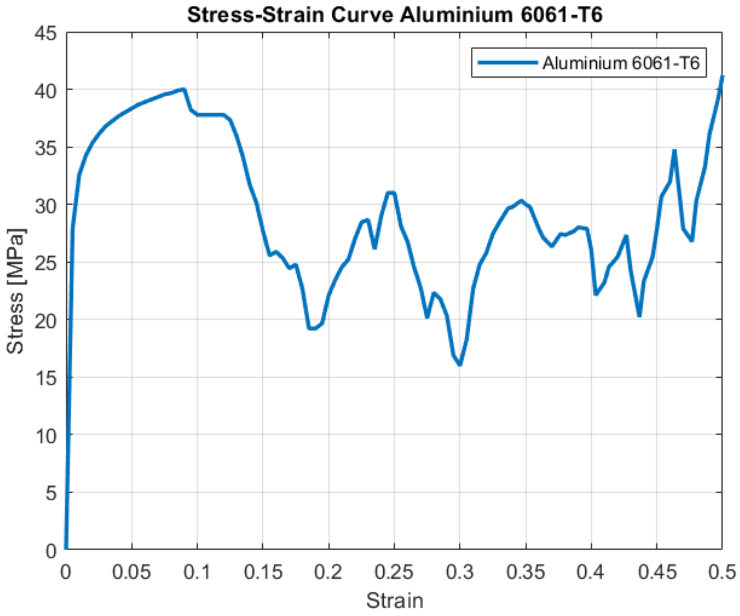

Figure 4.20: Stress-Strain Curve of the Specimen made with Aluminium 6061-T6

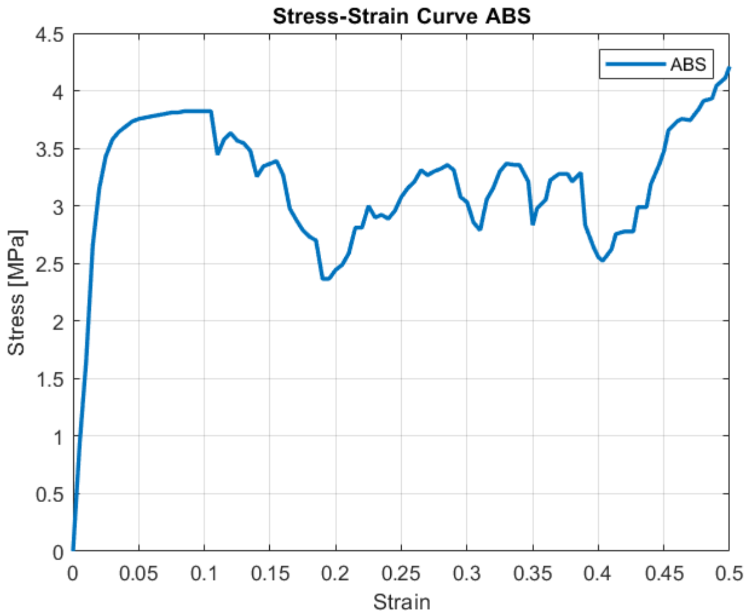

Figure 4.21: Stress-Strain Curve of the Specimen made with ABS

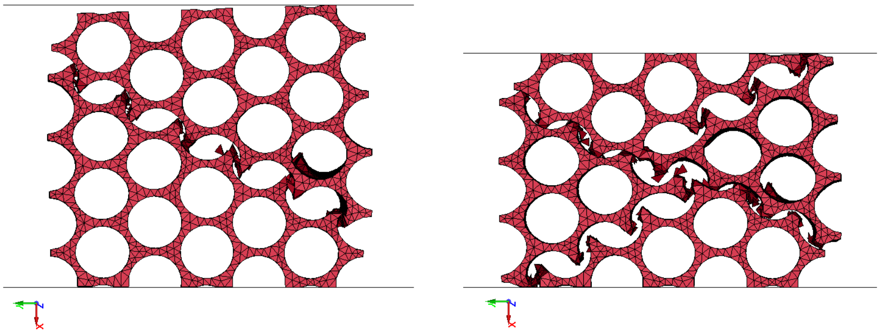

Figure 4.22: Fracture Mode of the Titanium Ti6Al4V Specimen under Horizontal Compression

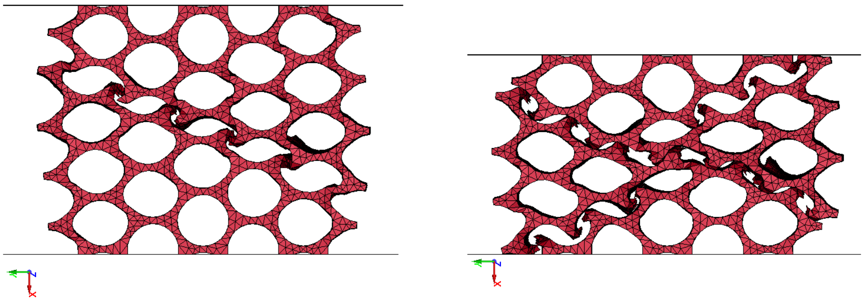

Figure 4.23: Fracture Mode of the Aluminium 6061-T6 Specimen under Horizontal Compression

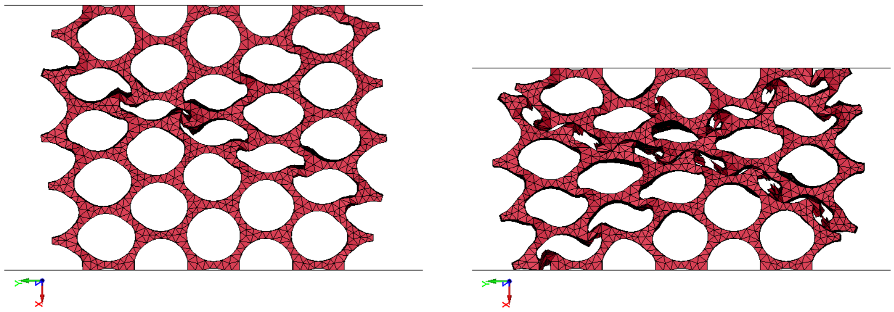

Figure 4.24: Fracture Mode of the ABS Specimen under Horizontal Compression

Titanium Ti6Al4V

As can be noticed, the titanium horizontal compression stress-strain curve is different from the vertical one and also result less stable. As in the previous case, the elastic region is present, but less steep, presenting a lower stiffness of about 224,666.7 N/mm. The yield point is less clear compared to the vertical behaviour, but can be estimated at around 75 MPa at 0.01 strain, and the ultimate stress is at around 86 MPa at 0.03 strain, resulting in less than half of the 246 MPa, that was instead observed during vertical compression. As it happened for the vertical uniaxial compression, after the peak, the stress, again, abruptly falls, however, in this case , it presents some oscillations and fluctuations in an interval between 4 and 60 MPa at larger strains. These oscillations are typical of a progressive and unstable failure, where broken components come into contacts between each others under the loading process, temporarly increasing the resistance before further failure occurs. This progressive failure mechanism, evident in Figure 4.22 illustrating the titanium specimen's rupture chain , involves broken components making contact under the ongoing loading process. The fracture initiates along a primary diagonal line, followed by a second break in the opposite diagonal direction, ultimately creating a characteristic X-shaped rupture path, which is highly indicative of a predominant shear failure mechanism under horizontal compression. This component contact temporarily increases the overall structural resistance before subsequent failure stages occurs. The little deformations of the holes of the specimen before reaching rupture, confirms the classification of the LENS-produced Titanium as exhibiting quasi-brittle behavior.

Aluminium 6061-T6

The stress-strain curve of the horizontally compressed aluminium maintains a ductile behaviour as for the vertical case but with significantly lower stiffness and strength. The initial elastic region is less steep, which corresponds to a stiffness of around 97,666.7 N/mm. The yield point is at around 32 MPa at 0.01 strain, and the peak stress is at around 40 MPa at 0.1 strain, which is much lower in comparison to the previous value of around 120 MPa in vertical compression. As for Titanium, after the peak, the stress decreases progressively, with a more gradual trend compared to titanium. This gradual reduction, along with the appearance of small stress oscillations, is typical of the ductility of aluminium and also of the local instability typical of this loading direction. The oscillations are indicative of progressive local buckling or partial collapse of cell walls, leading to temporary load redistribution. Despite this, the material maintains a moderate load-carrying capacity even at high strain levels, consistent with its plastic and ductile nature. As observed in (Figure 4.23), the sequence of deformation and fracture stages in the aluminium specimen largely mirrors that of the titanium specimen, retaining the distinct X-shaped fracture path. However, a key difference emerges in the degree of hole deformation. For identical failure conditions, the aluminium specimen's holes are noticeably more deformed than those in titanium. This observation clearly highlights and confirms the more ductile behaviour of Aluminium compared to LENS-produced titanium, indicating its capacity to withstand greater plastic deformation before final structural failure.

ABS

The stress strain curve of the horizontal compression of ABS demonstrates the response of a general ductile thermoplastic polymer. Similar to the vertical compression, the initial slope is confirmed to be the least among the three, consistently with the observed low structural stiffness found along the vertical direction. The stiffness during this test is 4824 N/mm. The yielding occurs at a strain of approximately 0.03, or a stress of approximately 3.6 MPa, and the peak stress of 3.8 MPa occurs at a strain of 0.105. This peak is far below 11.6 MPa under vertical compressive loading.

Also with ABS, the trend so far encountered in aluminum and titanium is confirmed. In particular, after the peak stress, there occurs a gradual softening followed by oscillations and fluctuations; however, in this case with lower amplitude. Even though stress gradually reduces, for the ABS, it is relatively steady, between the range of 2.3 to 3.6 MPa at large strains. This confirms ABS's ability to resist large plastic deformations in the x-direction despite reduced strength and deformation stability. This behaviour can be seen in the extensive deformation of the specimen showed in (Figure 4.24), where again, the failure

path once again confirms the X-pattern of the fracture.
More specifically, the ABS specimen exhibits the highest deformation magnitude before reaching its actual rupture point compared to both metallic cases, a feature clearly visible in the image, where, the shape of the internal holes is severely deformed. Similar to aluminium but even more pronounced, the walls of the ABS cell structure resist failure until a very high local strain is achieved. These characteristics make ABS suitable for applications in energy absorption.

Material	Maximum Stress [MPa]	Yield Stress [MPa]	Stiffness [N/mm]
Titanium Ti6Al4V	86	75	224,666.7
Aluminium 6061-T6	40 MPa	32 MPa	97,666.7
ABS	3.8	3.6	4824

Table 4.5: Values of parameters obtained from Horizontal Uniaxial Compression

Vertical vs Horizontal Compression

Comparing horizontal (X-axis) and vertical (Z-axis) compression results for titanium, aluminum, and ABS clearly demonstrates the anisotropic behavior of the specimens, attributable to their internal cellular structure, as illustrated in the LS-DYNA model. This anisotropy represents the fundamental difference between the two loading directions.

More specifically, horizontal compression is the most weakened direction. In this case, the compressive strength is significantly lower compared to the vertical direction due to instability effects such as buckling. In particular, when a compressive load is applied along the horizontal direction, the walls of the cells are laterally compressed, and this induces geometric instability (lateral bending) before reaching the yield of the bulk material. This buckling action significantly reduces the maximum load that the structure can support.

This is reflected in the maximum stress and yield values in horizontal compression, which are considerably lower than those in the vertical direction. Furthermore, the post-peak phase exhibits pronounced stress fluctuations, indicative of progressive structural failure caused by cell wall buckling. Buckling is not a singular failure event but a progressive and instable process that reduces load-bearing uniformity and leads to a rapid drop in equivalent structural strength after the initial peak.

In all cases, horizontal stiffness is significantly lower than vertical stiffness. The reduction is most pronounced for metals (aluminum and titanium, decreasing by approximately 80% and 75%, respectively) and less pronounced for ABS (around 70%). Maximum stress is also significantly lower in horizontal compression for all materials. Additionally, the post-yield phase in horizontal compression is more unstable, showing stress fluctuations, especially for titanium and aluminum, due to progressive specimen failure.

For an easier comparison, the values of the mechanical characteristics obtained both from the Vertical and Horizontal compression tests are here reported:

Material	Maximum Stress [MPa]	Yield Stress [MPa]	Stiffness [N/mm]
Titanium Ti6Al4V	246	208	918,720
Aluminium 6061-T6	120	84	504,666.7
ABS	11.6	10.5	16,066.7

Table 4.6: Values of parameters obtained from Vertical Uniaxial Compression

Material	Maximum Stress [MPa]	Yield Stress [MPa]	Stiffness [N/mm]
Titanium Ti6Al4V	86	75	224,666.7
Aluminium 6061-T6	40	32	97,666.7
ABS	3.8	3.6	4824

Table 4.7: Values of parameters obtained from Horizontal Uniaxial Compression

4.3.2 Compression of Specimens with the same mass

This section describes uniaxial compression simulations on bio-inspired cellular specimens of equal mass (8 g, isomass condition) but made from different materials. The ABS specimen was used as a reference for setting the target mass, and will therefore maintain its original dimensions. Titanium and aluminum specimens instead, were modified to match this mass.

This approach allows evaluation of the materials' specific structural efficiency, isolating the influence of material density on overall performance. In aerospace, automotive, and biomedical applications, the primary objective is often not absolute strength but strength-to-weight ratio (specific strength). By maintaining constant mass, this test directly compares the ability of titanium, aluminum, and ABS to provide maximum mechanical performance (stress and stiffness) within the same weight constraint and specimen design. Through this analysis is possible to identify which material, given a fixed mass and geometry, offers the highest equivalent structural stiffness and maximum load capacity.

The stress-strain curves for ABS remain consistent with previous tests, therefore will not be reported here.

Vertical Compression

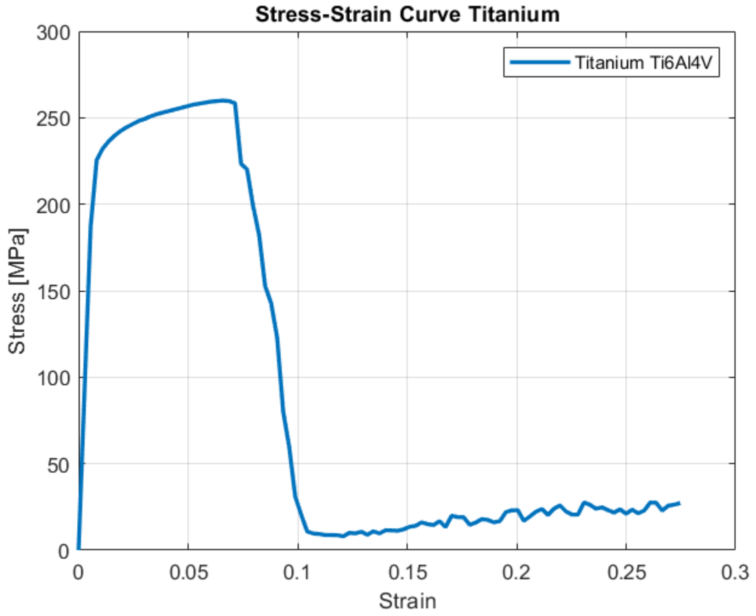

Figure 4.25: Stress-Strain Curve of the Specimen made with Titanium Ti6Al4V

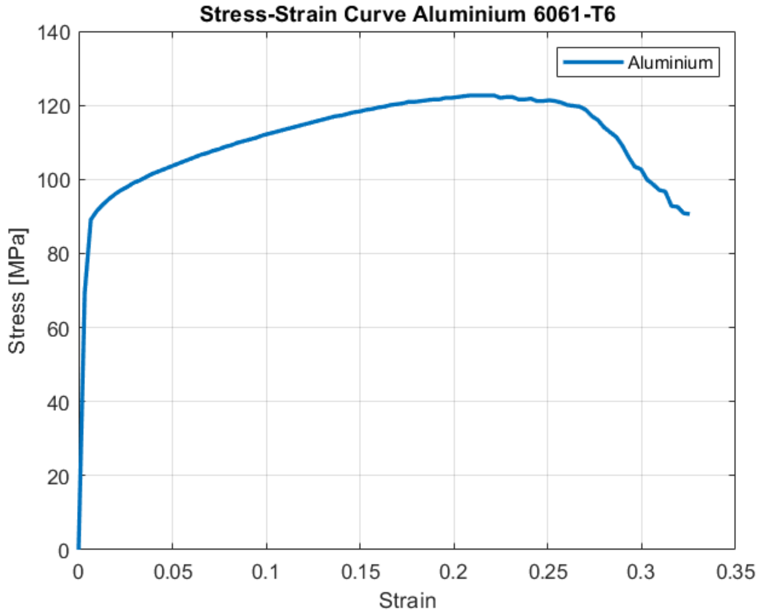

Figure 4.26: Stress-Strain Curve of the Specimen made with Aluminium 6061-T6

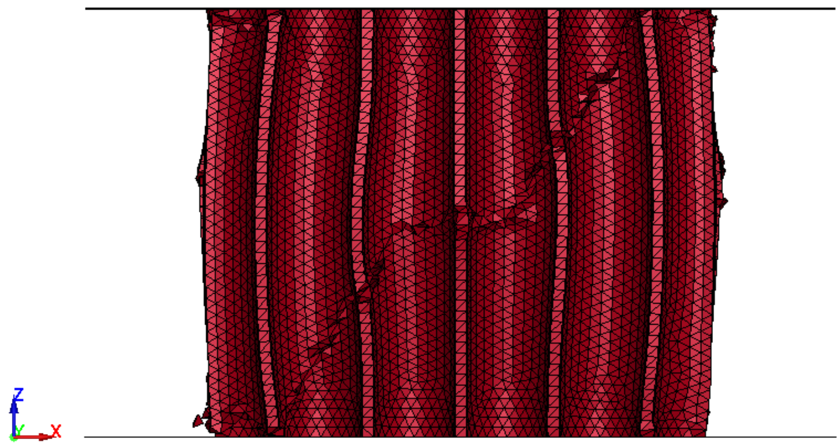

Figure 4.27: Fracture Mode of the Titanium Ti6Al4V Specimen under Vertical Compression

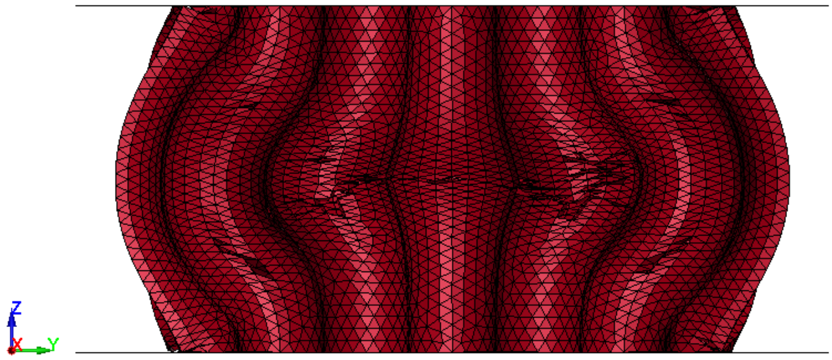

Figure 4.28: Fracture Mode of the Aluminium 6061-T6 Specimen under Vertical Compression

Horizontal Compression

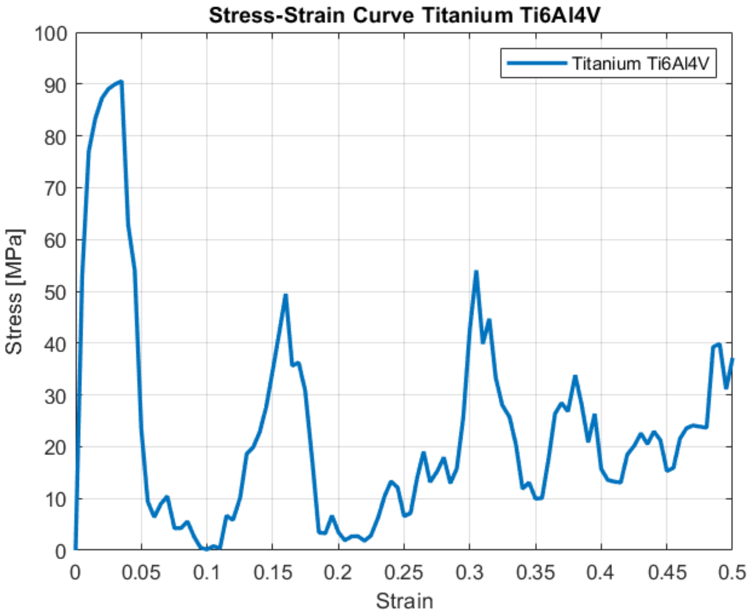

Figure 4.29: Stress-Strain Curve of the Specimen made with Titanium Ti6Al4V

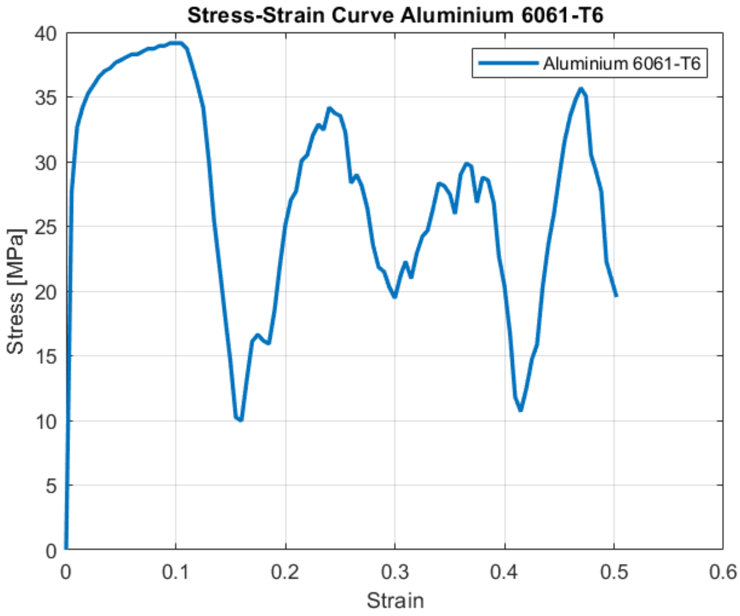

Figure 4.30: Stress-Strain Curve of the Specimen made with Aluminium 6061-T6

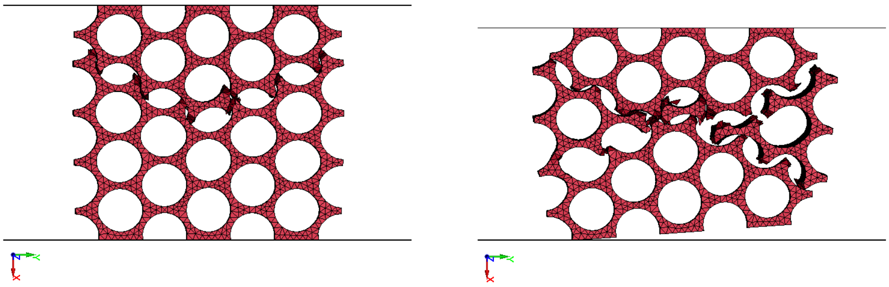

Figure 4.31: Fracture Mode of the Titanium Ti6Al4V Specimen under Horizontal Compression

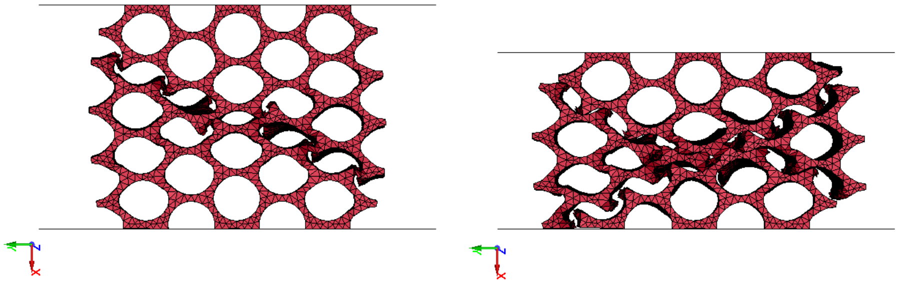

Figure 4.32: Fracture Mode of the Aluminium 6061-T6 Specimen under Horizontal Compression

As it can be noted from the figures above, representing stress-strain curves and the fractural mechanisms, both the qualitative shape of the stress-strain curves and the failure path, remains consistent across both directions for all the tested materials, reflecting the invariant constitutive behavior of the materials and the failure kinematics of the cellular structure. As discussed in Chapter 3, specimen dimensions were scaled, which allowed to preserve porosity and wall thickness ratios, ensuring that macroscopic deformation modes are inherently maintained.

Titanium Ti6Al4V

For both compression directions, it maintains a steep elastic phase with a maximum stress succeeded by a rapid and sudden collapse, which is typical of structural failure during compression. In horizontal compression, this is followed by unstable oscillations. More specifically, in the vertical compression test, titanium present a maximum compression stress of 260 MPa at a strain of 6.6% which is even greater than the value obtained for the compression of the first family of specimens. The same phenomena can be seen for the horizontal compression, where, once again the new specimen reaches a larger value of strength (90.5 MPa). This may be due to the fact that, usually, when the entire structure is scaled down proportionally, and the absolute dimensions of the walls and cells are reduced, smaller structural elements usually tend to exhibit higher local stiffness and

stability, and consequently a higher critical buckling strength.
The proportional scaling for mass equivalence largely maintains the inherent deformation modes in the titanium specimen, though there are subtle differences in the failure progression. For vertical compression the failure is characterized by a diagonal fracture line running from top to bottom, which indicates the catastrophic failure plane, together with a small lateral deformation perpendicular to the loading direction. Similarly, in horizontal compression, the failure still produces the final X-shaped fracture path associated with shear collapse. However, the way this final pattern is reached is different from the larger specimen. The fracture here does not immediately follow the diagonal; instead, the rupture initiates with a V-shaped fracture as the first step, immediately followed by a mirrored V-fracture. The reason for this localized change in the initial failure path, can be attributed to the size effect and the impact of the micro-architecture's stability in the smaller specimen. When the component's absolute dimensions are reduced, the influence of local stress concentrations at the cell walls and nodes increases relative to the overall geometry. This change in scale likely shifts the point of least resistance, causing the local instability (buckling) to produce the V-shaped path before converging into the overall X-shaped shear collapse dictated by the bulk structural load.

Aluminium 6061-T6

For the aluminium, the ductile behavior is confirmed with a clear yielding followed by a strain hardening phase, where the stress continues to rise gradually, allowing for large plastic deformations before reaching rupture. As for Titanium, Aluminium also presents an oscillating phase for high strains in the case of horizontal compression, which instead does not occur in vertical compression, confirming the difference in behavior noted so far. Moreover, as with Titanium, an increase in maximum strength is noted for the new Aluminium specimen compared to the previous one, particularly regarding vertical compression, (presenting a maximum strength of 123 MPa) while for horizontal compression, this behavior is less evident for Aluminium. This behavior can again be traced back to what was said for Titanium.
The overall ductile deformation modes are maintained in the scaled aluminum specimen for both loading directions. Under vertical compression, the primary deformation is characterized by a significant increase in the specimen's lateral dimensions (barrelling), while the internal cracks are primarily concentrated within the porous structure and internal holes; the external surfaces remain uncracked, indicating that failure mechanisms are confined to the cellular core. For horizontal compression, the failure maintains the characteristic final X-shaped fracture path associated with shear collapse. The superior ductile behavior of aluminum compared to the LENS-produced titanium is confirmed, not only visible in the stress-strain curve but also in the deformation image (Figure 4.32), where the internal holes are noticeably more deformed and elongated compared to the titanium counterpart. This structural evidence clearly demonstrates aluminum's sustained capacity for plastic deformation and energy absorption in a bending-dominated failure mode.

ABS

The thermoplastic polymer maintains the previously recorded values. Therefore, it still presents the lowest specific stiffness and yielding values, followed by a gradual softening, confirming its capacity for high-deformation energy absorption.

The fact that the curves maintain their fundamental characteristics, demonstrates that the nature of the mechanical failure is intrinsically linked to the bulk material properties and the cellular architecture, and is not altered by the proportional reduction in dimensions. Regarding instead, the stiffness values, this parameter shows the most important differences in this case.

In particular, the absolute stiffness values are significantly lower compared to the case of equal-sized specimens. Specifically, for vertical compression, the following values are observed :

Material	Maximum Stress [MPa]	Yield Stress [MPa]	Stiffness [N/mm]
Titanium Ti6Al4V	260	225.5	510,000
Aluminium 6061-T6	123	89	294,285.7

Table 4.8: New values of parameters obtained from Vertical Uniaxial Compression

For horizontal compression:

Material	Maximum Stress [MPa]	Yield Stress [MPa]	Stiffness [N/mm]
Titanium Ti6Al4V	90.5	77	140,109.9
Aluminium 6061-T6	39	32.6	70,307.8

Table 4.9: New values of parameters obtained from Horizontal Uniaxial Compression

The difference between the X and Z directions remains consistent with was already previously observed: the structure is stronger and stiffer along the cell axis (Z), while wall bending prevails in the transverse direction (X). The decrease in stiffness can be explained in the following way. It does not come from a variation in the intrinsic properties of the material, but it is a consequence of the macroscopic reduction of the dimension of the specimen in order to have isomassic specimens. More specifically, the structural stiffness is in general proportional to the ratio A0/L0, and having the specimen reduced in both A0 and L0, this would explain the stiffness reduction.

A further observation concerns the ratio between the two compressions stiffnesses. For Titanium, the ratio remained almost perfectly constant (around 3.64 for the compression of specimens with same mass against 3.67 in the case of the first family of specimen). Aluminium, however, presents a more marked reduction in the ratio, passing from (4.09) for the first family of specimens to (3.54) the second. This difference from ideal scalability means that the reduction of dimensions would have had a proportionally greater impact on the vertical stiffness than on the horizontal stiffness of the Aluminium sample, where the main operation mechanism is the bending of the cellular walls.

Overall, the mechanical trend remain consistent, however the absolute performance decreases because of the reduction of the specimen size.

The reduction of holes and walls makes the structure globally "softer," with lower stiffness values, while maintaining the relative ratio between directions and materials unaltered. In terms of Specific Efficiency, the results suggest that Titanium, despite having undergone the largest dimensional variation, continues to guarantee the best performance, followed by Aluminium and finally ABS, confirming the behavior observed in the first series of tests.

Finally, as so far noted, the bio-inspired honeycomb structure present an orthotropic behavior, with significantly higher stiffness and strength along the vertical (Out-of-Plane) direction, compared to the horizontal directions (In-Plane). This anisotropy is conserved even in the reduced specimens, confirming that it is a geometric and not a dimensional property.

This result validates the use of high-strength, moderate-density alloys like Titanium for the design of lightweight, high-performance cellular structures, where dimensional optimization compensates for the volume cost, while ABS confirms its utility for energy absorption applications.

4.3.3 Tension Test

Following the completion of the compression tests on the specimens, the same methodology is applied for the uniaxial tension test. The test will again be conducted along the vertical (Z) and horizontal (X) directions for both families of specimens.
This analysis extends the evaluation of the mechanical behaviour of the bio-inspired honeycomb cellular structure, moving from the previously described compression tests (vertical and horizontal) to uniaxial tension tests, executed in the same loading directions.
The objective is threefore to describe the stress-strain response and failure behaviour of the Titanium, Aluminium, and ABS specimens, to quantify the equivalent structural stiffnesses, and, finally, to conduct a qualitative comparison between the tension and compression regimes, highlighting the asymmetries and anisotropy induced by the structural geometry.

In general, is expected to obtain stress-strain curves that represent different behaviours, with varying maximum stress and strain values. However, regarding the elastic stiffness (or equivalent structural stiffness), it is generally anticipated that the value in the elastic region will be very similar between the compression and tension cases.

First Family of Specimens - Same Dimension Specimens

Vertical Tension

The results obtained in the vertical (Z) direction show stiffnesses that reflect the expected order based on the elastic moduli of the bulk materials (Titanium > Aluminium > ABS), although the values are lower than the massive material due to the structure's porosity.

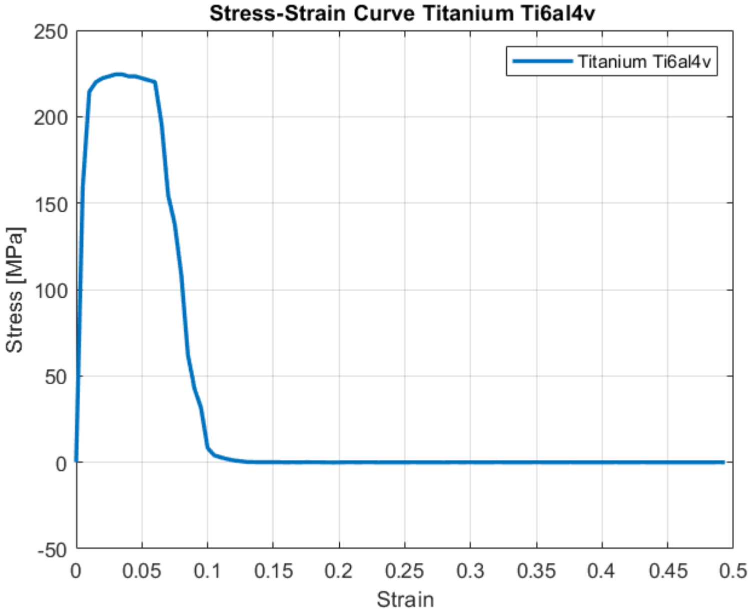

Figure 4.33: Stress-Strain Curve of the Specimen made with Titanium Ti6Al4V

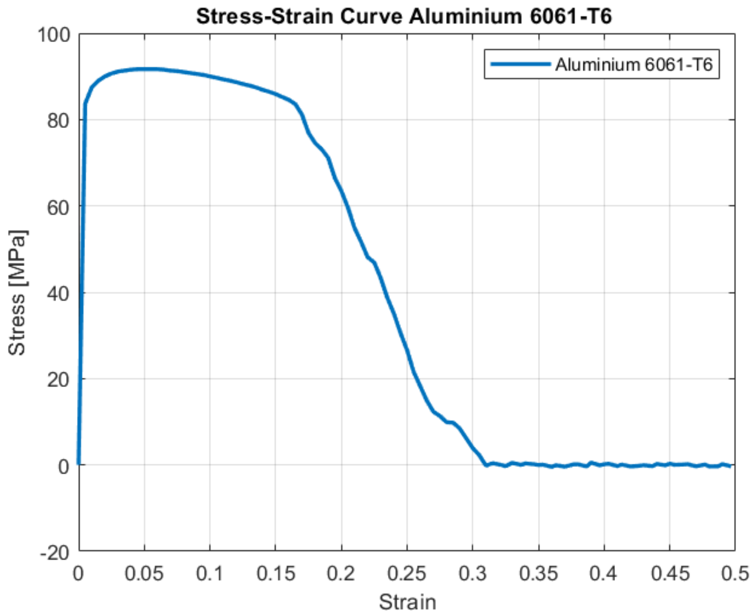

Figure 4.34: Stress-Strain Curve of the Specimen made with Aluminium 6061 - T6

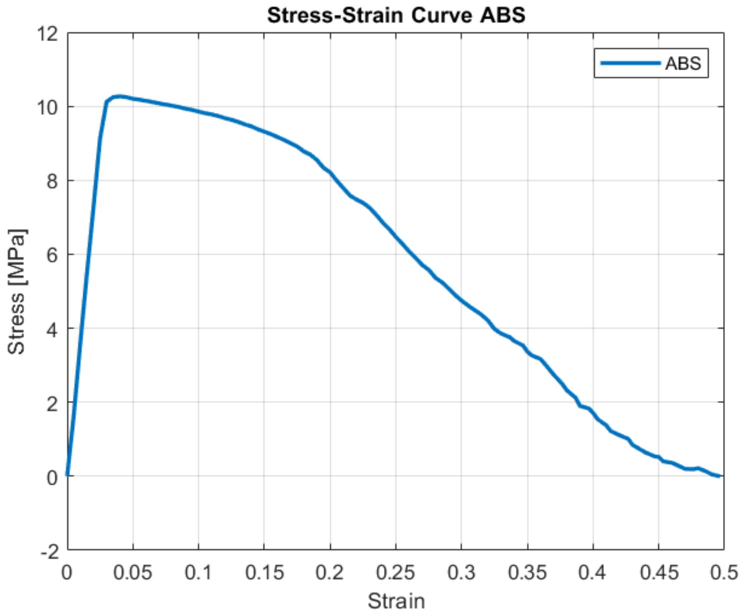

Figure 4.35: Stress-Strain Curve of the Specimen made with ABS

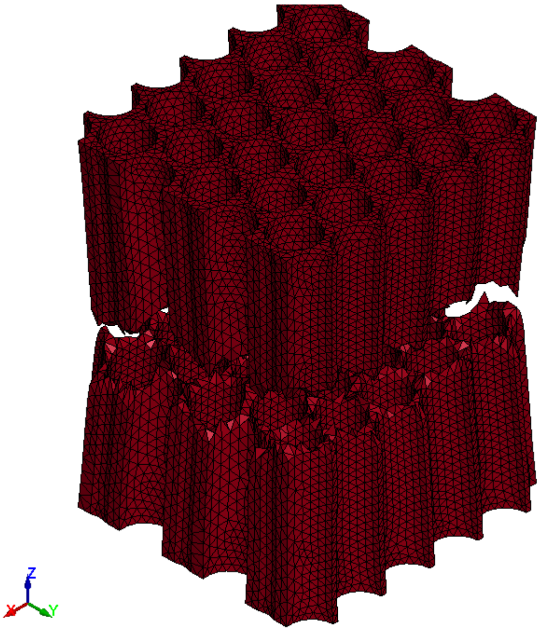

Figure 4.36: Fracture Mode of the Titanium Ti6Al4V Specimen under Vertical Tension

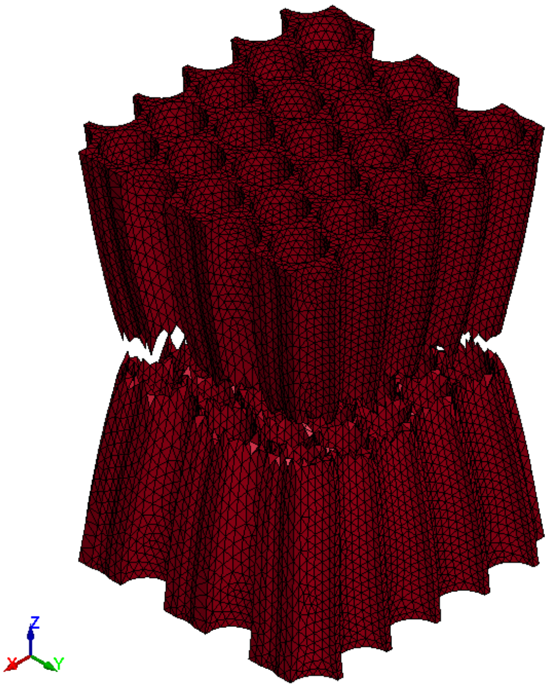

Figure 4.37: Fracture Mode of the Aluminium 6061-T6 Specimen under Vertical Tension

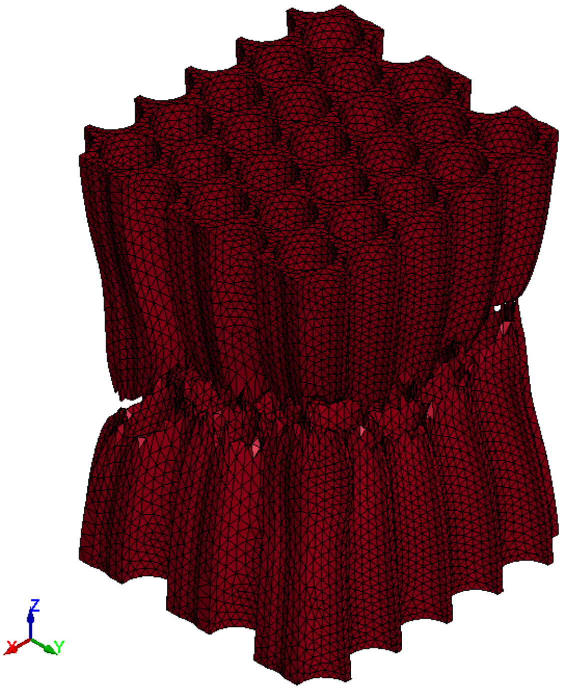

Figure 4.38: Fracture Mode of the ABS Specimen under Vertical Tension

Titanium Ti6Al4V

Titanium is characterized by the maximum elastic stiffness ($K_Z = 953,330$ N/mm). This value is very similar although a bit higher compared to the elastic stiffness of the same test but executed in the compression case (918,720 N/mm). The stress-strain curve of this test exhibits a very steep, linear elastic phase, typical of a high-strength material.

Differently from vertical compression, where the peak stress was 246 MPa, the tension curve reaches a maximum stress of 224.4 MPa, which is lower than the compression peak. Subsequently to the linear region, the curve is characterised by a flat region, where the stress remains nearly constant for about 5% strain. It is then followed by failure due to net-section semi-brittle fracture of the cell walls. This results in a rapid stress drop-off and a low fracture strain value of 6%. This behaviour is consistent with the semi-brittle nature of LENS-produced Titanium under axial load, whereas the same compression test showed a fracture strain of approximately 7.2%.
The characteristic sudden stress drop is visually confirmed to be due to a catastrophic net-section fracture that completely divides the specimen in two, as shown in (Figure 4.36). With this rupture, a small plastic elongation of the specimen is observed as a small reduction or necking of the cross-section. This necking corresponds to the plateau region of the stress-strain curve, confirming that the material undergo a work-hardening phase before failure. This mechanism is opposed to the lateral expansion observed during vertical compression. The high stiffness and small plastic region are consistent with the semi-brittle nature of LENS-produced Titanium under axial load.

Aluminium 6061-T6

For the Aluminium material, the curve shows a high stiffness of about $K_Z = 502,000$ N/mm. Once again, as in the case of Titanium, the stiffness value is very similar and essentially identical to the stiffness obtained in the respective compression test (504,666.7 N/mm). The overall behaviour is typical of a ductile metal in tension. More specifically, it is observed a linear elastic phase, followed by clear yielding beginning at 0.5% strain and 83.7 MPa stress. This is then followed by a work-hardening phase, reaching the UTS (Ultimate Tensile Strength) at 91.7 MPa with 5% strain. Finally, fracture, due to necking and subsequent failure, starts at approximately $16-17\%$ strain. In this case, except for the stiffness values, the difference between tension and compression tests is evident. The tension test exhibits notably lower maximum UTS and respective strain values, in particular, in compression, the values are 120 MPa, reached at about 22% strain, making them 23.6% and 77% higher, respectively, compared to tension.
Figure 4.37 showing the catastrophic fracture clearly demonstrates the bisection of the specimen into two distinct parts. The failure mechanism qualitatively mirrors that of titanium, being a net-section fracture. The cross-sectional reduction (necking) caused by plastic deformation preceding the rupture is visibly more pronounced in the aluminium specimen compared to the titanium one, confirming the material's higher capacity for ductile plastic deformation under axial tension. This difference in failure mechanism accounts for the substantially lower maximum Ultimate Tensile Strength (UTS) and strain values compared to the vertical compression test.

ABS

The ABS polymer, as expected, shows the lowest structural stiffness ($K_Z = 10,851$ N/mm), typical of a thermoplastic material. However, in this case, the stiffness difference between tension and compression is more pronounced in this material. The values obtained are 16,066.7 N/mm for compression and 10,851 N/mm for tension, leading to a difference of about 32%. This is likely due to the combination of the asymmetric behaviour of the base material (ABS) and structural instability phenomena which only manifest in compression. The stress-strain curve in tension (Z-direction), as anticipated shows low yielding (10.12 MPa at 3% strain), which essentially corresponds to the maximum stress, which is estimated at 10.26 MPa at 4% strain, followed by a long phase of softening (plastic flow). Both yielding and UTS are similar to the values obtained in the compression test (yielding of 10.5 MPa and maximum stress of 11.6 MPa). What changes significantly is the strain at which these occur: the maximum strain for compression was 20%.
The ABS polymer, as expected from the tensile test, also exhibits a final fracture that divides the specimen into two parts, characterized by the highest reduction cross-section among the three materials. Due to the material's viscoelastic nature, the necking (cross-section reduction) is the most significant of the three specimens, visually confirming its thermoplastic ductility under tensile load. Notably, the fracture plane is not uniform; it initiates diagonally, starting lower on the left corner and terminating higher on the right corner. This non-uniform fracture initiation may be attributed to a geometric imperfec-

tion or localized stress concentration, causing failure to start at the weakest point before rapidly propagating across the structure.

Material	Maximum Stress [MPa]	Yield Stress [MPa]	Stiffness [N/mm]
Titanium Ti6Al4V	224.4	159	953,330
Aluminium 6061-T6	91.7	83.7	502,000
ABS	10.26	10.12	10,851

Table 4.10: Values of parameters obtained from Vertical Uniaxial Tension

Analysis and Comparison (Vertical Tension)

From the results of the vertical tension test, several key evaluations can be drawn.
For both high-strength metallic materials, Titanium Ti6Al4V and Aluminium 6061-T6, the maximum structural stress (σ_{max}) achieved in the vertical (Out-of-Plane) tension test was lower than the peak stress recorded during vertical compression. This difference is a direct consequence of the divergent failure mechanisms induced by the axial loading direction and that were previously explained.

The honeycomb structure, when loaded along the Z-axis, is a stretch-dominated architecture.

- For Aluminium, the compression peak of 120 MPa exceeded the tension peak of 91.7 MPa by 30.8%.
- For Titanium, the compression peak of 246 MPa was 9.6% higher than the tension peak of 224.4 MPa.

Thus, the ability of the structure to densify under compression intrinsically provides a higher ultimate structural load limit compared to the limit imposed by net-section brittle fracture in tension.

In particular, under compression, the load is applied along the Z-axis, causing the cylindrical cell walls to act as long, slender columns subjected to axial compression. The failure initiation is governed by geometric instability, initiated by local micro-buckling of the struts. However, given the relative robustness of the walls, they prevent the rapid, layer-by-layer collapse typical of traditional thin-walled honeycombs, and the failure mode is dominated by a broader overall structural instability (global buckling or barrelling) of the cylindrical assembly, characterized by a long-wavelength deformation along the specimen's height.
The maximum compressive stress (246 MPa for Titanium and 120 MPa for Aluminium) represent the total load required to overcome initial instability and fully crush the structure into the densified state. This stabilizing deformation mechanism offers a higher ultimate structural load limit than failure based solely on the net-section material strength.

Moreover, in compression, instead, the material is usually able to sustain greater stresses because micro-cracks tend to close rather than propagate, delaying catastrophic failure.

Differently, under tension, stabilizing mechanisms are absent, failure is governed by the tensile strength capacity of the reduced solid area (net section). Once the localized stress, which is often concentrated at corners, fillets, or minor defects, exceeds the ultimate tensile strength (UTS) of the bulk material, the failing mechanism starts, leading to a catastrophic fracture.

These mechanisms also explain the large difference between the fracture strain in tension and compression for the ABS specimen, where under compression, the structure achieves impressive strain capacity, maintaining a stable load-bearing capacity up to about 20% strain before densification. In contrast, the tension test demonstrated catastrophic failure at a low strain of only 4%. This profound difference, even if not properly replicable in the present FEM analysis, can be explained in a practical way, by the interaction of the failure mode with the microscopic manufacturing defects introduced during the Fused Deposition Modeling (FDM) process.
3D printing often leaves gaps between layers, voids, and imperfect fusion points in complex nodal regions. Under tensile load, these microscopic imperfections act as intense stress concentrators. The structure's failure is dictated by the weakest link, leading to early crack initiation and rapid propagation through the net section, limiting the structure's ability to exploit the polymer's bulk ductility at the macroscopic level. The result is structural failure at low strain.
Under compressive load, however, the failure mechanism is different, and relies on extensive plastic bending and large deformation of the struts. Compressive forces tend to close the microscopic voids and inter-layer gaps associated with FDM, rather than propagating cracks from them. This protective mechanism allows the polymer to successfully transition into the characteristic stress plateau region of cellular materials, facilitating substantial plastic flow and high-strain energy absorption (up to 20% strain).

Elastic Stiffness Comparison (K)

An important evaluation concerns the comparison of stiffness between the tension and compression tests. In particular, in the linear elastic regime, the structural stiffness (K) is determined in general as the slope of the force-displacement curve. For isotropic and linear-elastic materials, the initial structure stiffness should ideally be the same whether the structure is subjected to tension or compression loading.

Specifically, what can be seen is that for the Aluminium 6061-T6 sample, the compressive stiffness ($\mathrm{K_{comp}} = 504,666.7$ N/mm) and the tensile stiffness ($\mathrm{K_{tens}} = 502,000$ N/mm) are very similar with a deviation of 0.53%.
This proximity confirms that the elastic behaviour of the metallic cellular structure is primarily controlled by the geometry and bulk modulus, exhibiting near-perfect symmetry in the initial elastic loading phase.

For the Titanium Ti6Al4V, the stiffness also demonstrates high symmetry, with $\mathrm{K}_{\mathrm{tens}} = 953,330$ N/mm being only 3.7% higher than $\mathrm{K}_{\mathrm{comp}} = 918,720$ N/mm. This minor deviation may be attributed to slight non-linear effects near the high yield point of the titanium alloy or microstructural variations inherent in the additive manufacturing process.

In contrast to the metals, the ABS polymer exhibits a pronounced structural stiffness asymmetry, with $K_{\mathrm{comp}} = 16,066.7$ N/mm being 48.1% higher than $K_{\mathrm{tens}} = 10,851$ N/mm. This substantial difference is characteristic of engineering polymers, which often show intrinsic Tensile-Compressive Asymmetry (TCA) and viscoelastic effects, where molecular behaviour differs significantly under opposite loads, leading to a measurable increase in effective stiffness in compression even within the nominal elastic region.

Horizontal Tension

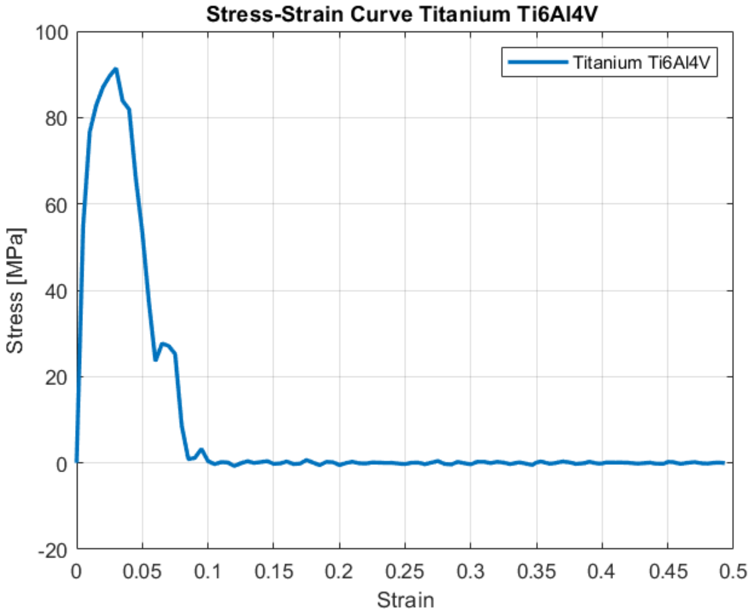

Figure 4.39: Stress-Strain Curve of the Specimen made with Titanium Ti6Al4V

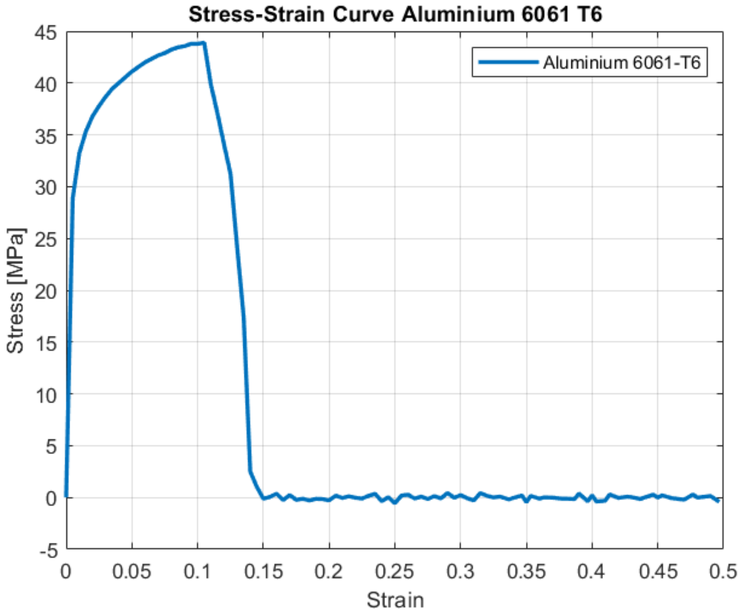

Figure 4.40: Stress-Strain Curve of the Specimen made with Aluminium 6061-T6

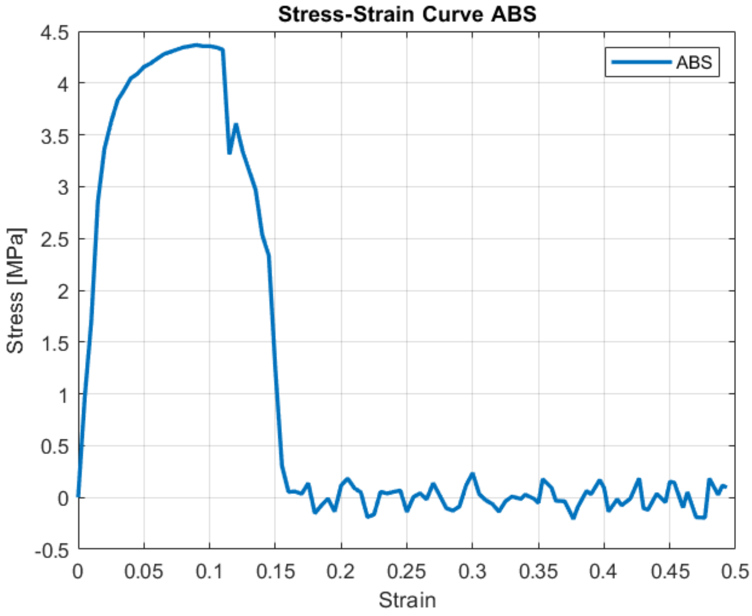

Figure 4.41: Stress-Strain Curve of the Specimen made with ABS

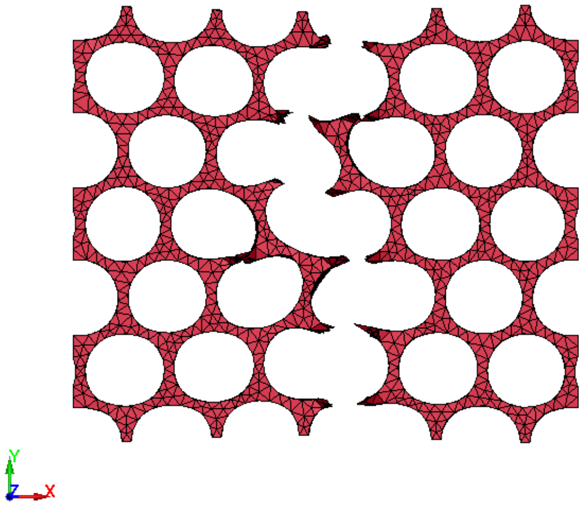

Figure 4.42: Fracture Mode of the Titanium Ti6Al4V Specimen under Horizontal Tension

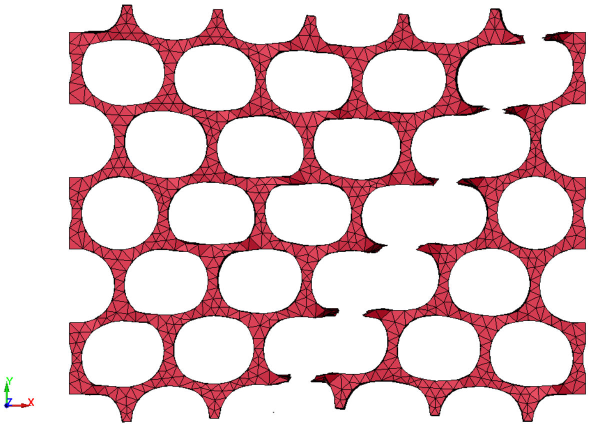

Figure 4.43: Fracture Mode of the Aluminium 6061-T6 Specimen under Horizontal Tension

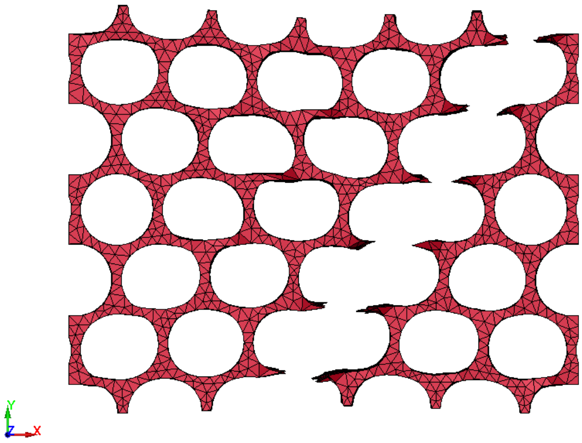

Figure 4.44: Fracture Mode of the ABS Specimen under Horizontal Tension

The uniaxial tension test conducted along the horizontal (X) axis quantifies the structural anisotropy under transverse tensile loading. As with compression, in this configuration, the load is applied perpendicular to the axis of the honeycomb tubes, resulting in deformation of the cell walls predominantly due to bending moments before tensile failure.

The structural orthotropy is confirmed by a drastic reduction in stiffness in all materials compared to the vertical loading direction. This is expected, as the flexural stiffness of the thin cell walls is significantly lower than their axial stiffness.

The qualitative behaviour of the horizontal tension curves mirrors the material identity observed in the vertical (Z) direction, but with drastically reduced initial slopes (and thus elastic stiffnesses), consistent with the findings from the compression test results.

A fundamental characteristic to note for this tension direction, unlike horizontal compression, is the stability of the post-yielding behaviour. As it is possible to notice, for all three materials, in tension, after reaching fracture, the measured stress follows a rapid drop, down to 0 MPa. The structure is no longer capable of sustaining any load and does not exhibit the unstable oscillations at higher stresses that occur in the compression case.

Titanium Ti6Al4V

The stress-strain curve for Titanium in horizontal tension shows an elastic phase with a substantially reduced slope ($K_X = 329,330$ N/mm) compared to the vertical tension test ($953,330$ N/mm), although, the value is higher than that of horizontal compression case value of approximately $224,666.7$ N/mm.
This asymmetry is likely a result of geometrical instability (buckling) under the condition of horizontal compression, resulting in premature, apparent softening of the structure and providing a lower measured value of stiffness than the tension test, which is structurally buckling-resistant.
Since tension does not induce the same early geometric instability, the measured stiffness

remains closer to the material's true structural elastic modulus, governed by the geometry of the cell walls, resulting in a higher $K_{X,\text{Tens}}$ value.

Regarding the maximum stress, the Titanium specimen reaches a value of 91.4 MPa with 3% strain. This is significantly lower than the 224.4 MPa reached in vertical tension, but similar to the horizontal compression case (which achieved a maximum strength value of 86 MPa at 3% strain). This similarity confirms that in the horizontal axis, the structural strength limit is dictated by the maximum flexural capacity of the cell walls even if it leads to different ultimate failure modes depending on the direction: buckling (compression) or tensile fracture (tension).
Failure is characterized by a sharp and rapid drop-off immediately after the peak, due to the semi-brittle nature of the LENS manufactured Ti6Al4V. Failure involves the brittle fracture of the cell walls due to the tensile stress induced by bending, without the progressive yielding seen in ductile materials.
In particular this can be seen in Figure 4.42, representing the resulting semi-brittle failure, visible as a fracture line that is mostly straight across the specimen. The cell walls at the rupture point appear sharp and minimally deformed, and in particular, the surrounding circular holes have retained their shape. This absence of profound plastic deformation confirm the quasi-brittle nature of the LENS-produced titanium alloy in this flexural-dominated failure mode.
Finally, the curve presents a stable post-peak behaviour, culminating in a stress that rapidly drops to 0 MPa. This stability is a key differentiator from horizontal compression, where cell wall buckling and self-contact generate substantial load oscillations and recoveries during specimen collapse. In tension, failure is a clean structural break, unable of sustaining further loads.

Aluminium 6061-T6

The Aluminium specimen demonstrates an equivalent stiffness of $K_X = 173,330$ N/mm. This value confirms the decrease in stiffness and the flexural-dominated deformation mechanism. It is less than the stiffness value obtained for the Aluminium specimen for the vertical tension test case ($502,000$ N/mm) and greater than the horizontal compression case at approximately $97,666.7$ N/mm. As with Titanium, the lower stiffness in compression in this direction is likely attributed to the premature structural softening caused by geometric instability (buckling). Although yielding occurs at a significantly lower stress level (about 29 MPa) compared to vertical loading, the material maintains its intrinsic ductile characteristics through plastic flow. The maximum stress is reached at 43.9 MPa with 10.5% strain. Again, this is lower than the peak stress for the vertical tension test (91.7 MPa at 5% strain), but similar to the horizontal compression case (peak stress at approximately 40 MPa at 10% strain). This confirms that strength in the horizontal (In-Plane) direction is controlled by bending capacity limit of the cell walls.
In this configuration, the geometric constraint imposed by the bending mechanism dominates the failure process for both tests (tension and compression), leading to comparable stress peaks.

The ultimate failure is the result of the catastrophic fracture of the cell walls under combined bending and tension, as it can be seen in Figure 4.43, followed by a rapid and stable drop-off to zero stress, mirroring the failure stability observed in Titanium under horizontal tension.

The path of the fracturing walls, as in the case of ABS follows a distinct diagonal line, differently from the straighter line observed in titanium. Moreover, the fracture occurs at a much larger strain than in titanium, and the surrounding holes are obviously more deformed and stretched out confirming the aluminium's more ductile behaviour.

ABS

The ABS polymer presents the lowest horizontal stiffness ($K_X = 5,279.3$ N/mm). The reduction ratio between vertical and horizontal tension stiffnesses ($K_X/K_Z \approx 48.6\%$) is marginally higher than for the metals, suggesting that the lower bulk modulus of the polymer makes the bending-induced stiffness reduction relatively more severe compared to the loss in axial capacity. This stiffness value is obviously lower than the vertical tension case ($10,851$ N/mm) and slightly higher than the respective horizontal compression test ($4,824$ N/mm). This trend (tension stiffer than compression) is consistent across all three materials in the horizontal direction. While polymers like ABS show intrinsic Tensile-Compressive Asymmetry (TCA) favouring compression in the vertical axis ($K_{Z,\text{Comp}}$ is 48.1% higher than $K_{Z,\text{Tens}}$), the horizontal axis is dominated by bending and instability. The geometric instability (buckling) induced by horizontal compression is the prevailing factor. This mechanism causes the structural softening observed in metals to also occur in the polymer, overriding the material's tendency to be stiffer in compression and resulting in $K_{X,\text{Tension}}$ being marginally higher than $K_{X,\text{Compression}}$.

The overall strength remains minimal (with a value of 4.3 MPa at 9% strain), and the rapid fracture behaviour confirms the structure's high sensitivity to tensile defects and low load-bearing capacity when subjected to transverse bending. Once again, the maximum stress is clearly lower than the vertical tension test (10.26 MPa at 4% strain) and is very similar to the maximum stress in horizontal compression (stress peak of 3.8 MPa at 0.105% strain). As established for the metallic specimens, this result confirms that in the horizontal axis, the failure load is primarily limited by the flexural capacity of the cellular struts, and is shown in Figure 4.44. The failure behavior of ABS is actually very similar to the behaviour of the aluminium, following a diagonal shear plane, though it occurs at a slightly higher strain (11%). The final image confirms the high deformation magnitude: the internal holes show extreme elongation and shape distortion before the walls finally break, demonstrating the polymer's intrinsic ability to handle large plastic strain even when the failure mode is dominated by bending.

Material	Maximum Stress [MPa]	Yield Stress [MPa]	Stiffness [N/mm]
Titanium Ti6Al4V	91.4	76.7	329,330
Aluminium 6061-T6	43.9	29	173,330
ABS	4.3	2.86	5,279.3

Table 4.11: Values of parameters obtained from Horizontal Uniaxial Tension

As previously done, to have a better understanding of the variation of the values of mechanical characteristics between the vertical and horizontal tension tests, the values obtained from the vertical tension test are here reported:

Material	Maximum Stress [MPa]	Yield Stress [MPa]	Stiffness [N/mm]
Titanium Ti6Al4V	224.4	159	953,330
Aluminium 6061-T6	91.7	83.7	502,000
ABS	10.26	10.12	10,851

Table 4.12: Values of parameters obtained from Vertical Uniaxial Tension

4.3.4 Second Family of Specimens - Isomass Specimens

As with the compression case, the analysis of the second family focuses on the specific structural efficiency under the constraint of constant mass (slightly less than 8 g). The Titanium and Aluminium specimens were proportionally scaled (sides of 18.2 mm and 21.5 mm respectively), while keeping the porosity ($\phi \approx 70\%$) and the dimensional ratios of the cell walls constant.
The ABS specimen served as the unscaled reference.

Vertical Tension

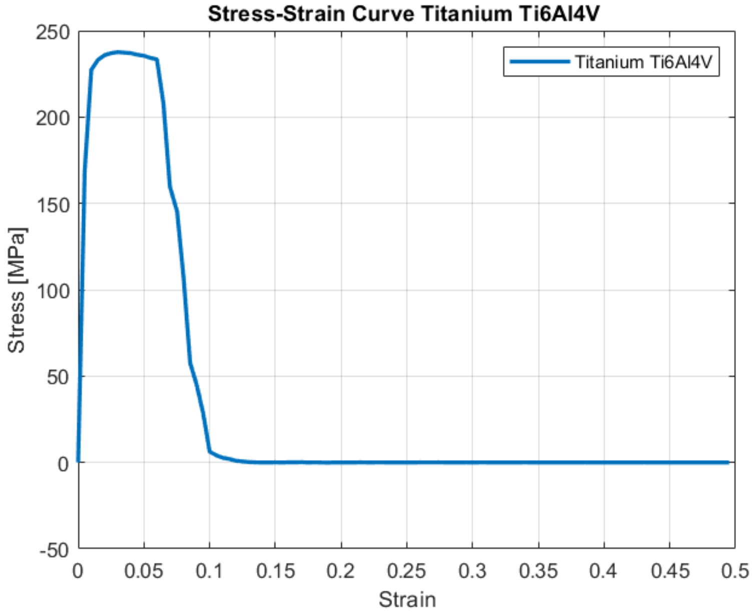

Figure 4.45: Stress-Strain Curve of the Specimen made with Titanium Ti6Al4V

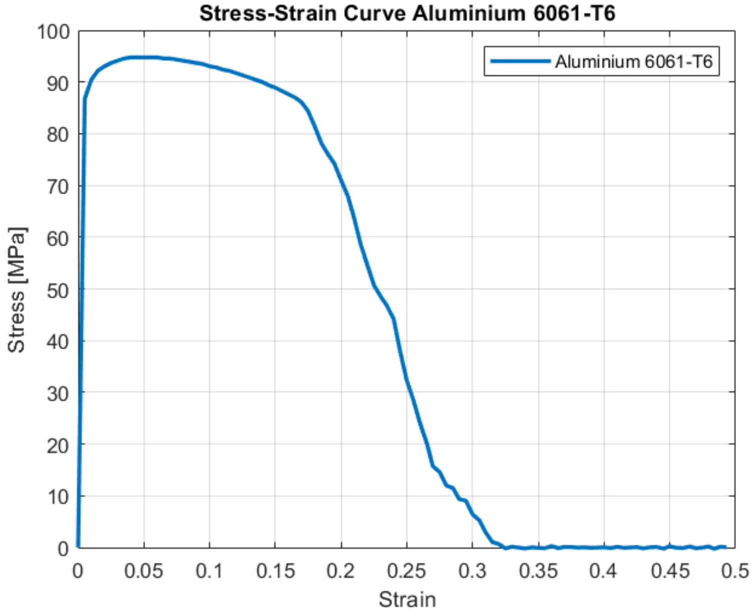

Figure 4.46: Stress-Strain Curve of the Specimen made with Aluminium 6061-T6

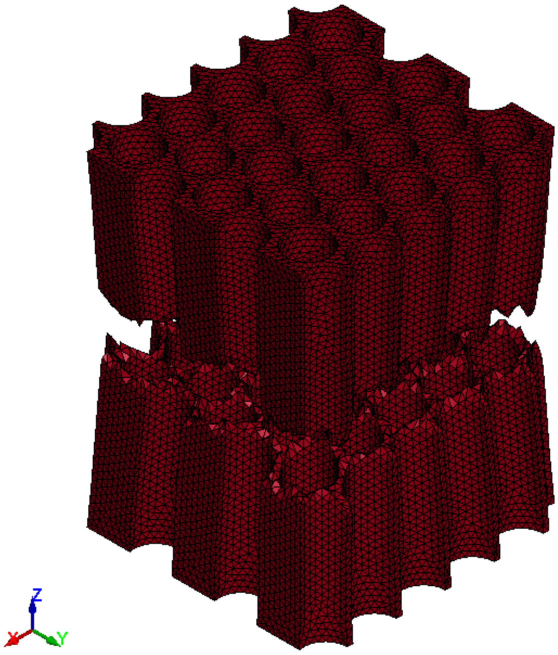

Figure 4.47: Fracture Mode of the Titanium Ti6Al4V Specimen under Vertical Tension

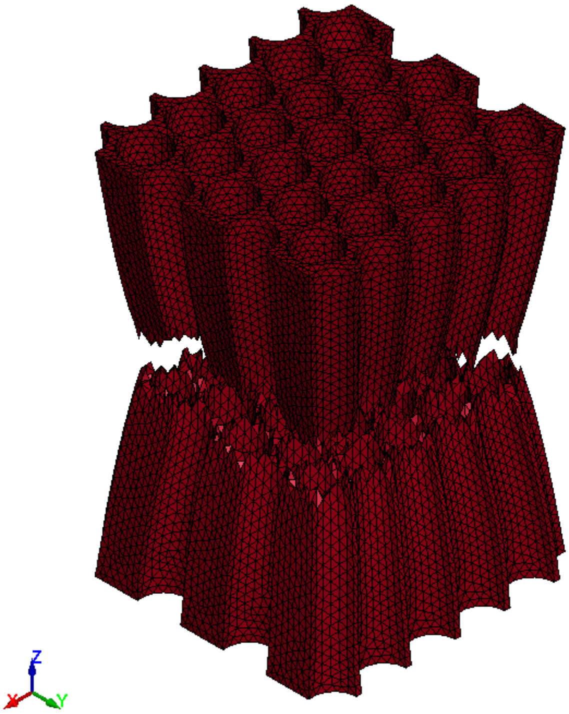

Figure 4.48: Fracture Mode of the Aluminium 6061-T6 Specimen under Vertical Tension

The proportional dimensional reduction required to achieve mass equivalence inevitably impacts the absolute structural stiffness. Since the structural stiffness (K) is proportional to the ratio between the nominal cross-sectional area (A_0) and the initial length (L_0), and both A_0 and L_0 are reduced in the scaled specimens, a consequential decrease in macroscopic stiffness is expected.

Titanium Ti6Al4V

Titanium which experienced the largest size decrease (from 30 mm to 18.2 mm), also experienced the most reduction in stiffness, by about 35.4% to $K_Z = 615,380$ N/mm. However, as it can be seen from Figure 4.45 the qualitative shape of the stress-strain curve was preserved, resulting in the same appearance with that of the vertical tension of the larger specimen from the first family. It is characterized by steep elasticity and rapid fracture at low strain, at about 6%, the same value as the previous vertical tension test on the larger specimen. Dimensional scaling did not alter the fundamental net-section failure mechanism determined by the material's semi-brittle nature,as it can be seen from Figure 4.47. The image shows the exact same failure mode as the larger specimen: a sharp, semi-brittle fracture with only a slight, localized necking (cross-section shrinkage), which is characteristic of the material's limited capacity for plastic work-hardening before rupture.

Despite the decrease in absolute stiffness, Titanium maintains the maximum specific strength, with a stress peak of approximately 237.6 MPa at 3% strain. As happened for the same comparison in the compressive case, this peak value is similar to, and even slightly higher than, the vertical case of the larger specimen (224 MPa). This phenomenon is characteristic of size effects and the greater intrinsic stability in scaled-down cellular structures. Specifically, in the tension case, failure is often initiated by microscopic defects or localized stress concentrations. By proportionally reducing the overall specimen size, the absolute size of the struts and nodes decreases, which can actually increase the structural efficiency and robustness against net-section failure. This leads to a marginally higher ultimate specific strength, reinforcing its superior performance for high-load, lightweight applications.

Comparing tension and compression, as expected, the maximum stress of this tension specimen (about 237.6 MPa at 3% strain) is also slightly lower than the maximum stress in vertical compression for this family of specimens (260 MPa at 6.6% strain), which also occurs at a greater strain.

Aluminium 6061-T6

The stiffness of Aluminium along the vertical direction decreased by 26.0% to $K_Z = 371,300$ N/mm compared to the previous family of specimens. This smaller reduction is consistent with the less severe dimensional scaling required for Aluminium compared to Titanium. The ductile yielding phases and subsequent work-hardening are once again

successfully maintained. More specifically, in this case, the yielding for the vertical tension occurs at 86.75 MPa at a strain of 0.5%, while the maximum stress is obtained at 94.75 MPa at a strain of 4%, similar to the previous family of tests where it was obtained a UTS of 91.7 MPa at a strain of 5%. This result confirms that the material's capacity for plastic energy absorption is preserved under mass optimization constraints, validating Aluminium as a suitable material for structural elements requiring specific ductility.
Moreover, the higher intrinsic ductility of the aluminium over titanium is also visibly confirmed in Figure 4.48, where, the proportional plastic deformation before rupture is significantly greater, resulting in a more pronounced necking compared to the titanium isomass specimen. This visible difference confirms that the material's capacity for plastic energy absorption is successfully preserved even under mass optimization constraints.

Horizontal Tension

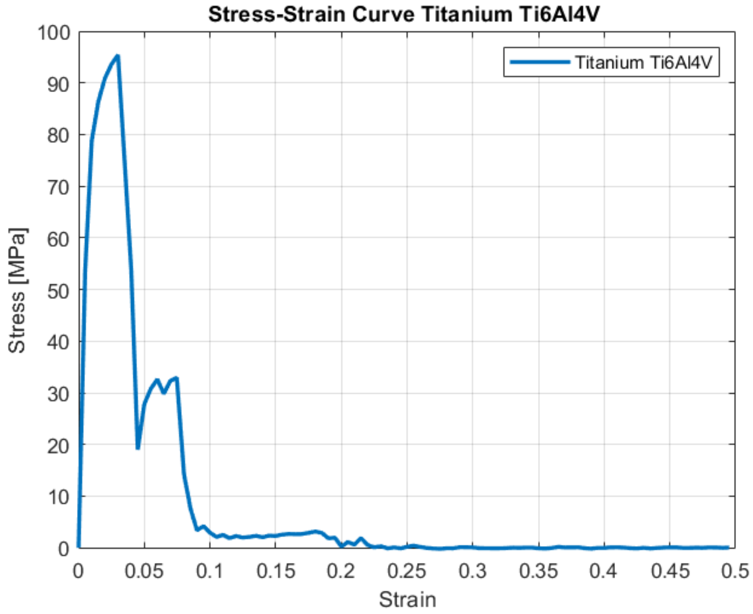

Figure 4.49: Stress-Strain Curve of the Specimen made with Titanium Ti6Al4V

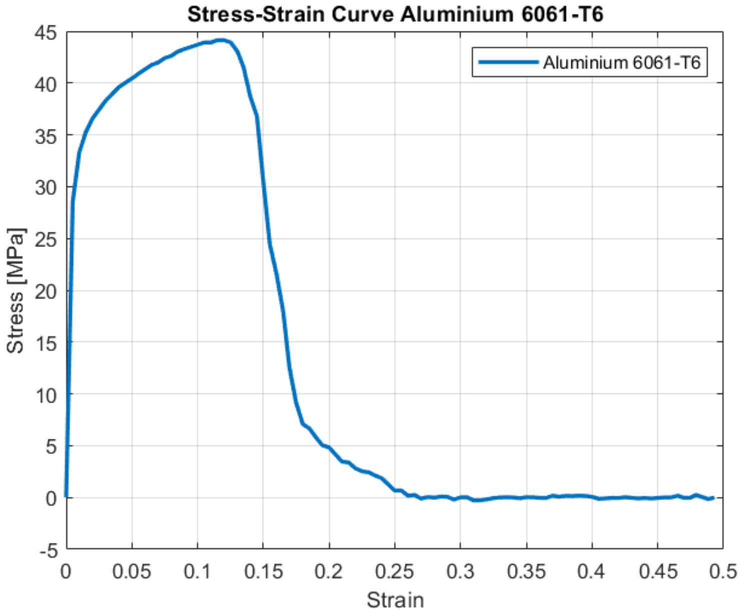

Figure 4.50: Stress-Strain Curve of the Specimen made with Aluminium 6061-T6

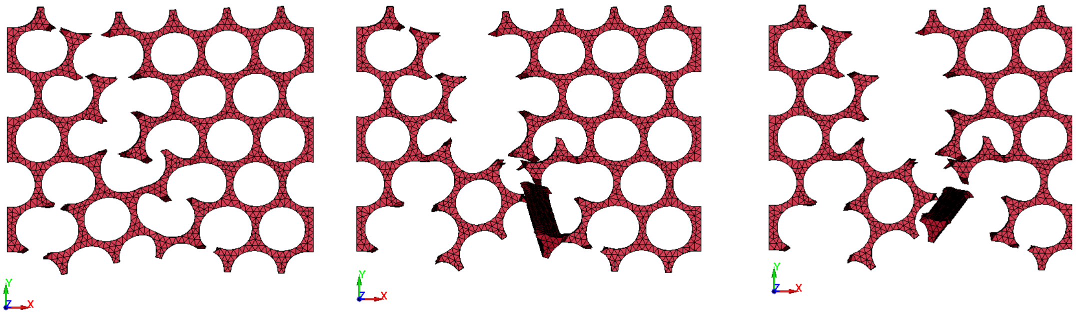

Figure 4.51: Fracture Mode of the Titanium Ti6Al4V Specimen under Horizontal Tension

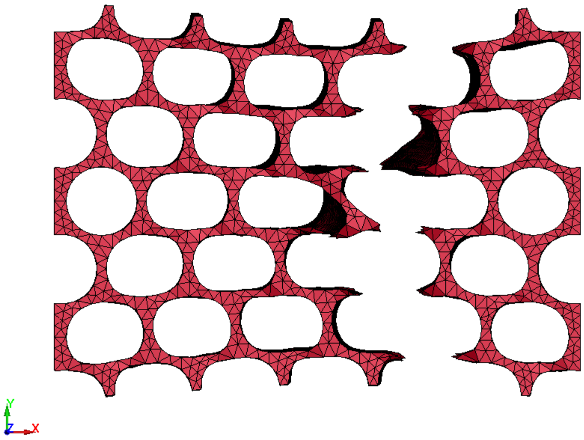

Figure 4.52: Fracture Mode of the Aluminium 6061-T6 Specimen under Horizontal Tension

Titanium Ti6Al4V

For horizontal tension, the scaled Titanium specimen presents a horizontal stiffness of $K_X = 195,600$ N/mm. The stiffness ratio $K_Z/K_X \approx 3.15$ confirms substantial orthotropy. This ratio is similar to the ratio found in the larger Family 1 specimen (2.89), demonstrating that the stiffness penalty associated with flexural-dominated transverse loading is an intrinsic geometric characteristic that survives dimensional scaling for mass optimization. It is, however, a lower ratio compared to the same ratios obtained for the compression test. Regarding yielding and maximum stress, they are 78.8 MPa and 95.4 MPa at 3% strain, respectively.

For this isomass specimen, the fracture process shows a more complex, multi-stage failure compared to the cleaner break of the previous family. After the initial cell wall rupture at approximately 3% strain, which causes the primary stress drop, few cell walls remain intact. These surviving walls momentarily carry some load, which explains that slight, temporary increase in stress (the second peak in the curve) until around 33 MPa and 7.5% of strain. Once these remaining walls fail, the specimen splits completely. This suggests a higher impact of local defects or load path on smaller specimens, leading to multi-stage failure progression.

Aluminium 6061-T6

For the horizontal direction, Aluminium shows $K_X = 122,220$ N/mm. The calculated anisotropy ratio $K_Z/K_X \approx 3.04$ is also largely preserved compared to the Family 1 ratio (2.90). These ratios for Aluminium are also lower than the compression case. The consistency of these ratios across different scales for both metals confirms that functional asymmetry is robust and governed by the conservation of relative cell wall relative dimensions and porosity. The failure mechanism remains the clean, rapid fracture of the cell

walls under bending-tension.
The fracture path in this isomass specimen, however, follows a line that is more linear rather than the diagonal path seen in the larger model. Once again, however, the aluminium's ductility is confirmed, as the circular holes adjacent to the final rupture line are extremely deformed and elongated, especially next to the rupture line. This extensive plastic deformation of the holes proves the material is still highly capable of absorbing plastic strain, even when the failure is dominated by flexure.
Finally, for this direction, the yielding stress is 28.6 MPa, while the maximum stress is 44.1 MPa, reached at 11.5% strain.

The ABS specimen maintains the properties of Family 1, serving as a constant mass and dimension reference. The transverse tension tests on the equivalent mass specimens confirm that geometric orthotropy is a scale-independent property of this cellular architecture, provided that relative dimensions are preserved through proportional scaling. Although the absolute stiffness decreases in both directions due to the overall reduction in specimen size, the anisotropic ratio remains highly consistent with the observations from the first family.

Finally, even for the tension test simulations, in terms of specific efficiency, the results suggest that Titanium, despite having undergone the largest dimensional variation, continues to guarantee the best performance, followed by Aluminium and finally ABS, confirming the behaviour observed in previous tests.

Material	Maximum Stress [MPa]	Yield Stress [MPa]	Stiffness [N/mm]
Titanium Ti6Al4V	237.6	227.3	615,380
Aluminium 6061-T6	94.75	86.75	371,300

Table 4.13: New values of parameters obtained from Vertical Uniaxial Tension

Material	Maximum Stress [MPa]	Yield Stress [MPa]	Stiffness [N/mm]
Titanium Ti6Al4V	95.4	78.8	195,600
Aluminium 6061-T6	44.1	28.6	122,220

Table 4.14: New values of parameters obtained from Horizontal Uniaxial Tension

4.3.5 Conclusions for the Simulations

The comprehensive analysis conducted on the compression and tension tests for the two families of specimens provides a definitive measure of the structural efficiency of the Fomes Fomentarius inspired architecture across different scales and material constraints.

The mechanical characterization of the bio-inspired honeycomb cellular structure under uniaxial tension and compression clearly establishes a complex interplay between bulk material properties, geometric orthotropy, and load direction-dependent failure mechanisms.

- **Titanium Ti6Al4V**: In both same-size (Family 1) and same-mass (Family 2) comparisons, Titanium consistently provided the maximum absolute stiffness and strength in all loading directions. Despite the dimensional scaling for the same-mass comparison reducing the absolute stiffness by over 35%, it still maintained the maximum specific performance. This validates the selection of high-strength, moderate-density alloys like Ti6Al4V for demanding structural or aerospace applications where maximizing performance under rigorous weight constraints is essential.
- **Aluminium 6061-T6**: It provided a strong balance between specific strength and ductility. Its near-perfect elastic stiffness symmetry in vertical loading confirms the theoretical model of an isotropic cellular solid. Furthermore, its capacity for significant plastic deformation in both compression and tension makes it highly effective for energy absorption applications, despite its lower absolute strength compared to Titanium.
- **ABS**: It confirmed its utility as an energy-absorbing material due to its large deformation in compression. However, its low elastic stiffness and sensitivity to FDM-induced defects under tensile load limit its applicability to non-primary load-bearing structures or systems designed exclusively for compressive impact mitigation.

The orthotropic behaviour, characterized by significantly higher stiffness and strength in the vertical (Out-of-Plane) direction compared to the horizontal (In-Plane) direction, was confirmed for all materials and both families. The conservation of the K_Z/K_X ratio under dimensional scaling (Family 1 vs. Family 2) confirms that this anisotropy is a robust and intrinsic property of the honeycomb geometry.

Vertical Direction (Out-of-Plane)

The most prominent feature is the Strength Asymmetry ($\sigma_{max,\text{Comp}} > \sigma_{max,\text{Tens}}$).

For the metallic specimens (Titanium and Aluminium) compression allows the structure to exploit geometric instability (phenomena of global buckling and barrelling), which sustains a higher ultimate load (246 MPa for Titanium) compared to the limit imposed by net-section fracture in tension (224.4 MPa for Titanium). For the ABS polymer, this asymmetry is extreme in terms of strain capacity ($\epsilon_{max,\text{Comp}} \approx 20\%$ vs. $\epsilon_{max,\text{Tens}} \approx 4\%$). Compression benefits from the closing of FDM-induced defects, while tension promotes crack propagation from the same defects.

The comparison of initial Elastic Stiffness in the vertical axis reveals that the metallic structures show near-perfect symmetry ($K_{Z,\text{Tens}} \approx K_{Z,\text{Comp}}$). This confirms that the initial elastic response is dictated purely by the geometry and the bulk material's modulus, irrespective of the load sign. In contrast, the ABS polymer shows a significant stiffness asymmetry ($K_{Z,\text{Comp}} > K_{Z,\text{Tens}}$) due to its intrinsic molecular and viscoelastic behaviour.

Horizontal Direction (In-Plane)

The structural behaviour is governed by the bending capacity of the thin cell walls.

- **Strength Symmetry**: The maximum structural stress values are remarkably similar across all materials ($\sigma_{max,\mathrm{Tens}} \approx \sigma_{max,\mathrm{Comp}}$). This structural convergence occurs because failure in this orientation is limited by the bending strength, irrespective of whether the final local mode is buckling (compression) or tensile fracture (tension).
- **Stiffness Asymmetry**: All materials show a slight structural softening under compression, resulting in $K_{X,\mathrm{Tens}} > K_{X,\mathrm{Comp}}$. This unexpected reversal of stiffness asymmetry is attributed to the early onset of geometric instability and structural softening induced by compression, which lowers the measured elastic modulus for both metals and polymers.

Finally, the analysis of anisotropy highlights that the anisotropy ratio (K_Z/K_X) is consistently higher in compression than in tension. This phenomenon confirms that the stiffness loss due to buckling in the horizontal compression direction causes an apparent increase of the structural orthotropy relative to the tensile case. This provides a critical insight for designing structures intended for compression-based energy absorption, where the stiffness in the bending plane is severely compromised.

5 Engineering Applications

This chapter presents a series of engineering applications which are related to the bioinspired microstructure studied throughout this work, derived from the internal organization of the fungus *Fomes Fomentarius*. The circular honeycomb structure, used as a reference in this research, provides a versatile and efficient model for developing lightweight, porous, and mechanically resistant systems.

Over the last decades, the design of porous materials has often taken inspiration from nature, where honeycomb and lattice structures are among the most widely used examples. Natural honeycombs, as found in beehives, consist of highly ordered arrays of hexagonal or nearly hexagonal cells. Their mechanical efficiency and low material usage have inspired generations of engineers to replicate their design principles for artificial applications.

Today, honeycomb structures can be produced in a wide variety of shapes and geometries, including triangular, square, and circular cells, as well as gradient configurations with varying wall thickness. The mechanical performance of these structures strongly depends on the geometric parameters of the cell, such as shape, size, and the thickness of the separating walls, which directly influence the overall stiffness, strength, and energy absorption capability of the system.

Naturally occurring honeycombs have fascinated scientists for centuries, and advances in fabrication technologies have enabled the reproduction of their architectures at different scales and with various materials. Engineered honeycomb systems are now used in multiple sectors, including aerospace, automotive, architecture, and packaging. These materials are appreciated for their ability to combine high strength-to-weight ratios with excellent impact absorption, insulation, and vibration damping properties.

Initially, the first man-made honeycomb cores were produced from paper, later replaced by metals, ceramics, and composites. The evolution of manufacturing techniques, from mechanical expansion and extrusion to modern additive manufacturing, has significantly improved the precision and versatility of honeycomb-based materials. Depending on the desired performance, honeycomb components can now be fabricated from aluminium, steel, titanium, polymers, or hybrid composites.

From a practical perspective, engineered honeycombs are typically developed to achieve three main objectives:

1. Lightweight design, where high stiffness and strength are achieved at minimal density, for example in aircraft, automobile, and architectural structures.
2. Energy absorption, in which the structure is optimized to dissipate impact energy, finding application in helmets, bumpers, and protective systems.
3. High shear and yield strength, often exploited in non-pneumatic tires, sandwich panels, and structural cores.

One of the earliest and most relevant applications is in honeycomb seals (5.1), widely employed in turbines and compressors to improve aerodynamic efficiency through leakage loss minimization in between rotating and fixed parts. Since the 1980s, they have replaced conventional labyrinth seals, to reduce wear to ensure a minimum gap loss, increased strength in turbomachinery and reduced rotor wear. Performance is relatively sensitive to design parameters such as sealing clearance and cell size, which are optimized to control leakage against structural stability.

Figure 5.1: Honeycomb Seal Segment[44]

Honeycomb cores have also been designed for electromagnetic and acoustic control, such as for sound absorption, vibration damping, or magnetic or radio frequency shielding. Corrosion-resistant coatings of aluminum honeycombs have been used to manage and directionalize airflow.

One of the most simple but useful features of cellular materials is that it is possible to tailor their mechanical properties in order to alter the mechanical properties, especially the effective stiffness of the structure. By functional grading in this way, designers can create components with high stiffness in certain areas and increased flexibility in others, a technique not dissimilar from the way most biological structures, like the Fomes fomentarius, allocate material on a needs basis for stresses.

This concept is particularly well-suited for the instance of additive manufacturing, as the capacity to define complex geometry enables local control of porosity and material location in precise detail. Functionally graded honeycomb structures have been employed, as examples, in lightweight brackets, automotive engine pistons, and turbine parts, demonstrating potential for high-performance and economically conscious engineering solutions resulting from nature-inspired mechanical optimization principles. In particular, reduction of the mass of any parts of vehicles directly influences their fuel consumption, which is increasingly in demand for higher fuel efficiency and lower carbon footprint.

5.1 Pillow Bracket

One interesting direction is the family of functionally graded lattice structures. These components are designed with gradual changes in density, allowing different stiffness values inside the same part. This design technique can be used for structural optimization, improving stiffness where needed while keeping the total mass very low. The same principle has already been applied to lightweight metal parts such as brackets or supports, where local changes in geometry make the structure stronger where the load is higher, and lighter where less material is needed.

A good example is the Ti6Al4V pillow bracket, whose geometry recalls the one of the circular honeycomb specimen studied here. Although the version found in literature is usually designed with squared or hexagonal holes, its logic is comparable. The shape of the hole is easily customizable, and cylindrical cavities like the one that simulated Fomes fomentarius can provide similar, or better, mechanical properties. The use of the alloy (Ti6Al4V) gives high specific stiffness, which can be utilized for both stiffness and light-weight application requirements.

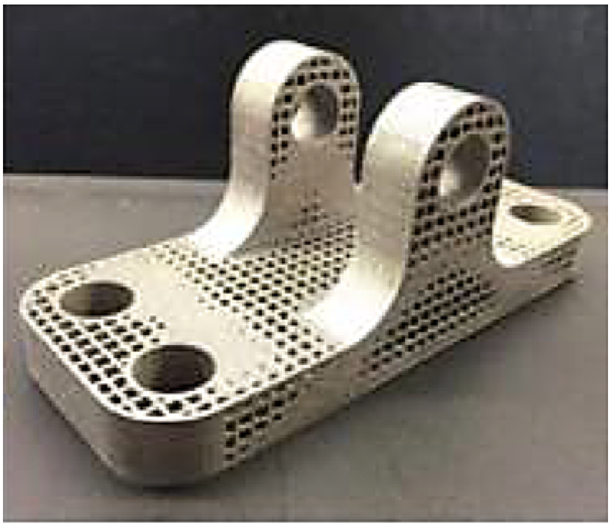

Figure 5.2: Ti6Al4V Pillow Bracket [10]

5.2 Gasoline Piston

Another sector where such a bioinspired structure can be applied is the automobile sector, where light weight is always an important factor. One prominent application is the use of a honeycomb lattice in the core of engine pistons. For instance, IAV Automotive Engineering, based in Berlin, has utilized metal 3D printing to develop a new type of piston for commercial vehicle engines featuring a strong internal honeycomb structure. This design addresses the industry trend towards achieving higher specific power output through increased pressure levels in the combustion chamber (up to 300 bar). The honeycomb lattice, which replaces the bulk solid material inside the piston, offers a dual benefit: it is both light in weight and exceptionally strong.

This innovative structure facilitates a mass reduction of approximately 25% compared to parts made via traditional casting methods. The reduced weight of the piston directly translates to lower loads applied to the bearings and less friction within the motor, subsequently influencing the counterweights on the crankshaft. Beyond weight savings, the structure, which incorporates through-holes whose dimensions change across the cross-section, is instrumental in optimizing the cooling of critical areas, further reducing friction and parasitic losses compared to conventional pistons. The designers have also integrated cooling channels within the piston head as an additional adjustment.

When manufactured using additive techniques, materials for this type of piston often include aluminum-silicon alloys. It should be noted that achieving the final geometry, especially concerning surface and clearance specifications, may necessitate hybrid fabrication techniques, combining AM with other conventional production processes.

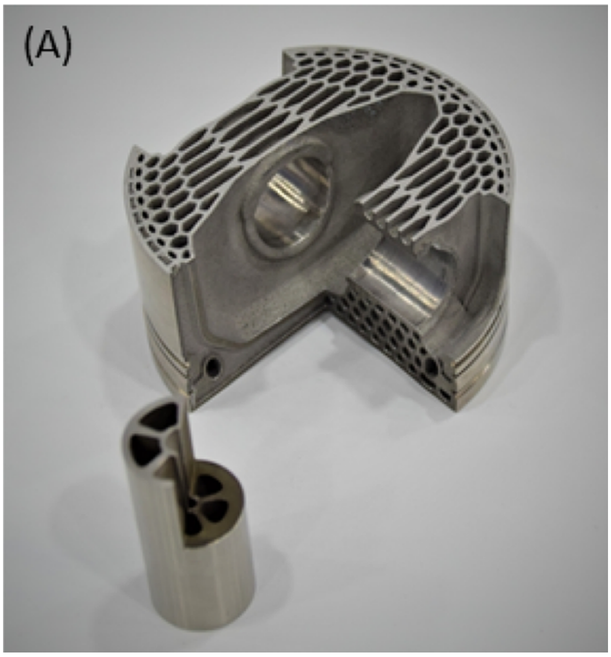

Figure 5.3: 3D Printed Gasoline Piston [10]

5.3 Rotor for Oil-Gas Separation

One further application focuses on a potentially major advancement for Additive Manufacturing in aerospace, investigated by a research team composed of members from the State Key Laboratory of Porous Metal Materials and the Shenyang Engine Design and Research Institute in China.
This area of study addresses oil–gas separation, a critical process of an aero-engine's lubrication system. Typically, the injection of lubricating oil to cool and lubricate the shaft bearings generates an oil–air mixture within the sealed bearing chambers, which must then be cleared and separated by a centrifugal separator.

The research reported by the paper of (Tang et al., 2016) [11], centred on designing a Ti6Al4V honeycomb structure featuring hexagonal cone-shaped pore channels. This novel component was manufactured using the AM technique of Selective Electron Beam Melting (SEBM). The results showed that the structure possessed high inherent strength, confirming that the pore shape and size within the SEBM-produced Ti6Al4V honeycomb are stable and well-suited for high-speed rotation in oil–gas separation.

To assess its effectiveness, the performance of the honeycomb structured Ti6Al4V rotor was directly compared to a conventional $Ni - Cr$ alloy sponge rotor. The separation efficiency of the Ti6Al4V rotor was impressive, reaching 99.8% and matching that of the $Ni - Cr$ sponge rotor at rotation speeds exceeding 4000 rpm, although its performance lagged slightly below this speed.

However, a distinct advantage was identified: the honeycomb-structured rotor exhibited significantly lower ventilation resistance, especially above 4000 rpm. Furthermore, the honeycomb rotor's ventilation resistance was observed to be much less affected by changes in rotation speed. Considering that the industry favours high rotation speeds, sometimes up to $18,000$ rpm, for rapid and effective separation, this characteristic gives the honeycomb rotor a clear functional superiority over the $Ni - Cr$ alloy sponge rotor.

Consequently, the authors concluded that, with continued design optimization guided by both modelling and experimentation, these new SEBM-manufactured Ti6Al4V separator rotors are strong candidates to become the next generation of oil–gas separation components in aero-engine lubrication systems.

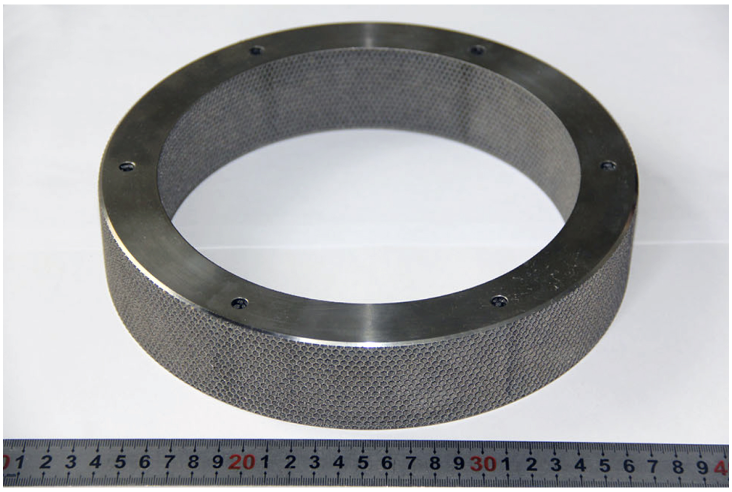

Figure 5.4: Ti-6Al-4V Honeycomb Rotor for Oil-Gas Separation [11]

5.4 Heat Exchangers

The field of heat exchangers provides another compelling application that aligns with the bio-inspired structure of this thesis. Modern metal Additive Manufacturing (AM) technologies are allowing engineers to produce heat exchangers with features, such as thickness, that are competitive with or equivalent to conventionally manufactured parts. The fundamental advantage of this approach is the ability to utilize the entire design volume to maximize the surface area of the heat exchanger. This capability results in highly efficient systems that are significantly lighter and provide superior thermal management, provided the correct geometric and material integrity is maintained.

Heat exchangers are traditionally made from materials like aluminum, titanium, steel, or cobalt chromium. However, the versatility of AM is expected to expand this material scope as more alloys are qualified for use in the process based on specific end-user demands.

For industries requiring performance levels beyond past capabilities, AM offers the potential to print heat exchangers with more complex shapes, higher levels of customizability, improved durability, better thermal management properties, lower weight. All of this can be achieved while simultaneously reducing the time and cost required to bring the product to market.

Multiple shapes and forms of heat exchangers can be used, depending on the application and final goal. AM has dramatically increased the freedom of design compared to traditional manufacturing, enabling complex internal geometries, as it is represented in the figure below. Among the various designs showed, one notable configuration features cylindrical holes arranged in a honeycomb pattern. This specific structure strongly resembles the morphology inspired by the fungus Fomes fomentarius and studied in the present thesis, representing a particularly relevant and further application for this bio-inspired cellular design.

Figure 5.5: Cross-section of Additive Manufactured Production Heat Exchanger [12]

Another application of heat exchangers through additive manufacturing is the following. As it was previously anticipated, Additive Manufacturing (AM) provides innovative methods for developing radiators and heat exchangers by unlocking the freedom to design complex structures. Unlike traditional methods that rely on welding, AM enables the successful fabrication of heat exchangers featuring micro-passage ways.
A prime illustration of this capability is the heat exchanger developed for the GE9X engine. Conventionally, this type of component was assembled from dozens of thin metal tubes. In order to enhance heat management performance, General Electric (GE) pioneered four entirely different AM-produced heat exchanger structures. trifurcating, tube-shell, plate-fin, and matrix, which are shown in the picture below.

The Matrix structure is particularly relevant to this thesis, as its arrangement directly mirrors the porous internal architecture of the Fomes fomentarius specimen that was previously simulated.

This component was manufactured using metal 3D printing. By adopting this novel structure, the heat exchanger achieved a notable 45% weight reduction and eliminated brazing joints entirely. The heat exchanger has also been certified and used in the Boeing 777X aircraft. Although the exact material is not specified, it is reasonable to believe that this component is made of a lightweight aluminum alloy, or Titanium Ti6Al4V.

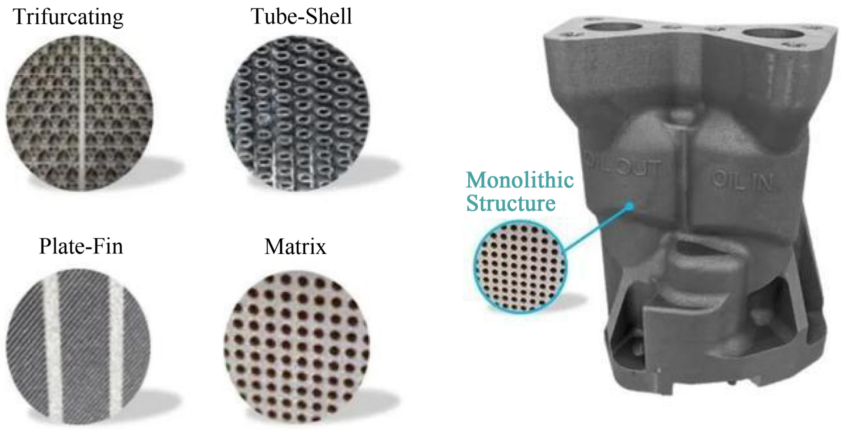

(a) Four different structures (b) Heat exchanger with matrix

Figure 5.6: Heat Exchanger in GE9X [13]

5.5 Energy Absorption Applications

Metal honeycombs are extensively employed as efficient energy absorbers in applications involving impact, primarily because of their exceptional capacity-to-weight ratio. Since many practical applications expose honeycomb materials to dynamic loading , understanding their energy-absorbing properties at relevant strain rates is crucial for accurate design and analysis. While in the past, experimental work focused on polymeric foams and plastic sheet honeycombs, the limited energy per unit volume they could absorb proved insufficient for certain high-demand applications. Consequently, the development of metal foams and honeycombs was necessary to substantially increase this capacity.

The high-density honeycombs examined in the study of Baker et al. (1998) [29] were specifically designed for a tunnel closure and sealing device. This device operates by rapidly sliding, in opposite direction, two heavy doors across a tunnel opening and subsequently needs to arrest their motion at a specific point. The study's specimens deviated from the typical hexagonal cell structure, instead featuring a greater sheet thickness, which conferred a higher density compared to materials in similar studies.

To accurately simulate these real-world conditions, particularly the high strain rates required, a specialized test method was developed to subject the honeycombs to impact conditions, achieving initial compressive strain rates up to approximately 2000/s. The aluminum honeycomb tested was constructed from 0.1905 mm thick sheets of 5052 aluminum. Its overall density was 881 kg/m^3, resulting in an effective density that was 32% of solid aluminum. This $\sim$ 32% solid density figure aligns closely with the $\sim$ 70% porosity established for the specimen studied in this thesis and inspired from the Fomes Fomentarius.

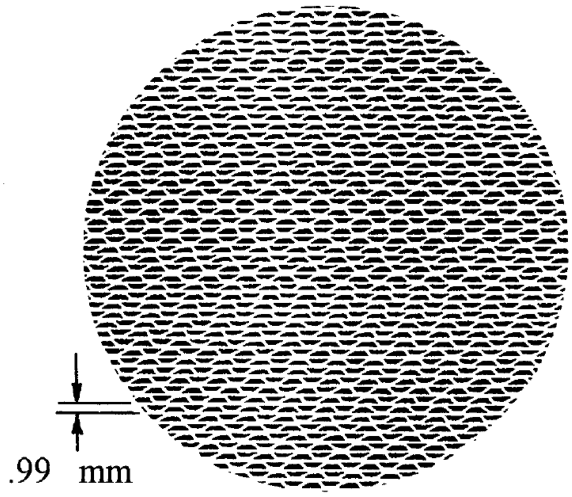

Figure 5.7: Honeycomb Cross-section [29]

The 5052 alloy is generally found to have a stress–strain curve that is almost rate-independent in the strain rate range attained in experiments. The aluminum honeycombs in the study consistently showed a strain-rate effect. For the aluminum honeycomb, this rate effect was observed despite the base 5052 material being largely rate-independent. Researchers attributed this to a change in the local collapse process between dynamic and quasi-static loading conditions.

A key conclusion of the work concerned the experimental method for compression testing: the technique of using external rings for constraint on the cylindrical aluminium specimens was highlighted. This technique is applicable to energy absorbers where it helps prevent global buckling and substantially reduces out-of-plane motion. By forcing the material to fail primarily through local cell-wall buckling, the overall absorbed energy is increased. The cross-section of the compressed aluminum honeycomb clearly shows the localized and corrugated deformation pattern induced during the test.

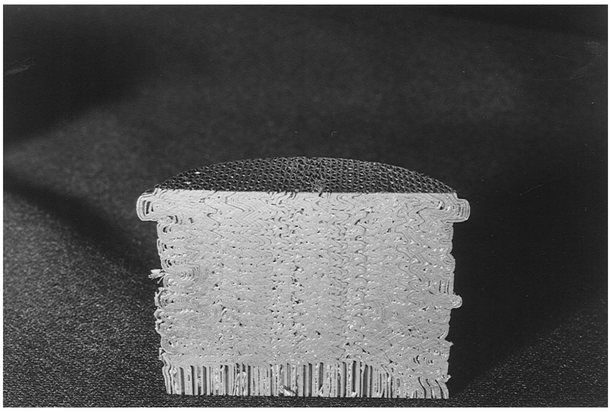

Figure 5.8: Cross sections of crushed specimens from quasi-static tests [29]

5.6 Polymeric Energy Absorber

A further application is here reported, representing an innovative method of constructing energy absorbers, with an innovative method designed to efficiently convert kinetic energy into strain energy during high-deformation events. The research proposes a practical application for hybrid energy absorbers aimed at improving vehicle safety.

The novel hybrid specimens consist of hollow, thin-walled metallic tubes filled with a polymeric honeycomb core. Specifically, the study employed square steel tubes that were modified with patterned windows on the wall, at half their height and filled with 3D-printed hexagonal honeycombs made from PET-G and ABS thermoplastics. The honeycomb cores were fabricated using the FDM technique.

The goal of the research was to determine the materials' energy absorption capacity and crashworthiness performance. This novel approach achieved several key goals, such as increasing energy absorption: the presence of the polymer core guaranteed an increase in energy absorption capacity compared to unfilled tubes. It also wanted to achieve controlled buckling: the strategically patterned windows were designed to change the buckling mode of the specimens and introduce an escape area, when dynamically loaded, leading to a reduction the magnitude of the peak force. This reduction is critical for vehicle safety, helping to lower the risk of neck and head injuries for occupants. Finally it also had the goal to improve space suitability, with the specimens' height made them suitable for insertion into small spaces, such as vehicle side doors, where they can replace traditional side protection bars.

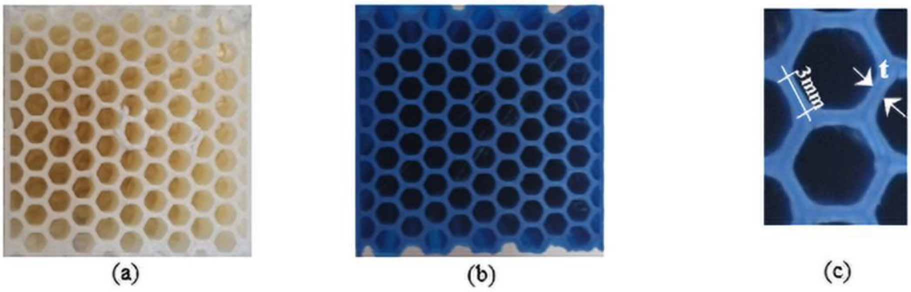

Figure 5.9: (a,b) Upper-view of the honeycomb core made of ABS and PET-G, respectively; (c) cell dimensions. [22]

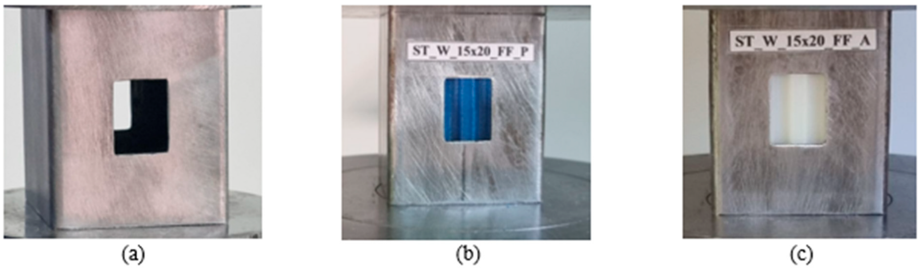

Figure 5.10: Design illustration of the thin-walled hybrid energy absorber with window (a) unfilled sample (b) filled sample with PET-G (c) filled sample with ABS [22]

The hybrid tubes were subjected to quasi-static axial compression. During testing, the patterned windows or the core material hindered the crush process. This resulted in the energy absorbers performing like a solid block, which ensured stable energy absorption. Overall, the composite steel/polymer combination undeniably withstood more loading than the metallic-only samples.
In the plastic phase, the core's contribution became more pronounced, with the ABS core leading to superior crashworthiness performance across key parameters, including Energy Absorption (E_a), Specific Energy Absorption (SEA), Peak Force (P_{peak}), Mean Force (P_m), Load Ratio (LR), and Structural Effectiveness (η).

The utilization of cellular structures as a core material for square steel thin-walled energy absorbers proved to be a successful strategy, significantly increasing energy absorption and enhancing structural effectiveness. Moreover, the augmentation of energy absorption for the baseline sample filled with ABS was about 23.2% greater than the sample filled with PET-G. Similar percentage augmentations were observed across various windowed samples.

An optimization study identified ABS as the optimal core material. This highlights that the novel hybrid energy absorber most effectively increased energy absorption specifically in the ABS samples.

5.7 3D Printed Gear and Sprocket Application

An especially compelling use case for cellular structures is demonstrated by an internal project at "Il Sentiero", where application engineers were tasked with significantly reducing the weight of standard components used in a test rig, and more specifically, the gears and sprockets.

The honeycomb structure proved to be the ideal choice, offering a perfect balance between substantial weight reduction, high structural stiffness (thanks to its wall thickness), and printability. The open design simplifies both the construction and modification processes within the software, a critical factor for rapid iteration. Crucially, the approach allowed the designer to leave the inner cavities of the honeycomb open without risking build failure, which was fundamental to achieving the desired weight savings.

For this application, the parts were produced using Metal 3D printing (metal powder bed fusion) with Stainless Steel (AISI 316L). This material choice reinforced the component's strength, making it suitable for the extreme environment in which the part will be used.

The redesign resulted in highly durable and significantly lighter components. In particular, the remodelled gear was 61% lighter than its traditional counterpart, and the sprocket was 53% lighter than the traditional model. When used on an entire shaft, the assembly was 46% lighter compared to the standard model, representing a major reduction in both weight and material consumption.

While this case utilized a standard hexagonal honeycomb morphology, one could conceptually achieve similar results by substituting the hexagonal holes with the circular-holed structure inspired by the Fomes fomentarius and investigated in this thesis. As with many engineering applications, the wall thickness of the cells remains a crucial variable, as it can be adjusted to arbitrarily tailor the component's final strength and weight characteristics. Furthermore, while stainless steel was here used, the choice of material is ultimately application-dependent. Materials like the Aluminium $6061-T6$ or Titanium Ti6Al4V previously analysed in this work could also be employed, based on the specific strength, stiffness, and environmental demands of the final component.

Figure 5.11: Honeycomb Structerd Gear [32]

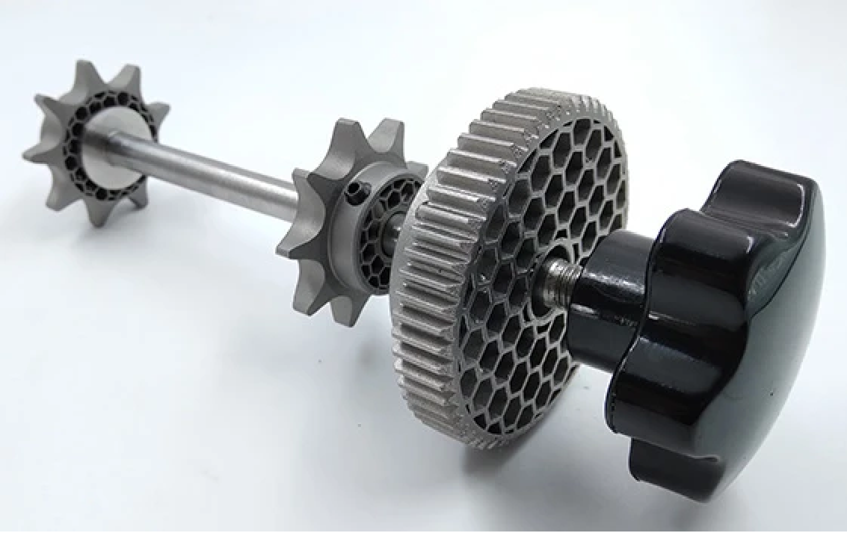

Figure 5.12: Final Assembly of Honeycomb Structured Gear and Sprocket [32]

5.8 Anticavitation Device

The phenomenon of cavitation, which consist in the formation and violent collapse of vapor bubbles resulting from sudden pressure drops in fluid systems, causes significant and costly damage, particularly within valves. Theoretically, preventing it is simple: keep the fluid velocity below the point where pressure falls below the vapor pressure. However, in practice, designing and manufacturing the necessary valve accessories has traditionally been complex, slow, and labor-intensive.Conventional solutions required assembling multiple components, such as plates or tubes, that were individually machined and often brazed together to create a tortuous path that breaks up the fluid stream to mitigate pressure drop and prevent cavitaion. This process demanded coordination with multiple suppliers and numerous manufacturing steps.

Additive Manufacturing (AM), particularly Laser Powder Bed Fusion (LPBF), has revolutionized the production of these anti-cavitation devices. This technology allows manufacturers to produce complex, optimized geometries as monolithic parts, replacing multi-component assemblies. By eliminating brazing and reducing manual labor, AM significantly cuts down on lead times (up to 70%) and lowers manufacturing costs, while simultaneously reducing potential points of failure.

Two leading industry examples demonstrate the shift to AM:

The first one is the Emerson's Fisher Cavitrol Hex Trim. Emerson discontinued its historical rotary valve trim, which was expensive and difficult to produce, requiring many brazed metal tubes, due to manufacturing complexity. Utilizing 3D printing, Emerson developed the new Fisher Cavitrol Hex Trim. This monolithic valve trim features a series of parallel hexagonal tubes that effectively slow the fluid by breaking it into multiple streams. The hexagonal geometry, which provides optimal strength and flow area, is only achievable through 3D printing and can be manufactured in a shape that perfectly contours the interior of the valve. Emerson now prints the trim in materials like stainless steel and cobalt chrome. Beyond preventing cavitation, this design also reduces noise and vibration and straightens the fluid flow.

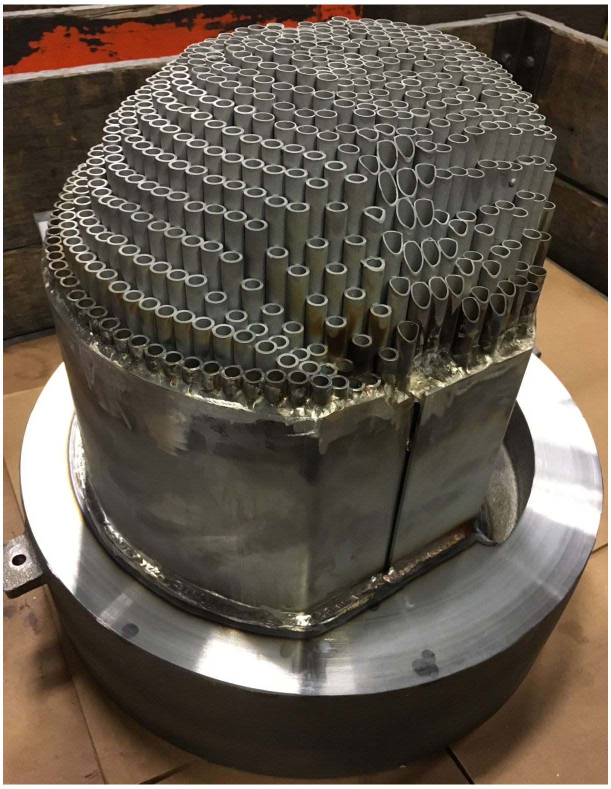

Figure 5.13: Emerson's conventionally produced anticavitation device involved many parts and skilled labor. Difficult and costly to produce [33]

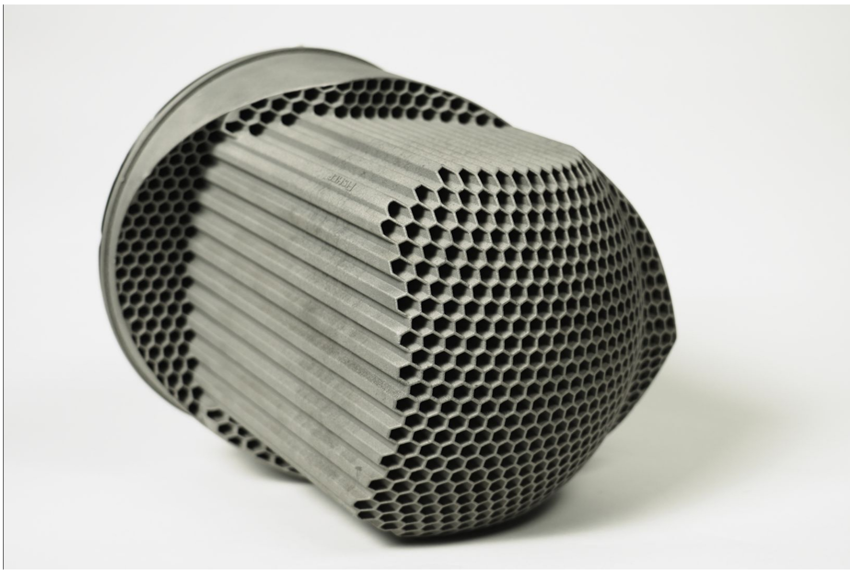

Figure 5.14: Emerson's 3D printed Cavitrol Hex trim incorporates hexagonal tubes and for most sizes can be manufactured all in one piece through laser powder bed fusion [33]

The second application is the Baker Hughes' Variable Resistance Trim Stack, showed in Figure 5.15 Baker Hughes conventionally produced its trim stacks by manually stacking and brazing individual machined metal sheets with strategically placed holes, a process that was time-consuming and challenging to manage across multiple vendors. Fluid is forced through a tortuous path inside the stack, again slowing its velocity and mitigating pressure drop that can otherwise lead to cavitation. By converting the design to AM, Baker Hughes now manufactures its variable resistance trim stacks internally using Inconel 718 on LPBF machines. The 3D printed devices are dimensionally similar to the conventional design but achieve an internal workflow that is faster, requires fewer steps, and reduces lead time by approximately 70%.

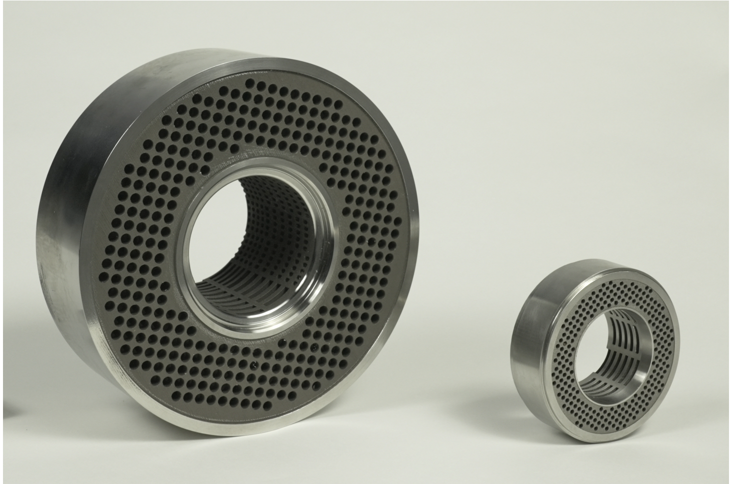

Figure 5.15: Baker Hughes now 3D prints variable resistance trim stacks all in one piece. The geometry has not changed much from the conventional stacks, but the manufacturing process has been dramatically simplified. [33]

One alternative conceptual design for these anti-cavitation components could be a solid cylindrical geometry perforated by a grid of circular holes. This highly porous structure strongly resembles the circular-holed honeycomb morphology inspired by the Fomes fomentarius and analyzed in this thesis, providing then a further possible application of the studied structure.

5.9 Thermoplastic Honeycomb Sandwich Panels for Mass Transit Vehicles

Cellular core sandwich structures are frequently adopted within the mass transit sector, a trend driven by their superior specific mechanical properties and substantial weight reduction benefits. These benefits directly translate into enhanced fuel efficiency and lower maintenance expenses.

A particularly relevant application is the use of a sandwich composite for a mass transit

bus side body panel, specifically targeting the pan-shaped section located below the passenger window. This area is structurally critical for maintaining integrity and ensuring crashworthiness.
The design uses a Polypropylene (PP) honeycomb core, which was selected for its, low density, high compressive strength, favorable energy absorption characteristics.

This core is integrated between face sheets made of E-glass fiber reinforced polypropylene (glass/PP) woven tape. Notably, this thermoplastic composite structure realized substantial weight savings of more than 55% over a conventional structure using aluminum skin and steel backup bars. This success demonstrates the effectiveness of honeycomb cores in structures where high stiffness and energy absorption must be realized at lightest possible weight.

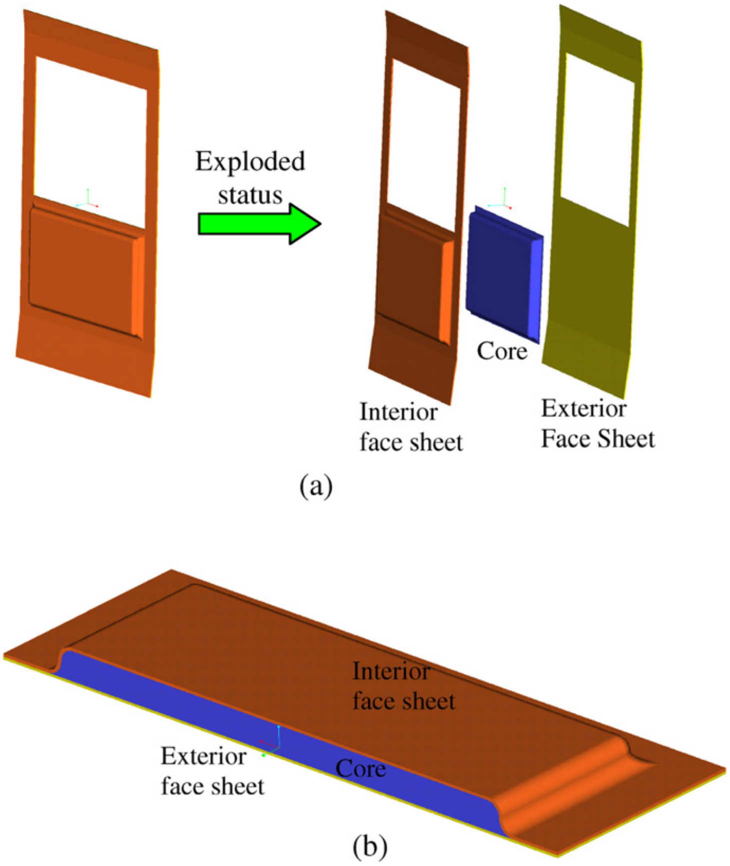

(a)

(b)

Figure 5.16: (a) Body panel and exploded view showing the three subcomponents, interior and exterior face sheet, core; (b) Cross-sectional view of the pan part of the body panel. [30]

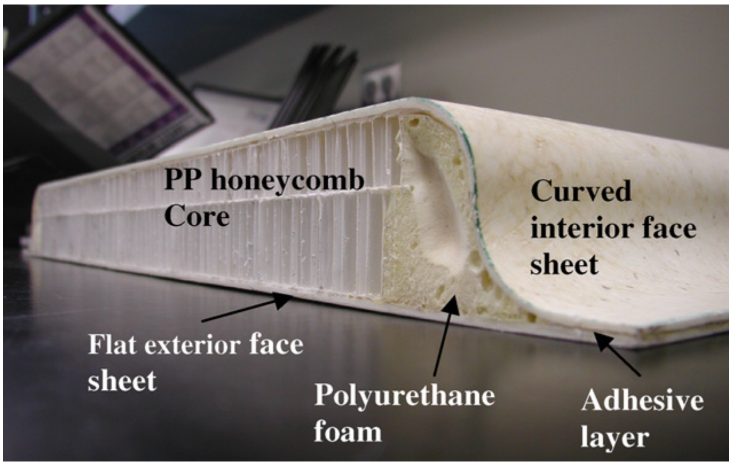

Figure 5.17: A cross-sectional view of the sandwich pan part. [30]

While this particular application uses a hexagonal PP core, the circular-holed honeycomb structure inspired by the Fomes fomentarius and studied in this thesis could potentially serve as an effective substitute, particularly given the strong energy absorption performance measured in the out-of-plane direction.
Moreover, the polymer Acrylonitrile Butadiene Styrene (ABS), which was analysed in the present work and is known for its excellent impact resistance, could also be considered a viable alternative material for the core in applications where structural damping and impact resistance are prioritized over maximizing lightweight performance.

5.10 Sandwich Panels

Sandwich panels are relatively common composite structural products and are employed in areas such as sports equipment, and in automotive and aeronautical applications. A typical sandwich panel is composed of three layers, in which two thin sheets (faces) of a stiff and strong material are separated by a thick core of low-density material. Sandwich structures have optimised specific flexural stiffness (flexural rigidity) because the separation of the two faces by a low density core increases the moment of inertia and hence contribute to the flexural stiffness of the panel, with only a small increase in panel mass. In addition to the high stiffness and low density of sandwich panels, an extra advantage of sandwich panels is that the designer can tailor the properties of the sandwich by adjusting the geometrical parameters of the panels (thickness of the core and the faces) independently of the material used.

A significant challenge in composite engineering is enhancing the recyclability of high-performance sandwich structures, which typically combine dissimilar materials (polymer faces with metal or wood cores). To address this, a viable application involves the development of all-polypropylene (all-PP) sandwich panels, where both the face sheets and the core are exclusively composed of PP-based materials. This mono-material design eliminates the costly and complicated material separation step at the product's end-of-life.

The faces are created from innovative high-modulus, highly oriented PP composite laminates (volume fraction $\sim 89\%$), while the core utilizes structural forms such as PP foam or PP tubular honeycomb. The PP honeycomb cores are fabricated from hexagonally packed, co-extruded tubes and offer superior out-of-plane shear properties (14 MPa for the 80 kg/m^3 density) compared to foam cores. Despite the lower intrinsic modulus of the all-PP faces compared to conventional glass-fiber reinforced PP (GFRPP), the resulting all-PP sandwich panels achieve similar specific flexural stiffness to GFRPP-faced counterparts due to the low density of the PP face material. This demonstrates a competitive performance-to-weight ratio.

Under four-point bending, all-PP panels exhibit a ductile failure mode characterized by the compressive yielding or buckling of the face sheet, in contrast to the brittle shear or adhesive failures common in GFRPP structures. While the low compressive strength of all-PP composites remains a limiting factor in flexure-critical designs, the ability to manufacture the face panels in incremental layers of thin plies provides designers with greater freedom to create optimized, low-weight structural solutions.

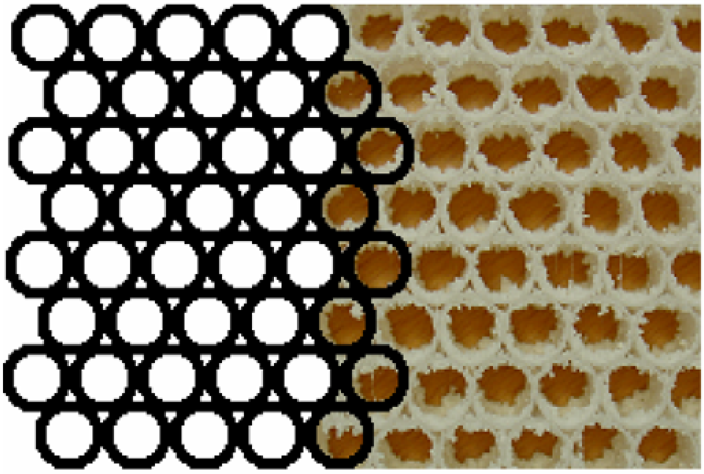

Figure 5.18: The structure of the tubular PP honeycomb core material used in the study. The right hand side shows a photograph of the cross-section of the honeycomb, while the left hand side shows a schematic of the tubular honeycomb at the same scale for clarity. [26]

]

Conclusions

The comprehensive simulation and analysis performed in the present work successfully achieved the objective of characterizing the mechanical response and inherent structural efficiency of the bio-inspired architecture, inspired by the fungus Fomes fomentarius, across both families of specimens analysed. It also succesfully quantified the performance trade-offs between the three chosen materials (Titanium Ti6Al4V, Aluminium 6061-T6, and ABS polymer) under various load and mass specifications.

The results strongly highlight the structure's geometric orthotropy, showing that applying load along the honeycomb axis (Out-of-Plane) delivers significantly higher stiffness and strength across all investigated materials, a characteristic entirely consistent with the cellular design. Furthermore, the results also revealed a Tensile-Compressive Asymmetry of the specimens and of the bio-inspired structure. In particular the metallic samples consistently withstanded notably greater maximum stresses in compression than in tension. This difference is not arbitrary, but it results from the structure effectively leveraging mechanisms like controlled buckling and folding to absorb energy during compressive loading, allowing it to reach an ultimate strength far beyond the limit imposed by tensile failure. This anisotropy proved to be a persistent property which occurred even in the dimensionally scaled (isomass) specimens, confirming that the directional variation in mechanical performance is maintained when relative geometric ratios are preserved.

In terms of material performance, instead, Titanium Ti6Al4V consistently outperformed the other tested materials for both specific stiffness and strength, validating its suitability for applications in industries like aerospace where weight restrictions are essential. Aluminium 6061-T6, achieved an excellent balance of ductility and strength, with its near-perfect elastic symmetry, which makes it an ideal choice for systems that require high plastic energy dissipation. Lastly, the ABS polymer, while showing high-capacity deformation, confirmed its most practical use in mitigating compressive impact, given its significantly lower absolute stiffness and high sensitivity to FDM-related defects when stressed in tension.

Many practical engineering applications relying on this or slightly modified bio-inspired structures were identified across various fields, including automotive, aerospace, transportation, heat exchanging, and energy absorption applications. This versatility is possible thanks to the possibility of producing this complex geometry through Additive Manufacturing (AM), which greatly increased precision allowing to widen the range of fields of applications. While recognizing the benefits of Additive Manufacturing, it is also important to consider the AM-induced defects (such as residual stress and surface imperfections) which can critically influence the performance. Therefore, the research of optimal post-treatment solutions (such as heat treatment) that can reduce or even eliminate some production defects is essential.

To build upon these findings, future research should focus on actually producing and testing the studied specimens under laboratory conditions. Moreover, with the advancement of AM, future studies could explore producing and studying the Fomes fomentarius honeycomb bio-inspired structure with new and different materials, expanding even more the range of its applications. Moreover, incorporating an explicit, localized model of AM-induced defects into the FEA models will be essential, particularly for materials like ABS, to narrow the gap between ideal simulations and the performance achieved by physically produced components.

Bibliography

[1] Wei J, Pan F, Ping H, Yang K, Wang Y, Wang Q, Fu Z. Bioinspired Additive Manufacturing of Hierarchical Materials: From Biostructures to Functions. Research 2023;6:Article 0164. https://doi.org/10.34133/research.0164

[2] Pleasant, D.; Gavin, C.; Redden, G.; Nagel, J.; Zhang, H. Bioinspired Design of Material Architecture for Additive Manufacturing. Machines 2023, 11, 1081. https://doi.org/10.3390/machines11121081

[3] Hoof fungus - Wild Food UK. (2024, November 7). Wild Food UK. `https://www.wildfooduk.com/mushroom-guide/hoof-fungus/`

[4] Amobonye, A., Lalung, J., Awasthi, M. K., & Pillai, S. (2023). Fungal mycelium as leather alternative: A sustainable biogenic material for the fashion industry. Sustainable Materials and Technologies, 38, e00724. `https://doi.org/10.1016/j.susmat.2023.e00724`

[5] Meyers, M. A., Chen, P.-Y., Lin, A. Y.-M., Seki, Y., & Materials Science and Engineering Program, Department of Mechanical and Aerospace Engineering, University of California, San Diego, La Jolla, CA 92093, United States. (2008). Biological materials: Structure and mechanical properties. In Progress in Materials Science (Vols. 53–53, pp. 1–206). https://doi.org/10.1016/j.pmatsci.2007.05.002

[6] Müller, C., Klemm, S., & Fleck, C. (2021). Bracket fungi, natural lightweight construction materials: hierarchical microstructure and compressive behavior of Fomes fomentarius fruit bodies. Applied Physics A, 127(3). https://doi.org/10.1007/s00339-020-04270-2

[7] Pylkkänen, R., Werner, D., Bishoyi, A., Weil, D., Scoppola, E., Wagermaier, W., Safeer, A., Bahri, S., Baldus, M., Paananen, A., Penttilä, M., Szilvay, G. R., & Mohammadi, P. (2023). The complex structure of Fomes fomentarius represents an architectural design for high-performance ultralightweight materials. Science Advances, 9(8). https://doi.org/10.1126/sciadv.ade5417

[8] Klemm, S., Freidank-Pohl, C., Bauer, L., Mantouvalou, I., Simon, U., & Fleck, C. (2024). Hierarchical structure and chemical composition of complementary segments of the fruiting bodies of Fomes fomentarius fungi fine-tune the compressive properties. PLoS ONE, 19(6), e0304614. https://doi.org/10.1371/journal.pone.0304614

[9] Yuan, L., Ding, S., & Wen, C. (2018). Additive manufacturing technology for porous

metal implant applications and triple minimal surface structures: A review. Bioactive Materials, 4, 56–70. https://doi.org/10.1016/j.bioactmat.2018.12.003

[10] Du Du Plessis, A., b, Razavi, N., Benedetti, M., Murchio, S., Leary, M., Watson, M., Bhate, D., Research Group 3DInnovation, Object Research Systems, Department of Mechanical and Industrial Engineering, Norwegian University of Science and Technology (NTNU), Department of Industrial Engineering, University of Trento, RMIT Centre for Additive Manufacturing, School of Engineering, RMIT University, 3DX Research Group, Arizona State University, & Berto, F., *. (2022). Properties and applications of additively manufactured metallic cellular materials: A review. In Progress in Materials Science (Vol. 125, p. 100918) [Journal-article]. https://doi.org/10.1016/j.pmatsci.2021.100918

[11] Tang, H. P., Wang, Q. B., Yang, G. Y., Gu, J., Liu, N., Jia, L., & Qian, M. (2016). A Honeycomb-Structured TI-6AL-4V Oil–Gas separation rotor additively manufactured by selective electron beam melting for aero-engine applications. JOM, 68(3), 799–805. https://doi.org/10.1007/s11837-015-1778-9

[12] KCI Media Group. (2023, October 18). AM in aerospace: The challenges and rewards of AM heat exchangers. Heat Exchanger World. https://heat-exchanger-world.com/am-in-aerospace-the-challenges-and-rewards-of-am-heat-exchangers/

[13] Sun, C., & Shang, G. (2022). Application of technology of additive manufacturing in radiators and heat exchangers. Journal of Power and Energy Engineering, 10(11), 35–44. https://doi.org/10.4236/jpee.2022.1011003

[14] Zhang, H., Nagel, J. K., Al-Qas, A., Gibbons, E., & Lee, J. J. (2018). Additive Manufacturing with Bioinspired Sustainable Product Design: A Conceptual Model. Procedia Manufacturing, 26, 880–891. https://doi.org/10.1016/j.promfg.2018.07.113

[15] Egan, P. F. (2023). Design for additive Manufacturing: recent innovations and future directions. Designs, 7(4), 83. https://doi.org/10.3390/designs7040083

[16] Yu, J., Li, J., & Hu, S. (2005). Strain-rate effect and micro-structural optimization of cellular metals. Mechanics of Materials, 38(1–2), 160–170. https://doi.org/10.1016/-j.mechmat.2005.05.018

[17] Hu, L., He, X., Wu, G., & Yu, T. (2014). Dynamic crushing of the circular-celled honeycombs under out-of-plane impact. International Journal of Impact Engineering, 75, 150–161. https://doi.org/10.1016/j.ijimpeng.2014.08.008

[18] Hu, L., Yu, T., Gao, Z.,& Huang, X. (2008). The inhomogeneous deformation of polycarbonate circular honeycombs under in-plane compression. International Journal of Mechanical Sciences, 50(7), 1224–1236. https://doi.org/10.1016/j.ijmecsci.2008.03.004

[19] Xu, M., a, Zhao, Z., a, Wang, P., a, Duan, S., a, Lei, H., a, Beijing Key Laboratory of Lightweight Multi-functional Composite Materials and Structures, Beijing Institute

of Technology, College of Engineering, & Peking University. (2022). Mechanical performance of bio-inspired hierarchical honeycomb metamaterials [Journal-article]. International Journal of Solids and Structures, 254–255, 111866. https://doi.org/10.1016/-\j.ijsolstr.2022.111866

[20] Wang, Z., Tian, H., Lu, Z., & Zhou, W. (2013). High-speed axial impact of aluminum honeycomb – Experiments and simulations. Composites Part B Engineering, 56, 1–8. https://doi.org/10.1016/j.compositesb.2013.07.013

[21] Ha, N. S., Pham, T. M., Tran, T. T., Hao, H., & Lu, G. (2022). Mechanical properties and energy absorption of bio-inspired hierarchical circular honeycomb. Composites Part B Engineering, 236, 109818. https://doi.org/10.1016/j.compositesb.2022.109818

[22] De Cássia Silva, R., De Castro, G. M., De Sousa Oliveira, A. B., & De Mendonça Brasil, A. C. (2024). Effect of 3D-Printed honeycomb core on compressive property of hybrid energy absorbers: experimental testing and optimization analysis. Materials, 17(2), 522. https://doi.org/10.3390/ma17020522

[23] Porter, Debora. FUNGAL STRUCTURES: THEIR MATERIAL PROPERTIES and APPLICATION to BIOINSPIRED DESIGN. May 2023.

[24] Analysis and development of additive manufactured novel Bio-inspired Lattice Structures. (2021).

[25] Kader, M. A., a, Hazell, P. J., Brown, A. D., Tahtali, M., Ahmed, S., Escobedo, J. P., Saadatfar, M., b, School of Engineering and Information Technology, The University of New South Wales, Canberra, ACT-2600, Australia, Department of Applied Mathematics, Research School of Physics, The Australian National University, Canberra, ACT-2601, Australia, & Weapons and Materials Research Directorate, CCDC Army Research Laboratory, Aberdeen Proving Ground, MD, 21005, USA. (2019). Novel design of closed-cell foam structures for property enhancement. In Additive Manufacturing [Journal-article]. https://doi.org/10.1016/j.addma.2019.100976

[26] Cabrera, N., Alcock, B., & Peijs, T. (2008b). Design and manufacture of all-PP sandwich panels based on co-extruded polypropylene tapes. Composites Part B Engineering, 39(7–8), 1183–1195. https://doi.org/10.1016/j.compositesb.2008.03.010

[27] Energy absorption characteristics of circular-celled honeycombs under in-plane quasi-static compressive loadings. (2021). In International Journal of Materials Research (Vol. 112, Issue 7, pp. 565–566).

[28] Liu, L., Li, L., Guo, C., Ge, Y., & Zhang, L. (2023). A study of the mechanical properties of Naturally-Inspired tubular Structures designed for lightweight applications. Applied Sciences, 13(11), 6519. https://doi.org/10.3390/app13116519

[29] BAKER, W. E., Jr., TOGAMI, T. C., WEYDERT, J. C., The University of New Mexico, & Sandia National Laboratories. (1998). STATIC AND DYNAMIC PROP-

ERTIES OF HIGH-DENSITY METAL HONEYCOMBS. In Int. J. Impact Engng (Vol. 21, Issue 3, p. 149—163). Elsevier Science Ltd.

[30] Ning, H., Janowski, G. M., Vaidya, U. K., & Husman, G. (2006). Thermoplastic sandwich structure design and manufacturing for the body panel of mass transit vehicle. Composite Structures, 80(1), 82–91. `https://doi.org/10.1016/j.compstruct.2006.04.090`

[31] Corex Honeycomb. (2025). Aluminium honeycomb for Automotive & Road Vehicles. In Corex Honeycomb. https://corex-honeycomb.com/applications/automotive-road-vehicles/

[32] Franchi, M. & Materialise. (2023). Sweet and simple: Magics' honeycomb structure keeps the gears ticking at the Il Sentiero campus [Case study]. `https://www.materialise.com/en/inspiration/cases/magics-honeycomb-structure-sentiero-campus`

[33] Hendrixson, S. (2024, May 21). Additive manufacturing versus cavitation. Gardner Business Media, Inc. https://www.valvemagazine.com/articles/additive-manufacturing-versus-cavitation-

[34] De Biasio, A., Ghasemnejad, H., Srimanosaowapak, S., & Watson, J. (2024). Development of multi aluminium foam-filled crash box systems to improve crashworthiness performance of road Service vehicle. European Journal of Mechanics - a/Solids, 109, 105433. https://doi.org/10.1016/j.euromechsol.2024.105433

[35] Ganilova, O. A., & Low, J. J. (2017). Application of smart honeycomb structures for automotive passive safety. Proceedings of the Institution of Mechanical Engineers Part D Journal of Automobile Engineering, 232(6), 797–811. `https://doi.org/10.1177/0954407017708916`

[36] Ngo, T. D., Kashani, A., Imbalzano, G., Nguyen, K. T. Q., David Hui, Department of Infrastructure Engineering, The University of Melbourne, Victoria 3010, Australia, & Composite Material Research Laboratory, Department of Mechanical Engineering, University of New Orleans, LA 70148, USA. (2018). Additive manufacturing (3D printing): A review of materials, methods, applications and challenges. Composites Part B, 172–196. https://doi.org/10.1016/j.compositesb.2018.02.012

[37] Wei, Y., Luo, X., Chu, X., Huang, G., & Li, C. (2020). Solid-state additive manufacturing high performance aluminum alloy 6061 enabled by an in-situ micro-forging assisted cold spray. Materials Science and Engineering A, 776, 139024. `https://doi.org/10.1016/j.msea.2020.139024`

[38] Habib, N., Vafadar, A., & Guzzomi, F. (2025). A comparative study of aluminium properties manufactured using additive friction stir deposition (AFSD) and wire arc additive manufacturing (WAAM). Progress in Additive Manufacturing, 10(11), 8963–8983. `https://doi.org/10.1007/s40964-025-01217-y`

[39] Beck, S., Rutherford, B., Avery, D., Phillips, B., Rao, H., Rekha, M., Brewer, L., Allison, P., & Jordon, J. (2021). The effect of solutionizing and artificial aging on the microstructure and mechanical properties in solid-state additive manufacturing of precipitation hardened Al–Mg–Si alloy. Materials Science and Engineering A, 819, 141351. https://doi.org/10.1016/j.msea.2021.141351

[40] LIVERMORE SOFTWARE TECHNOLOGY CORPORATION. (2013). LS-DYNA KEYWORD USER'S MANUAL VOLUME I.

[41] Baranowski, P., Małachowski, J., Płatek, P., & Szafrańska, A. (2019). LENS Ti-6Al-4V alloy material properties determination for LS-Dyna package. AIP Conference Proceedings. https://doi.org/10.1063/1.5092061

[42] Mehta, A., Zhou, L., Huynh, T., Park, S., Hyer, H., Song, S., Bai, Y., Imholte, D. D., Woolstenhulme, N. E., Wachs, D. M., & Sohn, Y. (2021b). Additive manufacturing and mechanical properties of the dense and crack free Zr-modified aluminum alloy 6061 fabricated by the laser-powder bed fusion. Additive Manufacturing, 41, 101966. https://doi.org/10.1016/j.addma.2021.101966

[43] Murray, C. M., Mao, M., Park, J., Howard, J., & Wereley, N. M. (2023). Visco-Elastic Honeycomb Structures with Increased Energy Absorption and Shape Recovery Performance Using Buckling Initiators. Polymers, 15(16), 3350. `https://doi.org/10.3390/polym15163350`

[44] Zhang, Q., Yang, X., Li, P., Huang, G., Feng, S., Shen, C., Han, B., Zhang, X., Jin, F., Xu, F., & Lu, T. J. (2015). Bioinspired engineering of honeycomb structure – Using nature to inspire human innovation. Progress in Materials Science, 74, 332–400. https://doi.org/10.1016/j.pmatsci.2015.05.001

[45] Du Plessis, A., a, Broeckhoven, C., Yadroitsava, I., Yadroitsev, I., Hands, C. H., Kunju, R., Bhate, D., Physics Department, Stellenbosch University, Stellenbosch 7602, South Africa, Laboratory of Functional Morphology, Department of Biology, Universiteitsplein 1, 2610 Wilrijk, Belgium, Department of Mechanical and Mechatronic Engineering, Central University of Technology, Bloemfontein 9300, South Africa, Department of Mechanical Engineering, Nelson Mandela University, Port Elizabeth 6031, South Africa, Altair Engineering Inc, 1820 Big Beaver Rd, Troy, MI 48083, USA, & The Polytechnic School, Arizona State University, 7001 E Williams Field Rd, Mesa, AZ 85212, USA. (2019). Beautiful and Functional: A review of biomimetic design in additive manufacturing. In Additive Manufacturing (pp. 408–427) [Journal-article]. https://doi.org/10.1016/j.addma.2019.03.033

[46] Ngo, T. D., Kashani, A., Imbalzano, G., Nguyen, K. T. Q., Department of Infrastructure Engineering, The University of Melbourne, & Composite Material Research Laboratory, Department of Mechanical Engineering, University of New Orleans. (2018). Additive manufacturing (3D printing): A review of materials, methods, applications and challenges. In Composites Part B (pp. 172–196). `https:`

//doi.org/10.1016/j.compositesb.2018.02.012

[47] Siddique, S. H., Hazell, P. J., Pereira, G. G., Wang, H., Escobedo, J. P., & Ameri, A. a. H. (2023b). On the Mechanical Behaviour of Biomimetic Cornstalk-Inspired Lightweight Structures. In Stuart Burgess (Ed.), Biomimetics (Vols. 8–8, pp. 92–92). https://doi.org/10.3390/biomimetics8010092

[48] Lobdell, M., Croop, B., Lobo, H., & DatapointLabs. (2015). Comparison of crash models for ductile plastics. In 10th European LS-DYNA Conference 2015. DYNAmore GmbH.

[49] Cho, Y., & Kim, T. (2016). Estimation of ultimate strength in single shear bolted connections with aluminum alloys (6061-T6). Thin-Walled Structures, 101, 43–57. https://doi.org/10.1016/j.tws.2015.11.017

[50] Mat, F., Ismail, K. A., Yaacob, S., & Ahmad, Z. (2014). Experimental and numerical analysis of Foam-Filled aluminum conical tubes subjected to oblique impact loading. Materials Testing, 56(11–12), 1001–1008. https://doi.org/10.3139/120.110663